

**PROBING HETEROGENEOUS DYNAMICS IN CONFINED
ENVIRONMENTS WITH SINGLE-PARTICLE TRACKING**

by

Yu Cai

B. Eng., Zhejiang University, 2014

A thesis submitted to the
Faculty of the Graduate School of the
University of Colorado in partial fulfillment
of the requirement for the degree of
Doctor of Philosophy
Department of Chemical and Biological Engineering
2018

This thesis entitled:

“Probing Heterogeneous Dynamics in Confined Environments with Single-Particle Tracking”

written by Yu Cai

has been approved for the Department of Chemical and Biological Engineering

Daniel K. Schwartz

Theodore W. Randolph

Date _____

The final copy of this thesis has been examined by the signatories, and we find that both the content and the form meet acceptable presentation standards of scholarly work in the above mentioned discipline.

Abstract

Cai, Yu (Ph.D., Department of Chemical and Biological Engineering)

Probing Heterogeneous Dynamics in Confined Environments with Single-Particle Tracking

Thesis directed by Professor Daniel K. Schwartz

The overall objective of the work was to develop and apply novel analytical techniques for the characterization of heterogeneous dynamics in confined environments. In this thesis, several different scenarios were explored involving heterogeneous dynamics of molecules or particles that are relevant to specific applications. In particular, total internal reflection fluorescence microscopy (TIRFM) was employed, enabling single-molecule imaging and tracking, to examine the adsorption and retention of protein molecules on a variety of model surfaces during site-blocking processes. By constructing super-resolution maps of the model surfaces, surface heterogeneity (induced by anomalous strong adsorption sites) was quantified as a function of protein surface coverage. Intermolecular Förster resonance energy transfer (FRET) was applied for the direct detection of potential protein-protein associations on the model surfaces. Again using TIRFM, the dynamics of cadherin ectodomains were investigated on supported lipid bilayers. Cadherins are a type of transmembrane proteins whose structures are highly determined by Ca^{2+} concentration. Single-molecule tracking technique allowed the observation of heterogeneous dynamics of individual cadherin ectodomains at different Ca^{2+} levels while they were associating with lipids. By performing careful statistical analyses on

cadherin diffusive behaviors, the presence of multiple modes was resolved within individual trajectories, providing detailed information about the interplay between the diffusion and conformation of cadherin at the molecular level. The other two projects described in this thesis provided insights into heterogeneous transport of nanoparticles in filtration processes. Specifically, an innovative nanoparticle tracking technique was developed, which enabled real-time imaging of nanoparticles while they were flowing through polymer filtration membranes and the characterization of membrane functional properties experienced by nanoparticles under different operating conditions. The functional tortuosity and particle retention in membrane, reflecting spatial heterogeneity and temporal heterogeneity in particle transport, were highly dependent on flow rate and tracer particle size and were correlated with each other. Additionally, systematic studies were performed to characterize membrane fouling mechanisms. Specifically, the evolution of effective flux, particle velocity and pathway tortuosity during fouling processes were measured in two different microfiltration membranes under “sticking” and “reduced-sticking” conditions, respectively. The single-particle tracking approach provided direct evidence for distinct fouling mechanisms, and the obtained comprehensive information can advance our understanding in complex mass transport and assist the design and optimization of separation processes.

Acknowledgements

My experience in graduate school has been incredibly enlightening and enjoyable. First and foremost, I would like to thank my thesis advisor, Daniel Schwartz, for always being extremely supportive since I joined the group in 2015. I have been deeply influenced by his powerful intellect and rational enthusiasm in science. His advising has been instrumental in inspiring critical thinking and problem solving, which ultimately helped me to evolve as an independent scientist. Dan, thank you for your time, energy and wisdom in advising over the past four years. It was one of the best decisions I have made to join the Schwartz research group.

I have had the opportunity to work or interact with many excellent scientists, engineers and staff in the Department of Chemical and Biological Engineering at the University of Colorado Boulder. In particular, I would like to acknowledge professors Theodore Randolph, Robert Davis, Andrew Goodwin, Joseph Falke and Yifu Ding for serving as my thesis committee members. Thank you all for selflessly giving your time and providing valuable guidance and insights to my thesis. I also want to thank Dominique de Vangel, who is the advisor of our graduate program, for his kind and prompt assistance throughout these years.

Next, I would like to thank all the talented researchers in the Schwartz lab, both past and present. Specifically, Mark Kastantin, Josh Mabry, Dapeng Wang, Kate Macri and Nathan Nelson all provided important technical assistance to me, such as tips and tricks for microscope and sophisticated algorithms for data analyses. I also enjoyed interacting with James Weltz,

Jeremiah Traeger, David Faulon, Becca Falatach, Andres Chaparro Sosa, Haichao Wu, Greg Morrin, Connor Thompson, Daniel Kienle and Raphael Sarfati. I gained knowledge, inspirations and tons of fun from many research-emphasizing or agreeably diverting office conversations with my groupmates. I want to thank all of them for making this collaborative and positive working environment. It was a true pleasure to work with all of them.

Importantly, I have been gratefully accompanied by many friends in Boulder throughout my studies in graduate school. Hao Wu, Della Shin, Nick Blum, Shiyi Wang and Sijia Huang have been close friends of mine for years. We have had countless fun gatherings that I will never forget about. I want to thank Hao, Shiyi and Sijia for their generous support in life and for carrying me through all the exciting outdoor activities. I like talking to Nick and appreciate his constant encouragement, which has been uplifting and refreshing. I am fortunate to have Della as my roommate, who is so compassionate and delightful. I enjoyed the exotic food (and alcohols) that she shared with me, as well as the time that we spent on random topics. Pengxiao Hao and Ke Ma have kindly provided lots of advice and encouragement, and I want to thank both of them for all the helpful hallway conversations (which usually went quite long). I would also like to thank Shengchang Tang for bearing my (occasional) complaints and motivating me in work and in life with his persistence and resilience.

Finally, I would like to express my deepest gratitude to my parents, who have been bringing me unconditional love and support for 26 years. They are the most open-minded and thoughtful parents as they always respect my opinions and decisions. Even though we did not spend much time together physically in the past few years, I know that the companionship of them is everlasting. Mom and dad, thank you.

Table of Contents

CHAPTER 1	INTRODUCTION	1
1.1	HETEROGENEOUS SCENARIOS	2
1.1.1	Heterogeneous Protein Adsorption and Site Blocking at Solid-Liquid Interfaces ...	2
1.1.1.1	<i>Surface properties affect protein adsorption</i>	2
1.1.1.2	<i>Site blocking on heterogeneous surfaces</i>	3
1.1.2	Heterogeneous Protein Dynamics on Supported Lipid Bilayers	4
1.1.2.1	<i>Cadherin conformations</i>	4
1.1.2.2	<i>Molecular diffusion associated with supported lipid bilayers</i>	6
1.1.3	Heterogeneous Particle Transport in Porous Media	7
1.1.3.1	<i>Membrane tortuosity and spatiotemporal heterogeneity</i>	7
1.1.3.2	<i>Membrane fouling</i>	8
1.2	CHALLENGES IN CHARACTERIZING HETEROGENEOUS DYNAMICS	9
1.3	TRACKING MOLECULES AND PARTICLES WITH FLUORESCENCE MICROSCOPY	11
1.3.1	Single Molecule Detection at Interfaces	11
1.3.2	Total Internal Reflection Fluorescence Microscopy (TIRFM).....	12
1.3.3	Förster Resonance Energy Transfer (FRET)	14
1.3.4	Tracking Nanoparticles in Porous Media	16
1.4	GOALS AND OBJECTIVES	18
1.4.1	Surface Heterogeneity.....	18
1.4.2	Molecular Dynamic Heterogeneity.....	18
1.4.3	Transport Heterogeneity	18
1.5	REFERENCES	19

CHAPTER 2	INFLUENCE OF PROTEIN SURFACE COVERAGE ON ANOMALOUSLY STRONG ADSORPTION SITES.....	28
2.1	ABSTRACT	28
2.2	INTRODUCTION	29
2.3	EXPERIMENTAL METHODOLOGY	32
2.3.1	Surface Preparation and Characterization	32
2.3.2	Protein Solutions.....	32
2.3.3	Single-Molecule Tracking	33
2.3.3.1	<i>Single-color concentration-dependent experiments</i>	33
2.3.3.2	<i>Förster resonance energy transfer</i>	34
2.3.4	HSA Surface Area Fraction	35
2.3.5	Data Analysis.....	36
2.3.5.3	<i>Surface heterogeneity</i>	37
2.3.5.4	<i>Cumulative residence time distributions (CRTD)</i>	37
2.4	RESULTS AND DISCUSSION	38
2.4.1	Surface Area Fraction	38
2.4.2	Site Blocking on TMS, FS and OEG Surfaces	40
2.4.3	Anomalous Site Blocking on NH ₂ Surfaces	47
2.5	CONCLUSIONS	53
2.6	REFERENCES.....	54
CHAPTER 3	CADHERIN DIFFUSION IN SUPPORTED LIPID BILAYERS EXHIBITS CALCIUM-DEPENDENT DYNAMIC HETEROGENEITY	62
3.1	ABSTRACT	62
3.2	INTRODUCTION	63
3.3	EXPERIMENTAL METHODOLOGY	65
3.3.1	Materials	65
3.3.2	Sample Preparation.....	65

3.3.3	Single-Molecule Tracking	66
3.3.4	Data Analysis.....	67
3.3.4.1	<i>Mean Squared Displacement and Mean Diffusion Coefficient</i>	67
3.3.4.2	<i>Diffusion Coefficient Distributions</i>	68
3.3.4.3	<i>Step Size Distributions</i>	68
3.4	RESULTS AND DISCUSSION	69
3.4.1	Calcium-Dependent Ensemble Average Diffusion	69
3.4.2	Step Size Distributions and Diffusive Heterogeneity.....	72
3.4.3	Support for a Single Diffusive Population	75
3.4.4	Interpretation of the Observed Dynamic Heterogeneity.....	79
3.5	CONCLUSIONS	80
3.6	REFERENCES.....	80
CHAPTER 4 MAPPING THE FUNCTIONAL TORTUOSITY AND SPATIO-TEMPORAL HETEROGENEITY OF POROUS POLYMER MEMBRANES WITH SUPER-RESOLUTION NANOPARTICLE TRACKING		86
4.1	ABSTRACT	86
4.2	INTRODUCTION	87
4.3	EXPERIMENTAL METHODOLOGY	89
4.3.1	Materials and Sample Preparation.....	89
4.3.2	Single-Particle Tracking.....	92
4.3.3	Data Analysis.....	93
4.3.3.1	<i>Mean squared displacements</i>	93
4.3.3.2	<i>Péclet number</i>	93
4.3.3.3	<i>Tortuosity</i>	94
4.3.3.4	<i>Normalized residence time distributions</i>	95
4.4	RESULTS AND DISCUSSION	96
4.4.1	Conventional Measurements of Apparent Tortuosity under Stagnant Conditions..	96

4.4.2	Tortuosity of Nanoparticle Trajectories Depends on Pe and Tracer Particle Size..	98
4.4.3	Spatial Heterogeneity	101
4.4.4	Temporal Heterogeneity	103
4.4.5	Correlation between Tortuosity and Retention.....	106
4.5	CONCLUSIONS	111
4.6	REFERENCES.....	112
CHAPTER 5 SINGLE-NANOPARTICLE TRACKING REVEALS MECHANISMS OF MEMBRANE FOULING.....		118
5.1	ABSTRACT	118
5.2	INTRODUCTION.....	119
5.3	EXPERIMENTAL METHODOLOGY	120
5.3.1	Materials and Sample Preparation.....	120
5.3.2	Fluorescence Microscopy and Single-Particle Tracking	123
5.3.3	Normalized Flux and Normalized Mean Particle Velocity	124
5.3.4	Tortuosity Distributions.....	125
5.4	RESULTS AND DISCUSSIONS	125
5.4.1	Controlling the “Stickiness” of Tracer Particles in Membrane	125
5.4.2	Visualizing Particle Trajectories in Fouling Processes	128
5.4.3	Evolution of Effective Flux and Particle Velocity	130
5.4.4	Progression of Membrane Functional Tortuosity	134
5.4.5	Hypothetical Fouling Mechanisms.....	137
5.5	CONCLUSIONS	138
5.6	REFERENCES.....	139
BIBLIOGRAPHY.....		143
APPENDIX A: SUPPORTING INFORMATION FOR CHAPTER 2		164
A.1	SUPPLEMENTARY TABLE	164

A.2	SUPPLEMENTARY FIGURES	165
APPENDIX B: SUPPORTING INFORMATION FOR CHAPTER 3		168
B.1	SUPPLEMENTARY TABLES.....	168
B.2	SUPPLEMENTARY FIGURES	171
APPENDIX C: SUPPORTING INFORMATION FOR CHAPTER 4		173
C.1	SUPPLEMENTARY TABLES.....	173
C.2	SUPPLEMENTARY FIGURES	175
APPENDIX D: SUPPORTING INFORMATION FOR CHAPTER 5		180
D.1	SUPPLEMENTARY FIGURES	180

List of Tables

Table 5-1. Compositions of index-matching liquids and tracer particles used to formulate “reduced-sticking” and “sticking” conditions in PVDF and PTFE membranes.....	123
Table A-1. The fitting parameters of f (site fractions) and λ (characteristic number of adsorption events) from a Poisson mixture model of HSA adsorption	164
Table B-1. The best-fit parameters of f_i and λ_i from a Rayleigh mixture model for the histograms of step sizes	168
Table B-2. The ensemble diffusion coefficients calculated by fitting the MSD vs lag time plots for the diffusion of cadherin and fluorescently labeled lipids	169
Table B-3. The best-fit parameters of μ and σ associated with fits of the histograms of individual trajectory diffusion coefficients to a reciprocal normal distribution	170
Table C-1. Fitting parameters and calculated diffusion coefficients for mean squared displacement versus time plots	173
Table C-2. Calculated standard deviation values for histograms of normalized residence time distributions for three replicate experiments.....	173
Table C-3. Ratios of mean residence times for more tortuous trajectories and less tortuous trajectories for different experimental conditions.....	174

List of Figures

Figure 1-1. Represented schematic diagram showing silanization mechanism on a silica substrate	2
Figure 1-2. Diagram of general cadherin structure	5
Figure 1-3. Diagram showing the contour length of a pathway and the end-to-end distance of the corresponding pathway in a porous media.....	7
Figure 1-4. Schematic diagram of a prism-based total internal reflection fluorescence (TIRF) microscope.	13
Figure 1-5. Spectra of FRET pair Alexa Fluor 532 and Alexa Fluor 647 fluorophores	15
Figure 1-6. Schematic diagrams of intermolecular FRET events on surface at different surface coverages.....	16
Figure 1-7. Schematic diagram of an epifluorescence microscope used to image nanoparticle transport in a flow cell	17
Figure 2-1. Adsorption isotherms vs. concentration of HSA on TMS, NH ₂ , FS and OEG surfaces	39
Figure 2-2. Representative super-resolution adsorption maps of HSA on TMS, FS and OEG surfaces at different HSA area fractions	41
Figure 2-3. The probability distributions of HSA site adsorption events on TMS, FS and OEG surfaces at different area fractions	43
Figure 2-4. The relative surface heterogeneity parameter versus HSA concentration and HSA area fraction on TMS, FS and OEG surfaces.....	44
Figure 2-5. Representative cumulative residence time distributions and mean residence times of HSA on strong sites and weak sites on TMS, FS and OEG surfaces	46
Figure 2-6. Representative super-resolution maps, probability distributions of site adsorption events and relative surface heterogeneity parameters of HSA on NH ₂ surface at different surface area fractions	48

Figure 2-7. Super-resolution FRET maps of donor and acceptor channels on NH ₂ surfaces at different HSA area fractions	49
Figure 2-8. Representative cumulative residence time distributions and corresponding mean residence times of HSA on strong sites and weak sites at low and high HSA area fractions.....	52
Figure 3-1. Ensemble mean squared displacements vs lag time plots for the diffusion of cadherin at different Ca ²⁺ concentrations and the diffusion of fluorescently labeled lipids	70
Figure 3-2. Histograms of step sizes for cadherin diffusion at different Ca ²⁺ concentrations.....	73
Figure 3-3. Ensemble diffusion coefficients and average diffusion coefficients of cadherin on supported lipid bilayers as a function of Ca ²⁺ concentrations.	74
Figure 3-4. Histograms of cadherin diffusion coefficients at different Ca ²⁺ concentrations	76
Figure 3-5. Representative trajectories of cadherin diffusion on lipid bilayers at different Ca ²⁺ concentrations	78
Figure 4-1. Scanning electron microscope images of Durapore filtration membrane and schematic diagram showing the flow cell construction and the imaging system	91
Figure 4-2. Mean squared displacements vs. time plots for 40 nm and 200 nm nanoparticles diffusing in un-confined bulk solvent and in PVDF membranes	97
Figure 4-3. Trajectory maps in membrane obtained with 40 nm tracer particles and 200 nm tracer particles at varying <i>Pe</i>	98
Figure 4-4. Apparent mean local tortuosity and global tortuosity for 40 nm and 200 nm tracer particles at increasing <i>Pe</i>	100
Figure 4-5. Probability distributions of local tortuosity for 40 nm particle trajectories and 200 nm particle trajectories at various <i>Pe</i>	102
Figure 4-6. Representative heat map of normalized residence times	104
Figure 4-7. Histograms of normalized residence times per bin	105
Figure 4-8. Local tortuosity for trajectories that passed through short-retaining and long-retaining regions at increasing <i>Pe</i>	107
Figure 4-9. Heat maps showing correlations of normalized mean residence time per length vs the logarithm of tortuosity for each trajectory	109
Figure 5-1. Scanning electron microscope images of membranes.....	121

Figure 5-2. Schematic diagram showing the experimental set-up	122
Figure 5-3. Snapshots of tracer particles retained in the field of view under “reduced-sticking” and “sticking” conditions and corresponding normalized total fluorescence intensity	126
Figure 5-4. Representative trajectory maps during fouling processes under “reduced-sticking” and “sticking” conditions	129
Figure 5-5. Normalized effective flux vs time plots for PVDF and PTFE membranes under various experimental conditions.	131
Figure 5-6. Normalized mean particle velocity vs normalized flux reduction plots for PVDF and PTFE membranes	133
Figure 5-7. Probability distributions of local tortuosity in PVDF and PTFE membranes under “reduced-sticking” and “sticking” conditions at different stages of fouling	136
Figure 5-8. Schematic diagrams of different fouling mechanisms in membrane constrictions under “reduced-sticking” and “sticking” conditions.....	137
Figure A-1. Representative super-resolution occupancy maps of HSA on TMS, FS and OEG surfaces at different HSA area fractions	165
Figure A-2. Representative super-resolution occupancy maps of HSA on an NH ₂ surface at different area fractions	166
Figure A-3. Super-resolution FRET occupancy maps of donor and acceptor channels on NH ₂ surfaces at different area fractions	166
Figure A-4. Representative super-resolution adsorption maps on FS and NH ₂ surfaces while using different concentrations of tracer HSA	167
Figure B-1. Step size distributions for fluorescently labeled DOPE-LR lipids in DOPC lipid bilayers at different Ca ²⁺ concentrations.....	171
Figure B-2. Histograms of diffusion coefficients for fluorescently labeled DOPE-LR lipids in DOPC lipid bilayers at different Ca ²⁺ concentrations.....	172
Figure B-3. Schematic sketch for the proposed dynamic shifting mechanism.....	172
Figure C-1. Flow curves of the index-matching solvent (isopropyl alcohol/Triton X-100).....	175
Figure C-2. Mean squared displacements versus time plots for 40 nm and 200 nm tracer particles in bulk index-matching solvent	176

Figure C-3. Results from DH-PSF 3D-tracking experiments.....	177
Figure C-4. Trajectories devided into short-retaining and long-retaining groups based on the heat map of normalized residence times	178
Figure C-5. Heat maps showing correlations of normalized mean residence time per length vs. the logarithm of tortuosity for each trajectory for particles in bulk solvent\.....	179
Figure D-1. Representative trajectory maps in PTFE membranes under “reduced-sticking” and “sticking” conditions at different fouling stages.....	180
Figure D-2. Representative trajectory maps of 40 nm tracer particles in a PVDF membrane under “sticking” conditions at different fouling stages.....	181
Figure D-3. Probability distributions of 40 nm tracer particles in a PVDF membrane at different stages of fouling.....	181

Chapter 1

Introduction

Heterogeneity is ubiquitous in all real materials and can affect a number of biotechnologies and bioprocesses. For example, in bioassays and biodevices, surface heterogeneity can cause the formation of strong adsorption sites, which have higher affinities to adsorbate molecules or particles, and can ultimately lead to surface fouling.¹⁻⁵ In filtration processes, heterogeneity in membranes can affect the transport and retention of particles significantly.⁶⁻¹¹ Meanwhile, dynamic heterogeneity of biomolecules (i.e. between conformational states) is often crucial for molecular function.¹²⁻¹⁶ However, these heterogeneous behaviors are challenging to identify using conventional measurements, which usually provide only ensemble average information about adsorption, retention and transport phenomena that happen at interfaces or in confined environments. In comparison, super-resolution single-molecule / particle tracking approaches enable the direct visualization of individual events and allow the observation of detailed spatio-temporal information of heterogeneous behaviors. Specifically, total internal reflection fluorescence (TIRF) microscopy or epifluorescence microscopy are effective techniques to image fluorescent probe molecules and particles at interfaces or in porous materials. The trajectories of individual objects can be further analyzed using automated algorithms, yielding statistically significant results that provide insights into the dynamics of molecules as well as the properties of materials. In this thesis, heterogeneous dynamics of molecules / particles in different scenarios will be discussed, involving protein site

blocking on self-assembled monolayers, cadherin diffusion in supported lipid bilayers and nanoparticle transport in porous membranes.

1.1 HETEROGENEOUS SCENARIOS

1.1.1 Heterogeneous Protein Adsorption and Site Blocking at Solid-Liquid Interfaces

1.1.1.1 Surface properties affect protein adsorption

Proteins are amphiphilic macromolecules comprising moieties with different hydrophobicity, polarity, and electrical charge.¹⁷⁻¹⁹ Given the complex nature of protein molecules, adsorption is affected by a combination of surface properties, including hydrophobicity, surface charge and surface topography.²⁰⁻²⁵ For example, proteins generally exhibit a greater tendency for adsorption to hydrophobic surfaces due to hydrophobic interactions between the surface and protein hydrophobic moieties;^{21, 26-27} charged surfaces can also cause greater protein adsorption because of attractive electrostatic interactions.²⁷⁻²⁸ In order to understand the influences of surface properties on protein adsorption and ultimately control

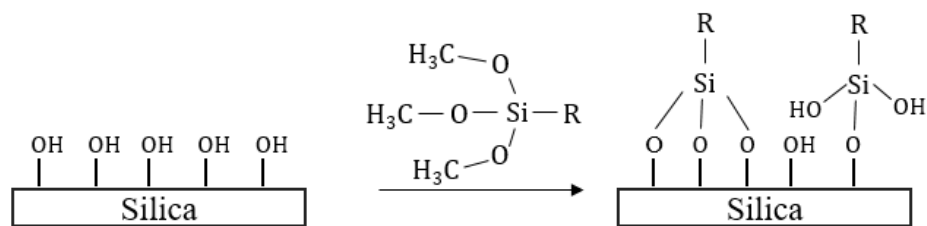


Figure 1-1. Represented schematic diagram showing silanization mechanism on a silica substrate. R represents functional group. Possible chemical heterogeneity is shown in the diagram.

protein adsorption, one way to create protein-compatible surface properties (i.e. with different hydrophobicity, charge and structure profiles) is to silanize surface hydroxyl groups on silica wafers.^{20, 22, 29-31} The mechanism of silica silanization is shown in **Figure 1-1**.

Each protein possesses unique properties and functions that are determined by its chemical composition and structure. While some proteins (e.g. lysozyme) are more rigid and stable in their natural conformations, other “softer” proteins (e.g. serum albumin) are more likely to adsorb to surfaces and undergo conformational changes when interacting with surfaces or other molecules.³²⁻³⁴ Unfortunately, this non-specific protein adsorption is a ubiquitous phenomenon and it can reduce the sensitivity or efficacy of a number of devices and biotechnologies (e.g. biosensors, chromatography, membrane separations, biomaterials).^{2-3, 35-41}

1.1.1.2 Site blocking on heterogeneous surfaces

All real surfaces are spatially heterogeneous. Even very finely polished fused silica wafers have unavoidable surface roughness.⁴² Additionally, as discussed above, when modifying surfaces with silanes, it is impossible to achieve perfectly homogeneous self-assembled monolayers. As shown in **Figure 1-1**, it is highly likely to have chemical heterogeneity (e.g. unreacted hydroxyl on silica substrate or from silanes) on surfaces via silanization reactions.⁴³ As a result, topographical and chemical heterogeneities are inevitable on surfaces, potentially causing isolated strong binding sites.^{22, 25, 41} Compared to the properties of an average surface location, those strong binding sites tend to have higher affinities to adsorbates (i.e. they can potentially cause more adsorption events and retain adsorbates for longer times) and can ultimately lead to surface fouling.^{25, 41, 44-45} Therefore, reducing surface heterogeneity is crucial in terms of

mitigating non-ideal protein adsorption. One common approach to reduce surface heterogeneity used in bioassays and biodevices involves introducing a blocking agent (often protein molecules) to surfaces so that the blocking agent can occupy surface strong sites and make the surface more homogeneous.^{1, 3-4, 46} Serum albumin is a type of protein that is frequently used as a blocking agent.⁴ However, as discussed above, serum albumin is relatively unstable and tends to denature at interfaces, which potentially raises the possibility of protein cluster formation. In some cases, depending on the details of surface chemistry and solution formulation, excessive use of blocking agent can elicit the undesirable creation of protein oligomers / aggregates, which could serve as new adsorption sites and make the surface more heterogeneous.^{25, 30-31}

1.1.2 Heterogeneous Protein Dynamics on Supported Lipid Bilayers

1.1.2.1 Cadherin conformations

Cadherins are a type of transmembrane proteins with their major function being the mediation of cell adhesion.⁴⁷ The name “cadherin” comes from “calcium-dependent adhesion”, and obviously, they are highly dependent on Ca^{2+} ions to activate their adhesive functions.^{14, 47-49} Cadherins have a specific elongated structure with five extracellular domains as shown in **Figure 1-2**. Between each of the two individual extracellular domains, there are binding sites for Ca^{2+} ions. Cadherin structure is extremely sensitive to Ca^{2+} ions: upon the binding of Ca^{2+} ions, the conformation of cadherins becomes more rigid and their functions can be enabled; on the other hand, when Ca^{2+} ions dissociate from cadherins, their conformations become more flexible and compact, and they are no longer capable of mediating cell adhesion.^{14, 49-51} It has also been reported that the association between Ca^{2+} ions and cadherins is highly dynamic and reversible.^{14,}

^{47-48, 52} Considering the high reversibility of cadherin structure, it is likely that heterogeneous denatured conformational status are present in Ca^{2+} -deficient environments.

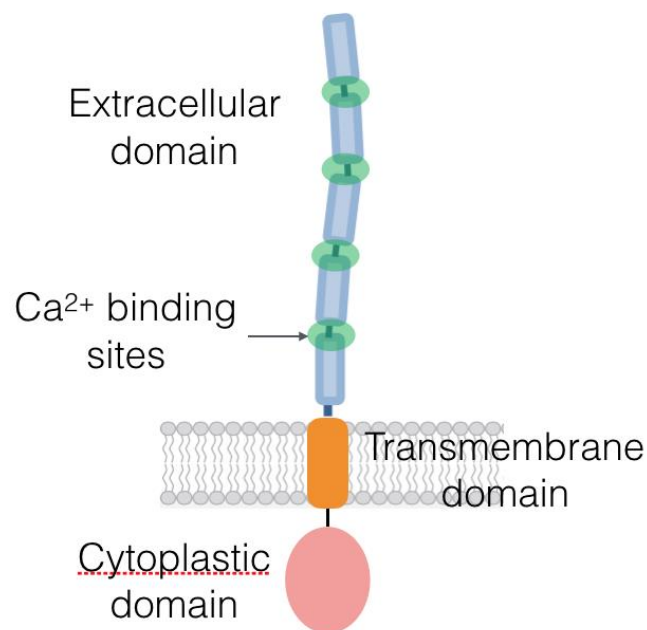


Figure 1-2. Diagram of general cadherin structure (including the extracellular, transmembrane and cytoplasmic domains). Binding sites for Ca^{2+} ions (shown in green) are located between individual extracellular domains.

1.1.2.2 Molecular diffusion associated with supported lipid bilayers

Cadherins are transmembrane proteins that exist on biological membranes, which are essentially complex lipid bilayers, and their transport in association with biomembranes can be significantly affected by their conformations.⁵³ The transport of cadherins can ultimately affect their function in terms of interactions within and between membranes, and junction formation.^{52, 54-56} Since the effective viscosity of lipid bilayers is much higher (i.e. ~2 orders of magnitude) than the viscosity of aqueous solution, when lipid-anchored molecules are diffusing in association with supported lipid bilayers, the majority of resistance comes from the friction between lipids.^{53, 57-58} In accordance with the Stokes–Einstein relation, the diffusion coefficient is inversely related to the hydrodynamic radius of the diffusing object.⁵⁹ As a result, the diffusion coefficient of lipid-anchored molecules is largely determined by the number of lipids that are moving together as a patch, which can be caused by their interactions with lipid-anchored macromolecules. For instance, if a molecule interacts with only one lipid, the apparent diffusion coefficient for the molecule should be similar to the diffusion coefficient of a single membrane-bound lipid. However, if a molecule associates with more than one lipid simultaneously, the corresponding diffusion coefficient for the molecule should be smaller since a group of lipids can contribute an effectively larger hydrodynamic radius.⁶⁰⁻⁶¹

As discussed above, multiple denatured conformational status of cadherin ectodomains might be present in Ca^{2+} -deficient environments. Consequently, it is likely that the apparent diffusion of cadherin on a supported lipid bilayer is heterogeneous due to the fact that cadherin molecules in different conformational structures can interact with different numbers of lipids.

Meanwhile, the highly dynamic nature of cadherin structure can make diffusive behaviors even more complex.⁶⁰

1.1.3 Heterogeneous Particle Transport in Porous Media

1.1.3.1 Membrane tortuosity and spatiotemporal heterogeneity.

Hindered mass transport is essential to water filtration processes and has been studied intensively for decades.^{9, 62-64} However, since particles can follow complex pathways and experience heterogeneous environments when flowing through filtration membranes, there are no existing universal models capable of predicting mass transport quantitatively. Tortuosity is an important parameter that can be used to quantify the complexity of pathways and predict mass transport in porous materials.⁶⁵⁻⁶⁸ As shown in **Figure 1-3**, tortuosity is defined geometrically by the ratio of the contour length to the end-to-end distance (i.e. Euclidean length) of pathways.⁶⁵ Apparently, greater tortuosity values are associated with more meandering pathways. One explicit way of characterizing the relevant tortuosity of membrane would be calculating the apparent tortuosity of actual particle trajectories in membrane.

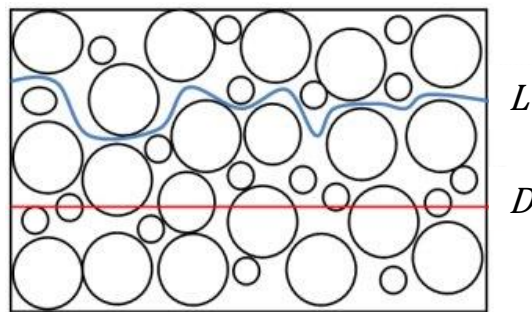


Figure 1-3. Diagram showing the contour length of a pathway (L) and the end-to-end distance of the corresponding pathway (D) in a porous media.

Actual filtration membranes usually have broad pore size distributions.⁶⁹⁻⁷¹ As a result, the transport behaviors of particles can vary dramatically when they pass through different membrane regions and pathways. In principle, particles experience higher resistance when they are breaking through small constrictions; they are likely to linger inside constrictions and their trajectories appear to be more tortuous. In contrast, particles can flow through large openings more easily without being retained long times. Moreover, the effects of local environment on particle transport are highly dependent on operating conditions. For example, one would expect that larger particles are more likely to be affected by small constrictions in a membrane, since constrictions that can confine larger particles may not confine smaller particles. Additionally, the confining effects can be attenuated with increasing flow rate, since particles have greater momentum to break through constrictions at higher flow rates. As discussed above, the transport behaviors of particles are highly dependent on heterogeneous structures within membranes as well as on operating conditions, and the spatiotemporally heterogeneous transport is instrumental to the performance of filtration membranes.⁷²

1.1.3.2 Membrane fouling

In actual filtration processes, it is inevitable to have particles deposited inside membrane pores over time, which can cause severe flux decline and affect the performance of separations.⁷³⁻⁷⁵ With decades of studies on membrane fouling, researchers have developed multiple models to describe fouling processes.^{6, 76-82} Being affected by a number of factors, including particle–particle and particle–surface interactions, membrane structure, physical

properties of particle and solution concentration, fouling processes in membrane can be either locally homogeneous or heterogeneous. Specifically, the “pore-narrowing” model describes a type of homogeneous fouling processes in which internal pathways in membranes are gradually narrowed; the “pore-blocking” model, on the other hand, describes spatially heterogeneous blockage of a subset of pathways in a membrane.⁷⁷⁻⁷⁸ Depending on the mechanism that dominates fouling process, the separation efficacy of membrane can be affected in different ways.

1.2 CHALLENGES IN CHARACTERIZING HETEROGENEOUS DYNAMICS

While heterogeneous dynamics at interfaces are present in all types of bio-applications, they are, unfortunately, challenging to resolve with conventional techniques. For example, when evaluating protein adsorption and site-blocking efficacy at solid–liquid interfaces, conventional methods (e.g., quartz crystal microbalance, surface plasmon resonance, and X-ray photoelectron spectroscopy) provide only ensemble-averaged information of protein remains on surfaces without offering detailed information regarding surface spatial heterogeneity.^{32, 42, 83} Additionally, these methods are solely static measurements of surface properties and fail to characterize dynamic site-blocking processes at different stages.

As discussed in Section 1.1.2, conformational dynamics of transmembrane proteins (e.g. cadherins) on supported lipid bilayers are crucial to their function-enabling transport and interactions. Circular dichroism spectroscopy is commonly used to study the conformations of cadherin extracellular domain.^{14, 84} However, this technique gives information only about the average conformation of cadherin in solution and cannot resolve the presence of multiple molecular populations or the dynamic heterogeneity of individual molecules. It also does not

account for cadherin–lipid interactions which can significantly affect the dynamic conformational changes of cadherin extracellular domains. As a result, it is challenging to obtain detailed and dynamic information of cadherin conformations while they are associating with lipid bilayers.

When it comes to transport in 3D environments, it is also difficult to resolve heterogeneity in filtration membranes and the resulting heterogeneous particle transport with conventional characterization methods. In terms of membrane tortuosity, common approaches (e.g. analyzing static images of materials, measuring the self-diffusion coefficient of tracers in stagnant condition, or employing computational methods based on mathematical models) measure only the average structural tortuosity of membrane under stagnant conditions and do not provide any information regarding the spatial heterogeneity in membrane.^{65, 85-87} Also, while the functional tortuosity is determined by actual pathways in membrane, it is highly dependent on operating conditions (i.e. flow rate and particle size), whose effects are not identified using conventional approaches. Another transport property which is important to the performance of membranes relates to the retention of particles in membrane. Unfortunately, none of the methods mentioned above is capable of resolving the temporal heterogeneity of particle transport.

In order to identify fouling mechanisms during filtration processes, the most common approach is to measure the permeate flux as a function of time, then determine the most likely fouling mechanism(s) by comparing experimental flux curves to parameterized mathematical models describing certain schemes.^{6, 77-79} Obviously, this approach provides very limited and indirect information about fouling processes and is highly model-dependent. However, as discussed in Section 1.1.3, fouling processes are greatly affected by the local structure of

membrane as well as interactions between particles and surface and can therefore be spatially heterogeneous and complicated to understand. While the evolution of available pathways and particle velocity in membrane are crucial for us to understand the corresponding fouling mechanisms, they cannot be detected with the conventional model-fitting approach.

1.3 TRACKING MOLECULES AND PARTICLES WITH FLUORESCENCE MICROSCOPY

1.3.1 Single Molecule Detection at Interfaces

The detection of single molecules can push analytical sensitivity to the ultimate limit. A dramatic advantage of single molecule techniques is the capability to resolve the heterogeneity of molecular behavior, which is usually neglected in ensemble-averaging techniques. Real-time visualization of individual molecules can provide direct insights into interfacial molecular dynamics, including adsorption, diffusion, retention and association.^{29, 88-89}

Fluorescence microscopy is a primary research tool to detect probe molecules at extremely low concentrations. When labeled with fluorophore(s), individual molecules of interest can be directly imaged with fluorescence microscopy. By tracking and analyzing hundreds of thousands of individual molecular trajectories, one can obtain detailed information of different types of heterogeneous dynamics. For example, when studying protein site-blocking behaviors at solid-liquid interfaces, surface heterogeneity can be resolved by mapping the adsorption events and residence times of many individual molecules.^{22, 25, 41} Associations between molecules can also be resolved when coupling fluorescence microscopy with the intermolecular Förster Resonance Energy Transfer (FRET) technique, which will be discussed in

Section 1.3.3.^{22, 30-31} Furthermore, since molecular behaviors can be recorded in real-time throughout entire processes, this single-molecule tracking approach provides insights into the dynamic progression corresponding to site-blocking mechanisms. Additionally, the single-molecule tracking approach can be used to understand conformational dynamics of membrane proteins while they are diffusing within supported lipid bilayers. In particular, by tracking the diffusive behaviors of cadherin ectodomains on supported lipid bilayers, the potential population or dynamic heterogeneity caused by associations between cadherin and lipids at the interfaces can be resolved, providing dynamic conformational information about cadherin ectodomains.⁶⁰ Imaging and tracking techniques enabling the visualization and analyses of individual molecules are discussed below in more details.

1.3.2 Total Internal Reflection Fluorescence Microscopy (TIRFM)

Total internal reflection fluorescence microscopy (TIRFM) is commonly employed to obtain single-molecule sensitivity at interfaces. The schematic diagram of a TIRF microscope is shown in **Figure 1-4**. Basically, this technique takes advantage of the total internal reflection phenomenon, which occurs when a propagated light strikes a boundary between two dielectric media (from the medium with a higher refractive index) at an angle larger than a particular critical angle.⁸⁸ Based on the Snell's law, the critical angle is calculated using the equation

$$\theta_c = \arcsin\left(\frac{n_2}{n_1}\right) \quad (\text{Eq. 1-1})$$

where n_1 and n_2 are the refractive indices of the two media between which total internal reflection occurs. In our experimental setup, incident light propagates through glass (refractive

index = 1.52) and is totally internally reflected at the glass–water (refractive index = 1.33) interface. Consequently, the evanescent electric field generated at the glass–water interface decays exponentially from the interface and selectively illuminates fluorophores in a restricted region that is immediately adjacent to the interface. Therefore, fluorescent signals from bulk solvent are greatly reduced and molecular interfacial behaviors can be strongly emphasized with the application of TIRFM.

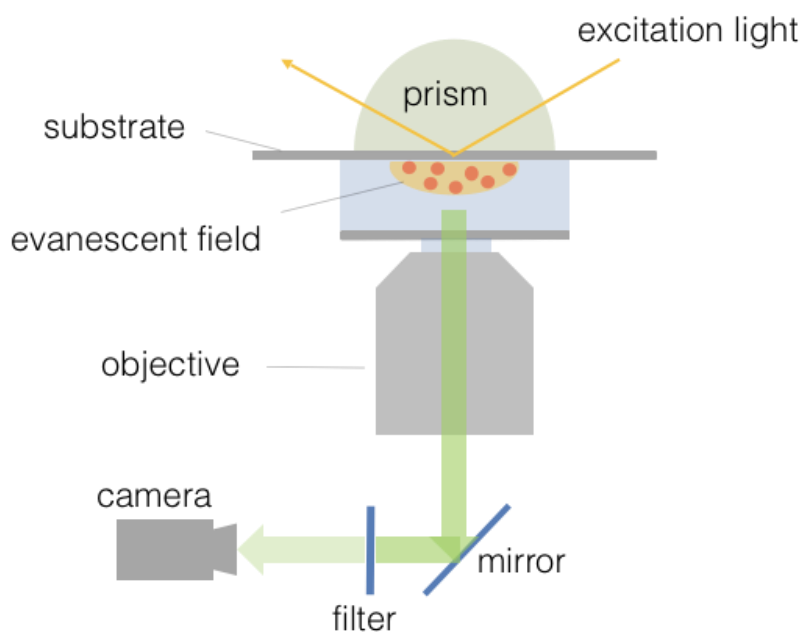


Figure 1-4. Schematic diagram of a prism-based total internal reflection fluorescence (TIRF) microscope.

Single-molecule TIRFM permits the acquisition of detailed spatiotemporal information of molecular dynamics at interfaces. Specifically, it can be used to identify surface adsorption / desorption events and molecular residence times.^{22, 89} Such information can further be applied to quantitatively characterize surface heterogeneity and strong binding sites as discussed in Section

1.1.1. Additionally, TIRFM is advantageous when applied to characterize the motions of anchored membrane proteins on supported lipid bilayers since the signals from free-moving proteins in solution can be largely eliminated.⁶⁰

1.3.3 Förster Resonance Energy Transfer (FRET)

Förster Resonance Energy Transfer (FRET) is a phenomenon that can be used to characterize the nanoscale distance between two fluorophores. As illustrated in **Figure 1-5**, when the emission spectrum of a donor fluorophore (with shorter excitation / emission wavelengths) overlaps with the adsorption spectrum of an acceptor fluorophore (with longer excitation / emission wavelengths), resonant energy transfer can occur from the excited state of the donor to the acceptor. The efficiency of energy transfer is determined by the donor-to-acceptor separation distance r (along with other factors), which can be described by the following equation

$$E = \frac{1}{1 + \left(\frac{r}{R_0}\right)^6} \quad (\text{Eq. 1-2})$$

where R_0 is the so-called Förster distance of the donor-acceptor pair. Therefore, the distance between donor and acceptor fluorophores can be identified quantitatively by measuring the FRET efficiency.

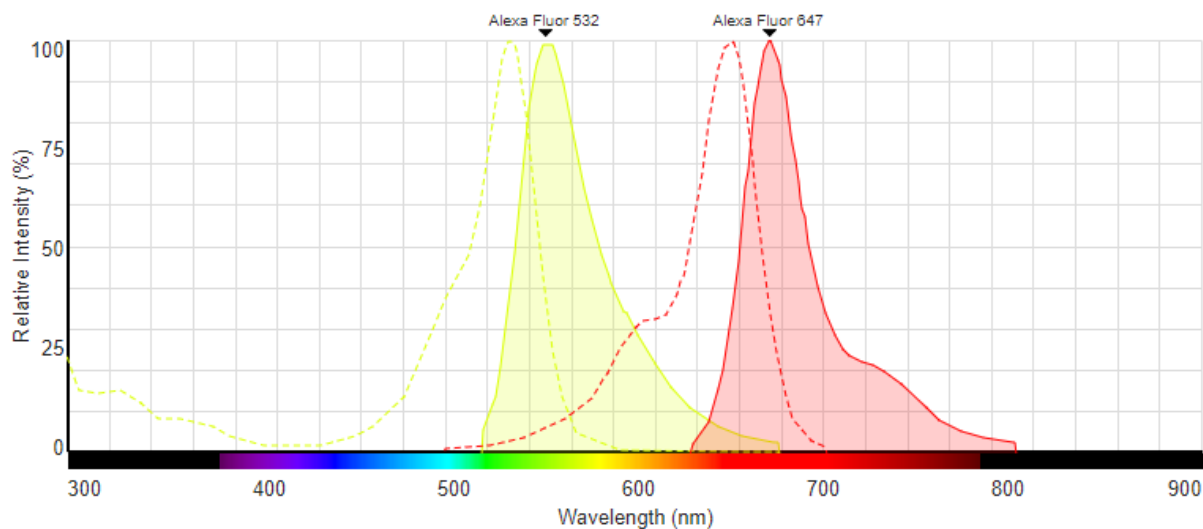


Figure 1-5. Spectra of donor (Alexa Fluor 532) and acceptor (Alexa Fluor 647) fluorophores for Förster Resonance Energy Transfer. The emission spectrum of donor fluorophore (light yellow shade) overlaps with the excitation spectrum of the acceptor fluorophore (red dash line).

As discussed in Section 1.1.1, depending on surface chemistry and the resulting orientation / conformation of blocking agent molecules, protein clusters can potentially emerge during site-blocking processes. Intermolecular FRET is an effective technique to identify the formation of protein clusters. With protein molecules labeled with either donor or acceptor fluorophores, significant FRET signals can be detected when “donor protein” and “acceptor protein” adsorb to surface locations that are close enough to each other (i.e. within a few Ångstroms), which indicates protein–protein associations.^{22, 30-31} Since only donor signals can be observed when donor and acceptor protein molecules adsorb to different surface sites, the illumination of acceptor fluorophores can be used as a signature of protein aggregation on surfaces. Schematic diagrams of intermolecular FRET in site-blocking processes are shown in **Figure 1-6.**

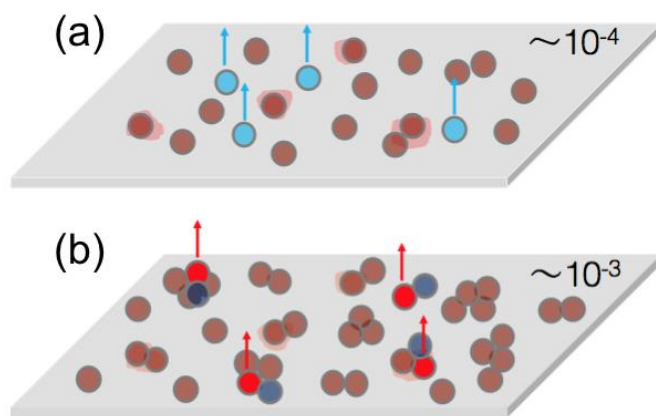


Figure 1-6. Schematic diagrams of intermolecular FRET events on surface at different surface coverages. Blue circles represent donor molecules and red circles represent acceptor molecules. (a) At a surface coverage of $\sim 10^{-4}$, donor molecules and acceptors adsorb to different sites and only donor fluorophores are excited. (b) At a surface coverage of $\sim 10^{-3}$, donor molecules adsorb to locations that are already occupied by acceptor molecules, which causes the transfer of energy and the illumination of acceptor fluorophores.

1.3.4 Tracking Nanoparticles in Porous Media

In addition to tracking single molecules at interfaces, fluorescence microscopy also allows the tracking of nanoparticles in porous media. Specifically, this is a powerful technique to study complex mass transport in filtration processes.^{72, 90} The schematic diagram of the corresponding experimental setup is shown in **Figure 1-7**. To image fluorescent tracer nanoparticles that are suspended in polymer membrane, epifluorescence microscopy is used to illuminate tracer particles. In order to enable the penetration of excitation light into the media and to minimize light scattering from internal interfaces, the liquid used in this approach must

have a refractive index that matches the refractive index of the membrane material.^{10, 91} By precisely engineering the relative proportions of liquid mixtures, the refractive indices of a wide range of polymer materials can be properly matched. In experiments, tracer particle solution is forced into a flow cell by pressure and flows across the membrane sample. The visualization of actual nanoparticle trajectories permits the identification of spatial and temporal heterogeneities of particle transport in membrane, as well as provides direct evidence for potential heterogeneous fouling mechanisms.

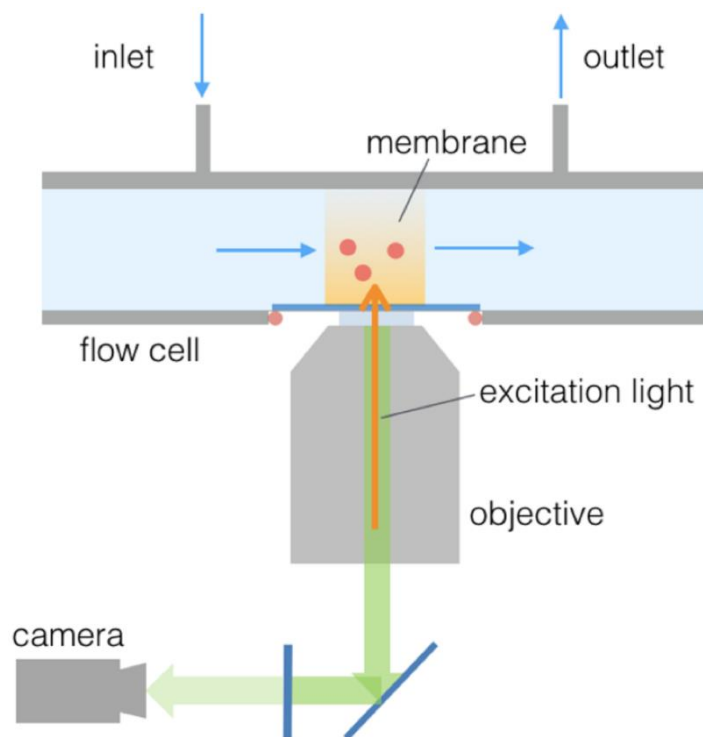


Figure 1-7. Schematic diagram of an epifluorescence microscope used to image nanoparticle transport in a flow cell.

1.4 GOALS AND OBJECTIVES

The overall strategy of this work was to apply super-resolution single-molecule / particle tracking methods to study heterogeneous behaviors of probes of interests in confined environments and obtain insightful understandings of relevant bioprocesses and biotechnologies. Novel statistical approaches were developed and performed to analyze massive datasets obtained with the tracking technique and resolve detailed spatio-temporal behaviors of molecules or particles. Specifically, the following objectives were addressed.

1.4.1 Surface Heterogeneity

The first objective was to identify molecular dynamics of serum albumin on model surfaces at different surface coverages and construct super-resolution maps to quantify surface heterogeneity and site-blocking efficacy. This approach provided effective references for the use of blocking agent in a variety of applications.

1.4.2 Molecular Dynamic Heterogeneity

We aimed to study the heterogeneous dynamics of cadherin on model supported lipid bilayers under different Ca^{2+} levels and obtain detailed information about the connection between diffusion and conformational changes of cadherin.

1.4.3 Transport Heterogeneity

The objective here was to develop a single-particle tracking approach to track tracer particles in filtration membrane under various flow conditions and quantify functional properties of membranes, including functional tortuosity, particle retention, spatio-temporal heterogeneity and detailed fouling mechanisms.

In the following chapters, the objectives above will be addressed in detail. In Chapter 2, single-molecule tracking and super-resolution mapping was employed to investigate the evolution of surface heterogeneity in site-blocking processes, addressing the first objective. Targeting the second objective, heterogeneous diffusion and dynamics of cadherin on supported bilayers will be carefully discussed in Chapter 3. Chapters 4 and 5 focus on the development of single-particle tracking approach in order to study heterogeneous particle transport in filtration membranes to address the third objective. Specifically, membrane functional tortuosity and spatio-temporal heterogeneity will be discussed in Chapter 4, with Chapter 5 discussing distinct fouling mechanisms in membranes.

1.5 REFERENCES

1. Miller-Jaster, K. N.; Petrie Aronin, C. E.; Guilford, W. H., A Quantitative Comparison of Blocking Agents in the In Vitro Motility Assay. *Cell. Mol. Bioeng.* **2011**, 5 (1), 44-51.
2. Shiddiky, M. J.; Kithva, P. H.; Kozak, D.; Trau, M., An electrochemical immunosensor to minimize the nonspecific adsorption and to improve sensitivity of protein assays in human serum. *Biosens. Bioelectron.* **2012**, 38 (1), 132-7.
3. Wang, S.; Yong, W.; Liu, J.; Zhang, L.; Chen, Q.; Dong, Y., Development of an indirect competitive assay-based aptasensor for highly sensitive detection of tetracycline residue in honey. *Biosens. Bioelectron.* **2014**, 57, 192-8.
4. Xiao, Y.; Isaacs, S. N., Enzyme-linked immunosorbent assay (ELISA) and blocking with bovine serum albumin (BSA)--not all BSAs are alike. *J. Immunol. Methods* **2012**, 384 (1-2), 148-51.
5. Zhang, B.; Wang, X.; Liu, F.; Cheng, Y.; Shi, D., Effective reduction of nonspecific binding by surface engineering of quantum dots with bovine serum albumin for cell-targeted imaging. *Langmuir* **2012**, 28 (48), 16605-13.

6. Bolton, G.; LaCasse, D.; Kuriyel, R., Combined models of membrane fouling: development and application to microfiltration and ultrafiltration of biological fluids. *J. Membr. Sci.* **2006**, *277* (1), 75-84.
7. Gao, W.; Liang, H.; Ma, J.; Han, M.; Chen, Z.-l.; Han, Z.-s.; Li, G.-b., Membrane fouling control in ultrafiltration technology for drinking water production: a review. *Desalination* **2011**, *272* (1), 1-8.
8. Maruyama, T.; Katoh, S.; Nakajima, M.; Nabetani, H., Mechanism of bovine serum albumin aggregation during ultrafiltration. *Biotechnology and bioengineering* **2001**, *75* (2), 233-238.
9. O'Melia, C. R., Particles, pretreatment, and performance in water filtration. *J. Environ. Eng.* **1985**, *111* (6), 874-890.
10. Skaug, M. J.; Schwartz, D. K., Tracking nanoparticle diffusion in porous filtration media. *Ind. Eng. Chem. Res.* **2015**, *54* (16), 4414-4419.
11. Stevenson, D., Flow and filtration through granular media—The effect of grain and particle size dispersion. *Water Res.* **1997**, *31* (2), 310-322.
12. Deis, L. N.; Wu, Q.; Wang, Y.; Qi, Y.; Daniels, K. G.; Zhou, P.; Oas, T. G., suppression of conformational heterogeneity at a protein-protein interface. *Proc. Natl. Acad. Sci. U. S. A.* **2015**, *112* (29), 9028-9033.
13. Morrissey, B. W.; Stromberg, R. R., The conformation of adsorbed blood proteins by infrared bound fraction measurements. *J. Colloid Interface Sci.* **1974**, *46* (1), 152-164.
14. Pokutta, S.; Herrenknecht, K.; Kemler, R.; ENGEL, J., Conformational changes of the recombinant extracellular domain of E-cadherin upon calcium binding. *European journal of biochemistry* **1994**, *223* (3), 1019-1026.
15. Thakur, G.; Jiang, K.; Lee, D.; Prashanthi, K.; Kim, S.; Thundat, T., Investigation of pH-induced protein conformation changes by nanomechanical deflection. *Langmuir* **2014**, *30* (8), 2109-16.
16. Xie, Z.; Srividya, N.; Sosnick, T. R.; Pan, T.; Scherer, N. F., Single-molecule studies highlight conformational heterogeneity in the early folding steps of a large ribozyme. *Proc. Natl. Acad. Sci. U. S. A.* **2004**, *101* (2), 534-9.

17. Leckband, D.; Prakasham, A., Mechanism and dynamics of cadherin adhesion. *Annu. Rev. Biomed. Eng.* **2006**, 8, 259-287.
18. Bloomfield, V., The Structure of Bovine Serum Albumin at Low pH*. *Biochemistry* **1966**, 5 (2), 684-689.
19. Carter, D. C.; Ho, J. X., Structure of serum albumin. *Adv. Protein Chem.* **1994**, 45 (45), 153-203.
20. Luik, A.; Naboka, Y. N.; Mogilevich, S.; Hushcha, T.; Mischenko, N., Study of human serum albumin structure by dynamic light scattering: two types of reactions under different pH and interaction with physiologically active compounds. *Spectrochim. Acta Mol. Biomol. Spectrosc.* **1998**, 54 (10), 1503-1507.
21. Aissaoui, N.; Bergaoui, L.; Landoulsi, J.; Lambert, J. F.; Boujday, S., Silane layers on silicon surfaces: mechanism of interaction, stability, and influence on protein adsorption. *Langmuir* **2012**, 28 (1), 656-65.
22. Allen, L. T.; Tosetto, M.; Miller, I. S.; O'Connor, D. P.; Penney, S. C.; Lynch, I.; Keenan, A. K.; Pennington, S. R.; Dawson, K. A.; Gallagher, W. M., Surface-induced changes in protein adsorption and implications for cellular phenotypic responses to surface interaction. *Biomaterials* **2006**, 27 (16), 3096-108.
23. Cai, Y.; Schwartz, D. K., Influence of protein surface coverage on anomalously strong adsorption sites. *ACS Appl. Mater. Interfaces* **2015**, 8 (1), 511-520.
24. Chatelier, R. C.; Minton, A. P., Adsorption of globular proteins on locally planar surfaces: models for the effect of excluded surface area and aggregation of adsorbed protein on adsorption equilibria. *Biophys. J.* **1996**, 71 (5), 2367.
25. Hartvig, R. A.; van de Weert, M.; Ostergaard, J.; Jorgensen, L.; Jensen, H., Protein adsorption at charged surfaces: the role of electrostatic interactions and interfacial charge regulation. *Langmuir* **2011**, 27 (6), 2634-43.
26. Langdon, B. B.; Mirhossaini, R. B.; Mabry, J. N.; Sriram, I.; Lajmi, A.; Zhang, Y.; Rojas, O. J.; Schwartz, D. K., Single-molecule resolution of protein dynamics on polymeric membrane surfaces: the roles of spatial and population heterogeneity. *ACS Appl. Mater. Interfaces* **2015**, 7 (6), 3607-17.

27. Monserud, J. H.; Schwartz, D. K., Effects of molecular size and surface hydrophobicity on oligonucleotide interfacial dynamics. *Biomacromolecules* **2012**, *13* (12), 4002-4011.
28. Wong, S. Y.; Han, L.; Timachova, K.; Veselinovic, J.; Hyder, M. N.; Ortiz, C.; Klibanov, A. M.; Hammond, P. T., Drastically lowered protein adsorption on microbicidal hydrophobic/hydrophilic polyelectrolyte multilayers. *Biomacromolecules* **2012**, *13* (3), 719-26.
29. McUmbur, A. C.; Randolph, T. W.; Schwartz, D. K., Electrostatic Interactions Influence Protein Adsorption (but Not Desorption) at the Silica-Aqueous Interface. *J. Phys. Chem. Lett.* **2015**, *6* (13), 2583-7.
30. Kastantin, M.; Schwartz, D. K., Identifying multiple populations from single-molecule lifetime distributions. *Chemphyschem* **2013**, *14* (2), 374-80.
31. Langdon, B. B.; Kastantin, M.; Schwartz, D. K., Surface Chemistry Influences Interfacial Fibrinogen Self-Association. *Biomacromolecules* **2015**, *16*, 3201-3208.
32. Langdon, B. B.; Kastantin, M.; Walder, R.; Schwartz, D. K., Interfacial protein-protein associations. *Biomacromolecules* **2014**, *15* (1), 66-74.
33. Rabe, M.; Verdes, D.; Seeger, S., Understanding protein adsorption phenomena at solid surfaces. *Adv. Colloid Interface Sci.* **2011**, *162* (1-2), 87-106.
34. Rabe, M.; Verdes, D.; Seeger, S., Understanding cooperative protein adsorption events at the microscopic scale: a comparison between experimental data and Monte Carlo simulations. *J. Phys. Chem. B* **2010**, *114* (17), 5862-5869.
35. Arai, T.; Norde, W., The behavior of some model proteins at solid-liquid interfaces 1. Adsorption from single protein solutions. *Colloids Surf.* **1990**, *51*, 1-15.
36. Banerjee, I.; Pangule, R. C.; Kane, R. S., Antifouling coatings: recent developments in the design of surfaces that prevent fouling by proteins, bacteria, and marine organisms. *Adv. Mater.* **2011**, *23* (6), 690-718.
37. Bhambure, R.; Sharma, I.; Pattanayek, S. K.; Rathore, A. S., Qualitative and quantitative examination of non-specific protein adsorption on filter membrane disks of a commercially available high throughput chromatography device. *J. Membr. Sci.* **2014**, *451*, 312-318.
38. Bowen, W.; Calvo, J.; Hernandez, A., Steps of membrane blocking in flux decline during protein microfiltration. *J. Membr. Sci.* **1995**, *101* (1-2), 153-165.

39. Sun, S.; Yue, Y.; Huang, X.; Meng, D., Protein adsorption on blood-contact membranes. *J. Membr. Sci.* **2003**, 222 (1-2), 3-18.
40. Wang, L.; Cai, Y.; Jing, Y.; Zhu, B.; Zhu, L.; Xu, Y., Route to hemocompatible polyethersulfone membranes via surface aminolysis and heparinization. *J. Colloid Interface Sci.* **2014**, 422, 38-44.
41. Charmas, B.; Leboda, R., Effect of surface heterogeneity on adsorption on solid surfaces: application of inverse gas chromatography in the studies of energetic heterogeneity of adsorbents. *J. Chromatogr. A* **2000**, 886 (1), 133-152.
42. Mabry, J. N.; Skaug, M. J.; Schwartz, D. K., Single-molecule insights into retention at a reversed-phase chromatographic interface. *Anal. Chem.* **2014**, 86 (19), 9451-8.
43. Rimola, A.; Costa, D.; Sodupe, M.; Lambert, J. F.; Ugliengo, P., Silica surface features and their role in the adsorption of biomolecules: computational modeling and experiments. *Chem. Rev.* **2013**, 113 (6), 4216-313.
44. Sindorf, D. W.; Maciel, G. E., Solid-state NMR studies of the reactions of silica surfaces with polyfunctional chloromethylsilanes and ethoxymethylsilanes. *J. Am. Chem. Soc.* **1983**, 105 (12), 3767-3776.
45. Sengupta, P.; Jovanovic-Talisman, T.; Skoko, D.; Renz, M.; Veatch, S. L.; Lippincott-Schwartz, J., Probing protein heterogeneity in the plasma membrane using PALM and pair correlation analysis. *Nat. Methods* **2011**, 8 (11), 969-75.
46. Gritti, F.; Guiochon, G., Heterogeneity of the adsorption mechanism of low molecular weight compounds in reversed-phase liquid chromatography. *Anal. Chem.* **2006**, 78 (16), 5823-34.
47. Hsieh, H. Y.; Wang, P. C.; Wu, C. L.; Huang, C. W.; Chieng, C. C.; Tseng, F. G., Effective enhancement of fluorescence detection efficiency in protein microarray assays: application of a highly fluorinated organosilane as the blocking agent on the background surface by a facile vapor-phase deposition process. *Anal. Chem.* **2009**, 81 (19), 7908-16.
48. Leckband, D.; de Rooij, J., Cadherin adhesion and mechanotransduction. *Annual review of cell and developmental biology* **2014**, 30, 291-315.
49. Koch, A. W.; Pokutta, S.; Lustig, A.; Engel, J., Calcium binding and homoassociation of E-cadherin domains. *Biochemistry* **1997**, 36 (25), 7697-7705.

50. Maurer, P.; Hohenester, E.; Engel, J., Extracellular calcium-binding proteins. *Current opinion in cell biology* **1996**, 8 (5), 609-617.
51. Brown, E. M.; Vassilev, P. M.; Hebert, S. C., Calcium ions as extracellular messengers. *Cell* **1995**, 83 (5), 679-682.
52. Kim, S. A.; Tai, C.-Y.; Mok, L.-P.; Mosser, E. A.; Schuman, E. M., Calcium-dependent dynamics of cadherin interactions at cell–cell junctions. *Proceedings of the National Academy of Sciences* **2011**, 108 (24), 9857-9862.
53. Knight, J. D.; Lerner, M. G.; Marcano-Velázquez, J. G.; Pastor, R. W.; Falke, J. J., Single molecule diffusion of membrane-bound proteins: window into lipid contacts and bilayer dynamics. *Biophysical journal* **2010**, 99 (9), 2879-2887.
54. Baumgartner, W.; Golenhofen, N.; Grundhöfer, N.; Wiegand, J.; Drenckhahn, D., Ca²⁺ dependency of N-cadherin function probed by laser tweezer and atomic force microscopy. *The Journal of neuroscience* **2003**, 23 (35), 11008-11014.
55. Biswas, K. H.; Hartman, K. L.; Yu, C.-h.; Harrison, O. J.; Song, H.; Smith, A. W.; Huang, W. Y.; Lin, W.-C.; Guo, Z.; Padmanabhan, A., E-cadherin junction formation involves an active kinetic nucleation process. *Proc. Natl. Acad. Sci. U. S. A.* **2015**, 112 (35), 10932-10937.
56. Wu, Y.; Jin, X.; Harrison, O.; Shapiro, L.; Honig, B. H.; Ben-Shaul, A., Cooperativity between trans and cis interactions in cadherin-mediated junction formation. *Proceedings of the National Academy of Sciences* **2010**, 107 (41), 17592-17597.
57. Ziemba, B. P.; Knight, J. D.; Falke, J. J., Assembly of membrane-bound protein complexes: detection and analysis by single molecule diffusion. *Biochemistry* **2012**, 51 (8), 1638-1647.
58. Ziemba, B. P.; Li, J.; Landgraf, K. E.; Knight, J. D.; Voth, G. A.; Falke, J. J., Single-molecule studies reveal a hidden key step in the activation mechanism of membrane-bound protein kinase C- α . *Biochemistry* **2014**, 53 (10), 1697-1713.
59. Edward, J. T., Molecular volumes and the Stokes-Einstein equation. *J. Chem. Educ.* **1970**, 47 (4), 261.
60. Cai, Y.; Shashikanth, N.; Leckband, D. E.; Schwartz, D. K., Cadherin diffusion in supported lipid bilayers exhibits calcium-dependent dynamic heterogeneity. *Biophys. J.* **2016**, 111 (12), 2658-2665.

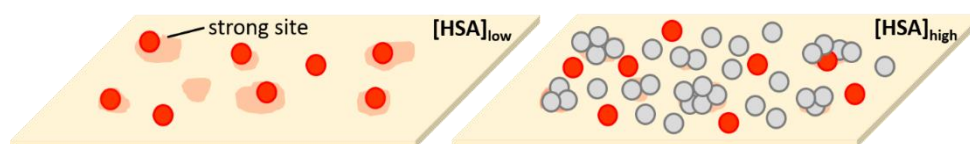
61. Chaparro Sosa, A. F.; Kienle, D. F.; Falatach, R. M.; Flanagan, J.; Kaar, J. L.; Schwartz, D. K., Stabilization of Immobilized Enzymes via the Chaperone-like Activity of Mixed Lipid Bilayers. *ACS Appl. Mater. Interfaces* **2018**.
62. van Reis, R.; Zydney, A., Bioprocess membrane technology. *J. Membr. Sci.* **2007**, 297 (1), 16-50.
63. Shannon, M. A.; Bohn, P. W.; Elimelech, M.; Georgiadis, J. G.; Mariñas, B. J.; Mayes, A. M., Science and technology for water purification in the coming decades. *Nature* **2008**, 452 (7185), 301-310.
64. McDowell-Boyer, L. M.; Hunt, J. R.; Sitar, N., Particle transport through porous media. *Water Resour. Res.* **1986**, 22 (13), 1901-1921.
65. Ghanbarian, B.; Hunt, A. G.; Ewing, R. P.; Sahimi, M., Tortuosity in Porous Media: A Critical Review. *Soil Sci. Soc. Am. J.* **2013**, 77 (5), 1461-1477.
66. David, C., Geometry of flow paths for fluid transport in rocks. *J. Geophys. Res.: Solid Earth* **1993**, 98 (B7), 12267-12278.
67. Koponen, A.; Kataja, M.; Timonen, J., Tortuous flow in porous media. *Phys. Rev. E* **1996**, 54 (1), 406-410.
68. Lee, Y.; Andrade Jr, J. S.; Buldyrev, S. V.; Dokholyan, N. V.; Havlin, S.; King, P. R.; Paul, G.; Stanley, H. E., Traveling time and traveling length in critical percolation clusters. *Phys. Rev. E* **1999**, 60 (3), 3425.
69. Kong, C. S.; Kim, D.-Y.; Lee, H.-K.; Shul, Y.-G.; Lee, T.-H., Influence of pore-size distribution of diffusion layer on mass-transport problems of proton exchange membrane fuel cells. *J. Power Sources* **2002**, 108 (1-2), 185-191.
70. Nakao, S.-i., Determination of pore size and pore size distribution: 3. Filtration membranes. *J. Membr. Sci.* **1994**, 96 (1-2), 131-165.
71. Lee, S.; Park, G.; Amy, G.; Hong, S.-K.; Moon, S.-H.; Lee, D.-H.; Cho, J., Determination of membrane pore size distribution using the fractional rejection of nonionic and charged macromolecules. *J. Membr. Sci.* **2002**, 201 (1-2), 191-201.

72. Cai, Y.; Schwartz, D. K., Mapping the Functional Tortuosity and Spatiotemporal Heterogeneity of Porous Polymer Membranes with Super-Resolution Nanoparticle Tracking. *ACS Appl. Mater. Interfaces* **2017**, 9 (49), 43258-43266.
73. Chang, I.-S.; Le Clech, P.; Jefferson, B.; Judd, S., Membrane fouling in membrane bioreactors for wastewater treatment. *J. Environ. Eng.* **2002**, 128 (11), 1018-1029.
74. Lohaus, J.; Perez, Y.; Wessling, M., What are the microscopic events of colloidal membrane fouling? *J. Membr. Sci.* **2018**.
75. Meng, F.; Chae, S.-R.; Drews, A.; Kraume, M.; Shin, H.-S.; Yang, F., Recent advances in membrane bioreactors (MBRs): membrane fouling and membrane material. *Water Res.* **2009**, 43 (6), 1489-1512.
76. Corbatón-Báguena, M.-J.; Álvarez-Blanco, S.; Vincent-Vela, M.-C., Fouling mechanisms of ultrafiltration membranes fouled with whey model solutions. *Desalination* **2015**, 360, 87-96.
77. Guo, W.; Ngo, H.-H.; Li, J., A mini-review on membrane fouling. *Bioresour. technol.* **2012**, 122, 27-34.
78. Henry, C.; Minier, J.-P.; Lefèvre, G., Towards a description of particulate fouling: From single particle deposition to clogging. *Adv. colloid interface sci.* **2012**, 185, 34-76.
79. Ho, C.-C.; Zydney, A. L., A combined pore blockage and cake filtration model for protein fouling during microfiltration. *J. Colloid Interface Sci.* **2000**, 232 (2), 389-399.
80. Miller, D. J.; Kasemset, S.; Paul, D. R.; Freeman, B. D., Comparison of membrane fouling at constant flux and constant transmembrane pressure conditions. *J. Membr. Sci.* **2014**, 454, 505-515.
81. Qin, W.; Zhang, J.; Xie, Z.; Ng, D.; Ye, Y.; Gray, S. R.; Xie, M., Synergistic effect of combined colloidal and organic fouling in membrane distillation: Measurements and mechanisms. *Environ. Sci.: Water Res. Technol.* **2017**, 3 (1), 119-127.
82. Wang, F.; Tarabara, V. V., Pore blocking mechanisms during early stages of membrane fouling by colloids. *J. Colloid Interface Sci.* **2008**, 328 (2), 464-9.
83. Puddu, V.; Perry, C. C., Peptide Adsorption on Silica Nanoparticles: Evidence of Hydrophobic Interactions. *ACS Nano* **2012**, 6 (7), 6356-6363.

84. Pertz, O.; Bozic, D.; Koch, A. W.; Fauser, C.; Brancaccio, A.; Engel, J., A new crystal structure, Ca^{2+} dependence and mutational analysis reveal molecular details of E-cadherin homoassociation. *The EMBO journal* **1999**, *18* (7), 1738-1747.
85. Nicolay, K.; Braun, K. P.; Graaf, R. A. d.; Dijkhuizen, R. M.; Kruiskamp, M. J., Diffusion NMR spectroscopy. *NMR Biomed.* **2001**, *14* (2), 94-111.
86. Vallabh, R.; Banks-Lee, P.; Seyam, A.-F., New approach for determining tortuosity in fibrous porous media. *J. Eng. Fiber Fabr.* **2010**, *5* (3), 7-19.
87. Vervoort, R.; Cattle, S., Linking hydraulic conductivity and tortuosity parameters to pore space geometry and pore-size distribution. *J. Hydrol.* **2003**, *272* (1), 36-49.
88. Honciuc, A.; Harant, A. W.; Schwartz, D. K., Single-molecule observations of surfactant diffusion at the solution– solid interface. *Langmuir* **2008**, *24* (13), 6562-6566.
89. Walder, R.; Nelson, N.; Schwartz, D. K., Super-resolution surface mapping using the trajectories of molecular probes. *Nat. Commun.* **2011**, *2*, 515.
90. Cai, Y.; Schwartz, D. K., Single-nanoparticle tracking reveals mechanisms of membrane fouling. *J. Membr. Sci.* **2018**.
91. Skaug, M. J.; Wang, L.; Ding, Y.; Schwartz, D. K., Hindered nanoparticle diffusion and void accessibility in a three-dimensional porous medium. *ACS Nano* **2015**, *9* (2), 2148-2156.

Chapter 2

Influence of Protein Surface Coverage on Anomalous Strong Adsorption Sites



Reproduced from Cai, Y. and Schwartz, D. K., *ACS Applied Materials & Interfaces*, **2016**, 8 (1), 511–520.

2.1 ABSTRACT

Serum albumin is commonly used as a blocking agent to reduce nonspecific protein adsorption in bioassays and biodevices; however, the details of this process remain poorly understood. Using single molecule techniques, we investigated the dynamics of human serum albumin (HSA) on four model surfaces as a function of protein concentration. By constructing super-resolution maps, identifying anomalously strong adsorption sites, and quantifying surface heterogeneity, we found that the concentration required for site blocking varied dramatically with surface chemistry. When expressed in terms of protein surface coverage, however, a more consistent picture emerged, where a significant fraction of strong sites were passivated at a fractional coverage of 10^{-4} . On fused silica (FS), “non-fouling” oligo (ethylene glycol) functionalized FS and hydrophobically modified FS, a modest additional site blocking effect

continued at higher coverage. However, on amine-functionalized surfaces, the surface heterogeneity exhibited a minimum at a coverage of $\sim 10^{-4}$. Using intermolecular Förster resonance energy transfer (FRET), we determined that new anomalous strong sites were created at higher coverage on amine surfaces, and that adsorption to these sites was associated with protein-protein interactions, i.e. surface-induced aggregation.

2.2 INTRODUCTION

Nonspecific protein adsorption is a ubiquitous phenomenon that affects a number of biotechnologies such as biosensing,¹⁻³ biomaterials,⁴⁻⁶ membrane separations,⁷⁻⁹ and chromatography¹⁰⁻¹². The undesired attachment of proteins is problematic since it can reduce the sensitivity and efficacy of devices,^{9, 13} or potentially elicit hazardous responses *in vivo*.^{14, 15} One common approach employed to reduce non-specific protein adsorption involves the use of blocking agents.¹⁶ Serum albumin has frequently been used as a blocking agent in bioassays and biodevices, including enzyme-linked immunosorbent assay (ELISA) microwells, *in vitro* motility assays, and field effect transistor (FET) biosensors.^{1, 3, 17-19} When effective, this approach is generally ascribed to the notion of competitive adsorption. However, depending on the details of the surface chemistry and formulation conditions, serum albumin is not always an effective blocking agent, and the details of the process remain poorly understood. In particular, recent studies have revealed the complexity of surface fouling phenomena and emphasized the importance of surface-mediated intermolecular protein-protein associations.²⁰⁻²² Therefore, it seems likely that surface passivation using serum albumin is a complex process, where one

attempts to block strong surface sites that are native to the surface, while avoiding the creation of protein oligomers/aggregates that could serve as new adsorption sites.

Chemical and topographical heterogeneity is unavoidable on any real surface, making it likely that isolated strong binding sites exist for any particular adsorbate species. Compared to the behavior on an average surface location, adsorbate molecules may adsorb at these anomalous sites more frequently, remain adsorbed longer, or both, ultimately leading to non-ideal surface fouling.²²⁻²⁵ A variety of experimental techniques (e.g., quartz crystal microbalance, surface plasmon resonance, and X-ray photoelectron spectroscopy) have been applied to evaluate protein adsorption at solid-liquid interfaces.^{4, 26, 27} However, the ensemble-averaged information provided by these methods provides only indirect insights into the site-blocking process, e.g. they can be as crude tests of *ad hoc* parametric models. Amplitude-modulation (tapping mode) atomic force microscopy (AMAFM) has been used for high-resolution imaging and is sensitive to the population of particularly long-lived protein molecules.^{28, 29} By modifying the cantilever tip with proteins, one can evaluate the strength of protein-surface interactions as well as protein-protein interactions.^{30, 31} This technique provides direct information about surface forces and could hypothetically identify heterogeneous sites on surfaces, although the low-throughput nature of these experiments makes this difficult in practice. In the present work, we employed a complementary single-molecule tracking and surface-mapping approach, which provided detailed spatio-temporal information for large numbers of molecular trajectories, allowing us to quantitatively characterize the heterogeneity of adsorption processes. Specifically, using single-molecule total internal reflection fluorescence microscopy (TIRFM), we identified each adsorption event, enumerated individual strong binding sites, and characterized the heterogeneity of a given surface under relevant conditions (e.g. as the blocking agent concentration was

varied).³² Coupled with intermolecular Förster resonance energy transfer (FRET), which can directly identify protein-protein associations, single-molecule TIRFM provides a powerful approach for the analysis of heterogeneous surface adsorption.²¹

Protein concentration (and therefore surface coverage) is a critical factor in regulating non-specific protein adsorption and surface heterogeneity, and an important focus of the experiments described here. Specifically, we investigated the surface dynamics of human serum albumin (HSA), at different stages of fractional surface coverage on representative surfaces. Four model surfaces were used in our experiments, fused silica (FS), FS modified with a hydrophobic trimethylsilane (TMS) layer, FS modified with a “non-fouling” oligo (ethylene glycol) (OEG) layer,³³ and FS modified to exhibit an amine (NH₂) surface functionality. FS, NH₂ and OEG represented hydrophilic surfaces with negative, positive and neutral surface charge respectively, and TMS represented a model hydrophobic surface. For each type of surface, we performed experiments over a wide range of HSA concentration (7~8 orders of magnitude), providing a systematic picture of the spatial heterogeneity and molecule dynamics as a function of average protein surface coverage. Aside from inhibiting non-specific binding to native surface sites, an ideal blocking agent would also prevent protein-protein interactions. These unwanted interactions were directly identified by the use of intermolecular FRET. The findings presented here will be useful in understanding the complexity of protein adsorption processes and ultimately enhancing the efficacy of site blocking.

2.3 EXPERIMENTAL METHODOLOGY

2.3.1 Surface Preparation and Characterization

Fused silica (FS) wafers (Mark Optics Inc.) were washed with 2 % Micro90 detergent, then immersed in warm piranha solution (~70 °C) for 3 hours. After drying in a nitrogen stream, they were further treated by UV-ozone for 30 minutes. Surfaces with amine groups and OEG monolayers were then prepared via liquid phase deposition by immersing clean FS wafers (pre-treated as described above) in 175 mL toluene solution with 200 μ l N-(6-aminohexyl) aminopropyl trimethoxysilane (Gelest) or methoxy-triethyleneoxy-propyl trimethoxysilane (Gelest) for 2 hours, respectively. Trimethylsilane (TMS) surfaces were prepared by exposing wafers to hexamethyldisilazane (Sigma Aldrich) vapor for 22 hours. For NH₂, OEG and TMS surfaces, wafers were further rinsed with toluene and isopropanol before use. Static water contact angle measurements were performed to characterize the four surfaces. By measuring the static contact angle (reflecting hydrophobicity and macroscopic surface energy) of 6 droplets on random positions on each surface, the measured values for FS surfaces, NH₂ surfaces, OEG surfaces and TMS surfaces were determined to be ~0°, 43 \pm 2°, 18 \pm 3° and 91 \pm 4°, respectively, consistent with previous observations by our group and others.^{22, 34-36}

2.3.2 Protein Solutions

HSA (fatty acid free, globulin free, \geq 99%, Sigma-Aldrich) was labeled with either Alexa Fluor 647 or Alexa Fluor 488,³⁷ and then purified with Zeba spin desalting columns (7K

MWCO).³⁸ Each protein sample solution was purified three times in order to remove salts and other small molecules (i.e. fluorophores). The remaining dye molecules after purification were calculated to be less than 0.01% of that in the original sample solution, and therefore had a negligible statistical influence on our experiments. The concentrations of original protein solutions and the dye/protein ratios were determined by a UV-vis spectrometer; each HSA molecule was labeled with 1.6 dyes on average. No evident change of HSA adsorption affinities to surfaces was observed after protein labeling in our experiments (see Appendix A for supplementary figures). Phosphate buffered saline (pH 7.4, Gibco) was used to prepare all protein solutions. Labeled proteins were used as tracers in extremely low concentrations to achieve the sparse conditions required for single molecule resolution. Unlabeled proteins were further added to adjust the solutions to desired concentrations. The fraction of tracer molecules did not affect the results of our experiments, as shown in **Figure A-4** in Appendix A).

2.3.3 Single-Molecule Tracking

All experiments were performed using a custom-built prism-based total internal reflection fluorescence microscope (TIRFM) as described previously.³⁹ An EMCCD camera (Photometrics) cooled to -95 °C was used to capture images.⁴⁰ Multiple movies (each movie contained 3,000 frames) with an acquisition time of 50 ms were collected for each experimental condition.

2.3.3.1 Single-color concentration-dependent experiments – Tracer proteins labeled with Alexa Fluor 647 were excited by a 647 nm laser with the emission filtered by a 647 nm long pass filter (Semrock). Each experiment was conducted on at least two different sample wafers. On each surface, experiments were performed sequentially from a very low concentration to much

higher concentrations. For each concentration, the surface was incubated for several minutes, and then at least 10 movies were collected over a time period of an hour. No significant change of dynamic protein behavior was observed over this time period suggesting that a steady state was reached relatively quickly. Fluorescent microspheres (0.02 μm , 660/680) were introduced to the surfaces as registration markers as necessary and images were aligned to compensate for drift when processing data.

2.3.3.2 Förster resonance energy transfer – Intermolecular Förster resonance energy transfer (FRET) was used to identify protein-protein associations.²¹ HSA molecules labeled with Alexa Fluor 488 and Alexa Fluor 647 were used as donor molecules and acceptor molecules, respectively. A 491 nm laser was used to illuminate donor fluorophores and no measurable direct excitation of acceptor was observed, due to the large spectral separation. The donor emission was filtered by a band-pass filter centered at 529 nm with a 90% transmission width of 28 nm (Semrock), while the acceptor fluorophores excited by the donors were filtered by a 685 ± 20 nm bandpass filter (Semrock). Dual-channel imaging was attained with an Optosplit II image splitter (Cairn Research) which split the image via a dichroic mirror with a nominal separation wavelength of 610 nm (Chroma). The two channels were manually aligned to within 1-2 pixels with an alignment grid before each experiment, and were further aligned using objects appearing in both channels by a Mathematica program as described previously.⁴¹ Since the Förster radius for the donor-acceptor pair was approximately 5.0 nm,⁴²⁻⁴⁵ and the radius of gyration of HSA was determined to be 2.74 ± 0.04 nm,⁴⁶⁻⁴⁸ energy transfer was very likely to happen when a donor molecule and an acceptor molecule adsorbed to a same site. As a result, the emission from acceptor fluorophores was used as a signature for protein-protein associations.²¹

2.3.4 HSA Surface Area Fraction

The fractional surface area of HSA was calculated at each concentration on each of the three surfaces. After injection of proteins into the flow cell, a given surface was incubated in the protein solution (containing very small fraction of labeled HSA) for 3 minutes, which was sufficient to allow the surface to reach equilibrium in the small volume of the flow cell. The laser and the camera were then turned on to capture images of the surface showing the number of adsorbed fluorescent molecules. The number of adsorbed unlabeled molecules was estimated by multiplying the number of fluorescent molecules by the ratio of unlabeled to labeled molecules. These measurements were performed quickly enough that the effects of photobleaching were observed to be negligible. To calculate the fractional surface area of HSA, the total area covered by HSA molecules (calculated using the estimated HSA cross-sectional area, $\sim 31.4 \text{ nm}^2$) was divided by the total area of the field of view. It is noteworthy that due to different types of affinities to surfaces, HSA may adopt specific orientations when adsorbed, leading to distinct cross-sectional areas (from $\sim 16.0 \text{ nm}^2$ to $\sim 51.6 \text{ nm}^2$).^{4, 49-51} The orientations of proteins on surfaces may also change with surface concentration, which is difficult to describe by a simple model.^{52, 53} To make a reasonable approximation of the cross-sectional area, we assumed that adsorbed HSA had a constant cross-sectional area on each surface, and we estimated this value using the diameter of albumin globule at pH 7.4 ($62 \pm 1 \text{ \AA}$).^{46, 54, 55} This value is similar to the cross-sectional area for the protein in its predominant native conformation as previously reported, which is 28.2 nm^2 .⁵⁴

2.3.5 Data Analysis

2.3.5.1 Super-resolution mapping – Super-resolution maps were achieved via a variation of the localization technique called “motion blur” point accumulation of imaging in nanoscale topography (mbPAINT)⁵⁶⁻⁵⁸ with a pixel size of 14.5 nm. Briefly, the position of each adsorbed molecule was placed on a pseudoimage and blurred by a Gaussian function. Only the first position of each adsorbed molecule was used for the adsorption maps, while all trajectory positions were included for the occupancy maps. By accumulating large numbers of trajectories, the distributions of adsorption sites were sampled in a statistically significant way.

2.3.5.2 Adsorption site analysis – By summing and grouping connected adsorption events, adsorption sites were identified. The adsorption event count for each site was defined as the maximum local value. The distribution of adsorption events was described using a Poisson mixture model²⁵

$$f_{ads}(n) = \sum_{i=1}^M p_i \frac{\lambda_i^n e^{-\lambda_i}}{n! (1 - e^{-\lambda_i})} \quad (\text{Eq. 2-1})$$

where λ_i is the average number of adsorption events and p_i is the corresponding fraction for the i th population. M is the total number of populations. Given the average number of adsorption events

$$\lambda = \sum_{i=1}^M p_i \lambda_i \quad (\text{Eq. 2-2})$$

the experimental number of surface adsorption sites could be expressed as N/λ , where N is the total number of trajectories.

2.3.5.3 *Surface heterogeneity* – The relative heterogeneity of a surface, represented by a surface heterogeneity index, was described as the maximum theoretical number of adsorption sites divided by the experimental number of adsorption sites²²

$$h = \frac{A/a}{N/\lambda} \quad (\text{Eq. 2-3})$$

where A is the total image surface area ($1892 \mu\text{m}^2$) and a is the cross-sectional area of an adsorbed HSA molecule ($\sim 31.4 \text{ nm}^2$).

2.3.5.4 *Cumulative residence time distributions (CRTD)* – Molecular residence times were determined by identifying the number of frames in which a given molecule appeared. Using these residence times, we calculated cumulative residence time distributions (CRTD),⁵⁹ where the cumulative probabilities represented the fraction of molecules remaining on the surface for time t or longer. Assuming multiple populations, the CRTD can be described by an exponential mixture model

$$C(t) = \sum_{i=1}^n f_i \exp(-t/\tau_i) \quad (\text{Eq. 2-4})$$

based on a model involving a superposition of first-order desorption processes. f_i and τ_i represented the fraction of each population and the corresponding characteristic residence time respectively. Thus the mean residence time can be calculated as

$$\tau = \sum_{i=1}^n f_i \tau_i \quad (\text{Eq. 2-5})$$

where n is the total number of populations.

2.4 RESULTS AND DISCUSSION

2.4.1 Surface Area Fraction

Interactions of molecules with surfaces are known to be strongly influenced by surface coverage.^{22, 60-63} In our experiments, with the protein concentration varying over many orders of magnitude, the surface area fraction of HSA (F_{HSA}) varied from ultra-low to fully saturated. Due to the dramatically different affinity of HSA with the four surfaces, we observed (as illustrated below) that comparisons based on solution concentration, while useful for practical applications, provided little physical insight, and we hypothesized that more universal behavior might be observed if protein surface coverage was used as the basis for comparison. In order to make this conversion, we measured surface coverage isotherms vs. solution concentration as described above (see **Figure 2-1**). We note that the highest concentration used was lower than the critical concentration reportedly resulting in HSA pre-nucleation clusters in solution.⁶⁴

As shown in **Figure 2-1**, due to differences in the interactions between HSA and the various surface chemistries, the HSA concentration required to achieve a specific fractional surface coverage varied over roughly four orders of magnitude.⁶⁵⁻⁶⁷ On the hydrophobic TMS surface, reflecting the strongest affinity with HSA (presumably due to strong hydrophobic interaction as well as the fact that water is weakly bound and easily displaced),⁶⁸ approximately 10^{-6} of the surface was covered by HSA at a concentration of 10^{-8} mg/mL, and the surface was approximately fully covered at 10^{-3} mg/mL. The positively charged hydrophilic NH_2 surface, possessing the opposite net charge to HSA in solution, required bulk concentrations of 10^{-7} mg/mL and 0.1 mg/mL to achieve the equivalent area fractions. The corresponding

concentrations for the FS surface were as high as 10^{-5} mg/mL and 1 mg/mL due to its extreme hydrophilicity and like net negative charge to HSA. OEG surfaces exhibited the weakest affinity to HSA, and the concentrations required to attain these specific area fractions were approximately 10^{-4} mg/mL and 10 mg/mL. The ability of OEG to resist protein adsorption was previously suggested to be caused by a combination of the tight binding of water molecules around OEG chains, the rapid mobility of hydrated chains, and possibly the complete absence of electrostatic attraction.^{33, 69} These isotherms were used to make approximate conversions between solution concentration and surface coverage, allowing us to test the hypothesis that surface coverage would comprise a more relevant basis for comparison between the three surfaces.

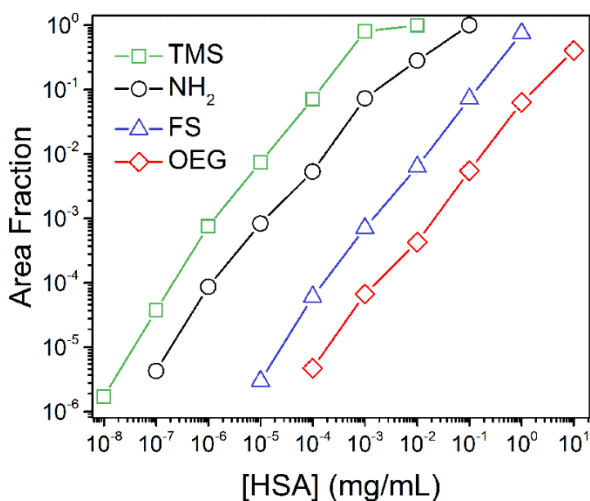


Figure 2-1. Adsorption isotherms vs. concentration of HSA on TMS, NH₂, FS and OEG surfaces.

2.4.2 Site Blocking on TMS, FS and OEG Surfaces

Here we combine the discussion of TMS, FS and OEG surfaces due to the fact that the phenomena observed were qualitatively similar. In different stages of the protein adsorption processes on the surfaces, adsorbed tracers were identified and the initial locations of these trajectories were collected and accumulated to generate super-resolution adsorption maps exhibiting individual binding sites. Due to the finite number of adsorption events and thus the very low tracer area fraction, sites with several adsorption counts were identified as anomalous and defined as strong binding sites.²⁵

Figure 2-2 shows adsorption maps of HSA on TMS, FS and OEG surfaces at three representative ranges of surface coverage. In experiments where the surface area fraction covered by HSA was extremely low, the adsorption on both TMS and FS surfaces was highly heterogeneous with many strong binding sites observed (**Figure 2-2a and 2-2d**). The adsorption on OEG surfaces was initially more homogeneous than on the other surfaces (presumably related to its resistance to protein adsorption), but still exhibited noticeable strong sites. Evidently, when a limited number of proteins were introduced to these surfaces, they preferentially adsorbed to these strong sites rather than weak sites even though the latter ones were much more abundant. One probable explanation for the existence of strong sites is that they are due to anomalous local chemical and/or physical properties which are favorable to protein adsorption. For example, the history of a fused silica sample determines the amount and arrangement of silanol and siloxane groups on its surface, which can further result in regions with different hydrophobicity.⁷⁰⁻⁷³ This

heterogeneity can potentially affect the quality of self-assembled monolayers (SAM) after surface modification.

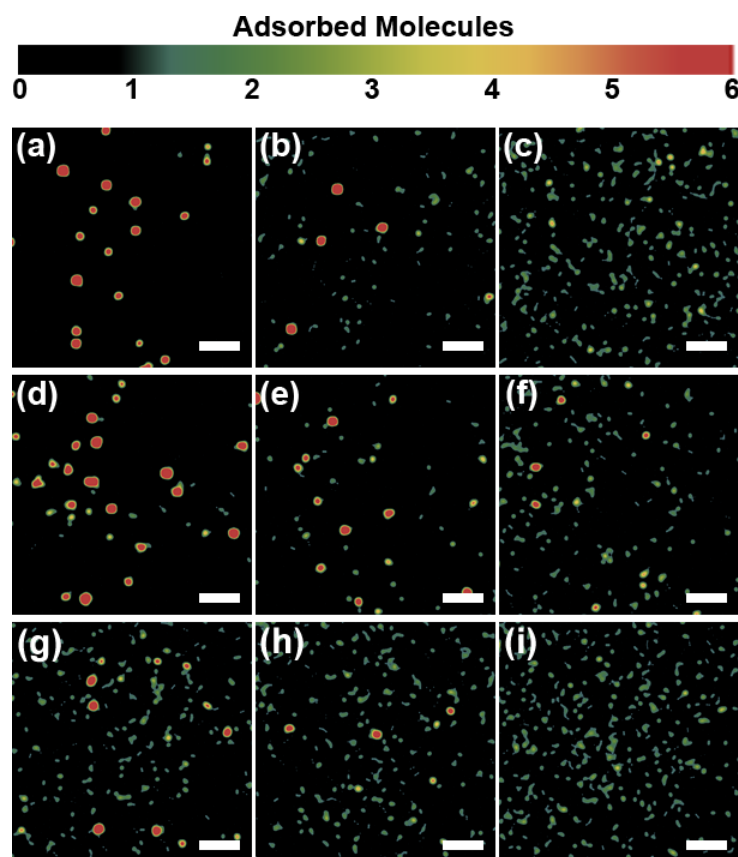


Figure 2-2. Representative super-resolution adsorption maps of HSA on (a-c) TMS, (d-f) FS and (g-i) OEG surfaces at very low HSA area fraction ($\sim 10^{-6}$, panels a, d and g), intermediate area fraction ($\sim 10^{-3}$, panels b, e and h) and high area fraction (~ 1 , panels c, f and i). Scale bar = 2 μm . The corresponding occupancy maps are shown in Appendix A.

As protein concentration (and surface coverage) increased, the heterogeneity developed in the same way on TMS, FS and OEG surfaces. For TMS surfaces, the density of anomalous strong binding sites decreased monotonically with surface coverage (**Figure 2-2b**), and were virtually nonexistent near saturated coverage (**Figure 2-2c**). Similarly, for FS surfaces, the number of strong binding sites decreased gradually, with only a small fraction of remaining at high surface coverage (**Figure 2-2f**). The anomalous adsorption on OEG surfaces also showed an obvious decrease, and at high surface coverage the adsorption was truly homogeneous (**Figure 2-2i**). It is reasonable to assume that with increased protein concentrations or surface area fraction, strong sites were increasingly occupied, or blocked, by adsorbed unlabeled proteins. Therefore, further adsorption to these sites was hindered, and these strong sites became weak.

To quantify these trends, probability histograms of site adsorption event counts, as shown in **Figure 2-3**, were constructed based on the adsorption maps. If a surface were ideally homogeneous, the site adsorption events distribution should follow Poisson statistics since the probability of adsorbing on each site would be identical. Since the actual surfaces were heterogeneous, a Poisson mixture model, with multiple populations representing different types of adsorption sites, was used to fit the heavy-tailed distributions (Eq. 2-1). For each case, two classes of adsorption sites were observed depending on the mean number of adsorption events (λ): populations with very small λ values (0.1-0.3) represented weak sites, while populations with much higher λ values (>2) represented strong sites. Consistent with the mapping results, the fractions of strong sites, as well as the corresponding mean numbers of adsorption events, decreased dramatically on all three surfaces as a function of surface coverage. As shown in **Table A-1** in Appendix A, as the HSA surface area fraction increased from $\sim 10^{-6}$ to 1, the fraction of strong sites decreased from 0.20 to 0.02 on TMS surface, while the characteristic

number of adsorption events on strong sites decreased from ~ 9 to ~ 3 . Correspondingly, on FS surfaces, the fraction of strong sites decreased from 0.18 to 0.08 with the number of adsorption events falling from ~ 12 to ~ 6 . On the most homogeneous OEG surfaces, the fraction of strong sites also showed an apparent decrease from 0.08 to 0.02 and the characteristic number of adsorption events decreased from ~ 6 to ~ 4 .

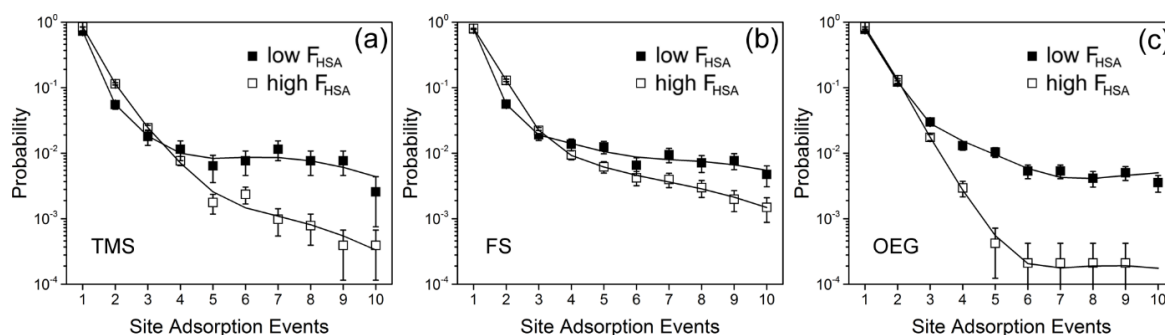


Figure 2-3. The probability distributions of HSA site adsorption events on (a) TMS, (b) FS and (c) OEG surfaces at low area fraction ($\sim 10^{-6}$) and high area fraction (~ 1), respectively. Poisson mixture fits are represented by solid lines.

To further quantify the surface heterogeneity, the relative surface heterogeneity index h was calculated in each case using Eq. 2-3. Higher heterogeneity index values indicate more heterogeneous surfaces. **Figure 2-4** shows the evolution of the surface heterogeneity of TMS, FS and OEG surfaces with increased solution concentrations and HSA area fraction. When expressed in terms of solution concentration, the progression of heterogeneity on the three surfaces varied dramatically. In particular, the increase of site blocking on TMS surfaces mainly occurred within a concentration range from 10^{-8} mg/mL to 10^{-6} mg/mL (**Figure 2-4a**), following which the heterogeneity parameters saturated. In contrast, site blocking on FS surfaces occurred

over a much higher concentration range from 10^{-5} mg/mL to 10^{-2} mg/mL (**Figure 2-4a**), and the corresponding concentration range was even higher on OEG surfaces, from 10^{-4} mg/mL to 0.1 mg/mL (**Figure 2-4a**), due to the weak affinity of HSA to these surfaces. However, in terms of area fraction, the transitions of three surfaces were very similar. On all surfaces, the heterogeneity parameter showed a marked decrease when the HSA surface area fraction increased from 10^{-5} to 10^{-3} (**Figure 2-4b**), after which the decrease slowed down at higher area

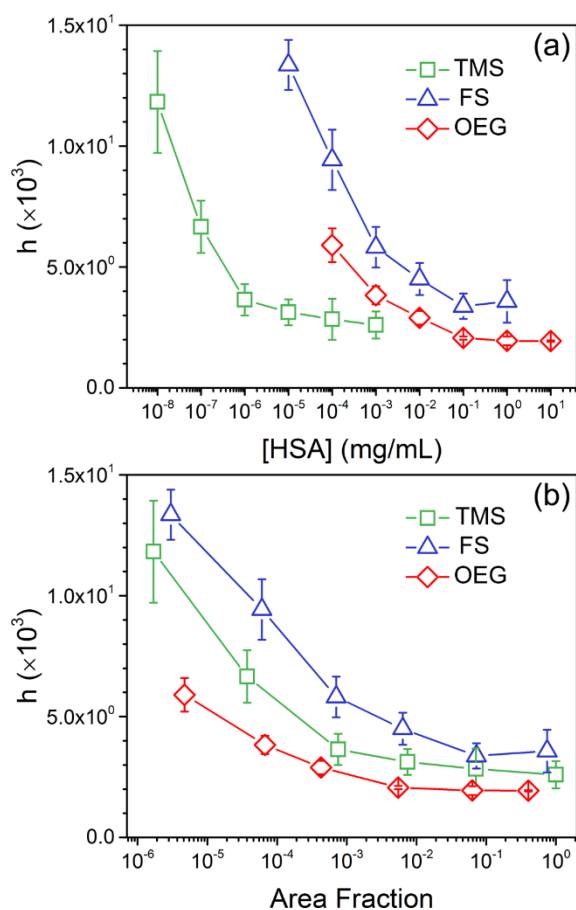


Figure 2-4. The relative surface heterogeneity parameter (h) versus (a) HSA concentration and (b) HSA area fraction on TMS, FS and OEG surfaces.

fractions. Based on these observations, it is reasonable to conclude that the protein surface area fraction, instead of the solution concentration, is the more relevant factor to determine site blocking efficacy and solution concentration alone should not be considered as an appropriate parameter. This observation is potentially associated with the history-dependent protein adsorption model, suggesting that independent of the adsorption rate and surface heterogeneity, the history of the protein layer (reflected by protein area fraction) is a critical factor in determining further adsorption.⁶³

Interestingly, the strong sites that were identified by excessive adsorption events also exhibited anomalously long retention of HSA molecules. **Figure 2-5a** shows representative cumulative residence time distributions of HSA molecules, on strong and weak adsorption sites, for TMS, FS and OEG surfaces, respectively. The slower decay of the distributions associated with strong sites indicates that they retained molecules for longer times compared to weak sites, presumably because of stronger protein-surface interactions. This was particularly dramatic for TMS, but also significant for FS and OEG. This also resulted in a distinct trend in the mean surface residence times as a function of HSA surface coverage, as shown in **Figure 2-5b**. On all three surfaces, HSA exhibited systematically shorter surface residence times at high coverage as a result of decreased amount of strong sites. These trends, consistent with the evolution of surface heterogeneity with protein coverage, again suggested the high retention capacity of molecules to strong sites, which has potential connections to surface fouling behavior, since longer HSA on strong sites may result in a higher probability to undergo conformational changes and/or interact with other proteins.⁷⁴

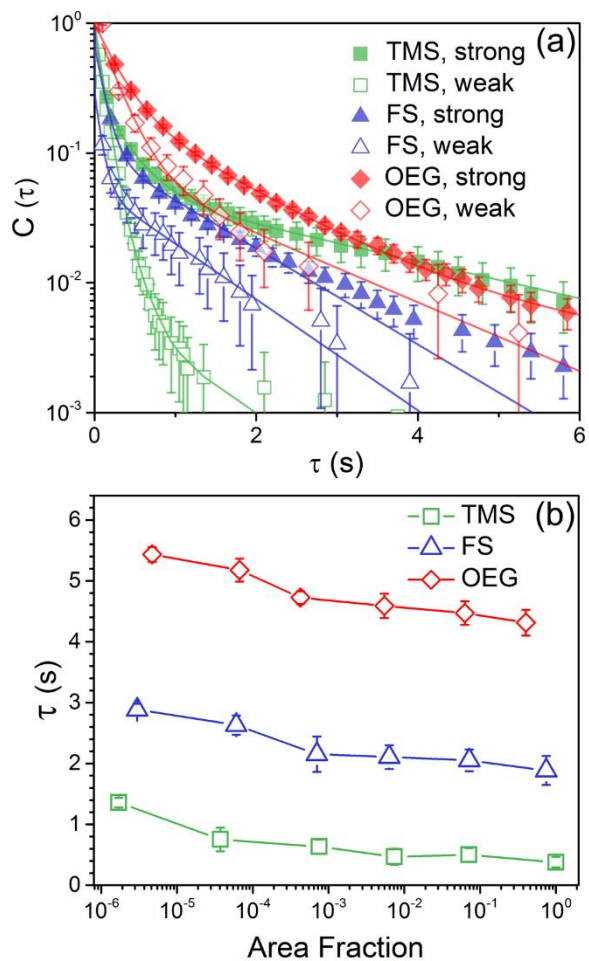


Figure 2-5. (a) Representative cumulative residence time distributions of HSA on strong sites (closed labels) and weak sites (open labels) on TMS (green), FS (purple) and OEG (red) surfaces, respectively. Multiple exponential fits are indicated by solid lines. (b) Mean residence times of HSA on TMS, FS and OEG surfaces.

2.4.3 Anomalous Site Blocking on NH₂ Surfaces

In contrast with TMS, FS and OEG, NH₂ surfaces exhibited heterogeneity that was non-monotonic as a function of protein concentration. As shown in **Figure 2-6**, abundant strong sites existed on NH₂ surface at very low concentrations (**Figure 2-6a**) and were blocked, as for TMS and FS, by feeding in more protein (**Figure 2-6b**). Surprisingly, a further increase of concentration (still at very low HSA area fraction), led to the appearance of new “strong sites” (**Figures 2-6c and 2-6d**). By comparing **Figure 2-6a** and **Figure 2-6c**, which visually captured the spatial heterogeneity on the same area, we determined that the new “strong sites” arose in different locations compared to the original ones. Since the original strong sites had been blocked by adsorbed proteins, the new “strong sites” were presumably due to a different mechanism.

Representative probability distributions of site adsorption events as a function of HSA area fraction on NH₂ surfaces are shown in **Figure 2-6d**, exhibiting the reduction and re-creation of anomalous sites. The fraction of strong sites (determined using Poisson mixture model fitting), which was 0.14 at the lowest area fraction, decreased strikingly to less than 0.01 when the area fraction reached 10^{-4} . The corresponding characteristic adsorption number on the strong sites also decreased from ~15 to ~4. However, at an increased area fraction of 10^{-3} , the fraction of strong sites rose again to 0.19, together with the characteristic adsorption events on strong sites. These two parameters then remained high for further increases in surface coverage. Analogously, the heterogeneity of NH₂ surfaces exhibited a minimum at low area fraction and then increased sharply. We hypothesized that this anomalous increase of heterogeneity with increasing protein coverage, illustrating the complexity of the site blocking process, was possibly related to lateral

interactions, or protein-protein associations that occurred more frequently as the surface became more crowded.⁴ Specifically, we hypothesized that the new “strong sites” on the NH₂ surface were no longer directly determined by special surface chemistry or surface structure, but may have been associated with protein clusters induced by strong protein-protein associations.²⁰⁻²² As a result, proteins approaching the surface would have higher affinity to these “sites” rather than to the uncovered surface (on which many strong sites had already been blocked).

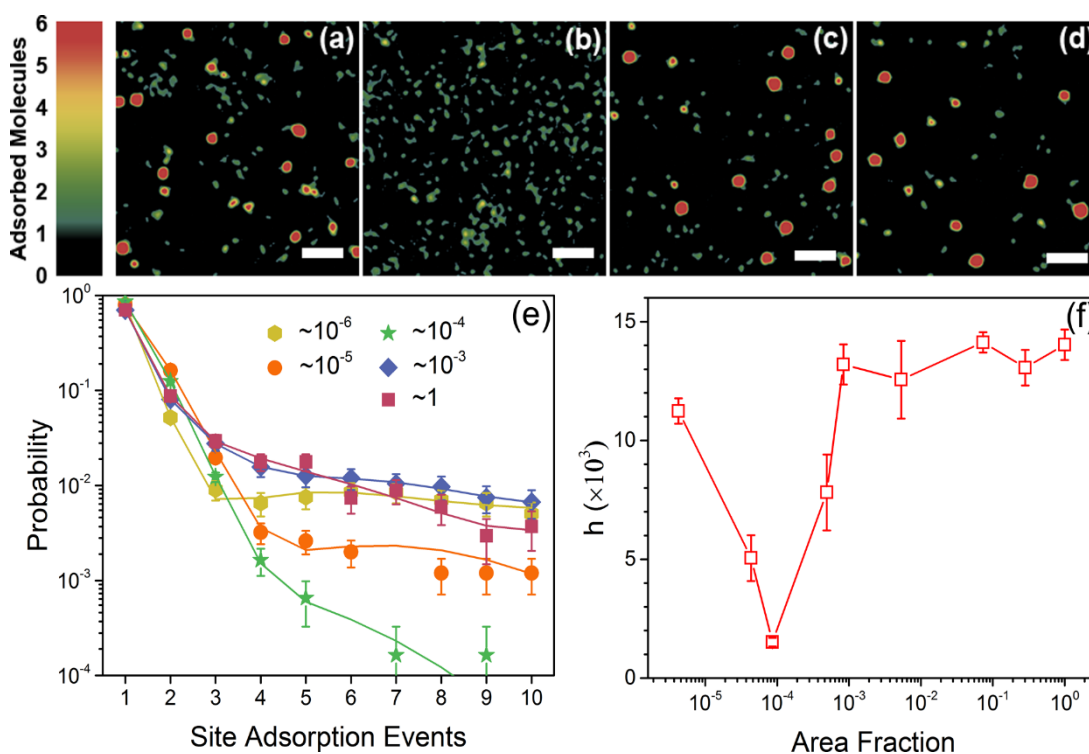


Figure 2-6. Representative super-resolution maps of HSA on NH₂ surface at HSA surface area fractions of (a) $\sim 10^{-6}$, (b) $\sim 10^{-4}$, (c) $\sim 10^{-3}$ and (d) ~ 1 . Scale bar = 2 μm . (e) The probability distributions of site adsorption events of HSA on NH₂ surfaces at various HSA area fractions. Poisson mixture fits are indicated by solid lines. (f) Relative surface heterogeneity parameters of NH₂ surfaces using HSA as probes as a function of HSA surface area fraction.

Intermolecular FRET was used to test our hypothesis that the anomalous rise of new “strong sites” on NH_2 surfaces was caused by protein aggregation. As described in the experimental section, HSA molecules labeled with different fluorophores were used as donors and acceptors respectively. An ultra low concentration of donor-labeled molecules was employed (10^{-7} mg/mL, $\sim 10^{-5}$ area fraction), and the concentration of acceptor-labeled molecules was 1-2 orders of magnitude greater than the donor concentration, ensuring sufficient interactions between donors and acceptors. These associations were clearly characterized by comparing the signals in the two channels: only donor emission was observed in the absence of protein-protein associations, and emission in the acceptor channel was a signature of associations.

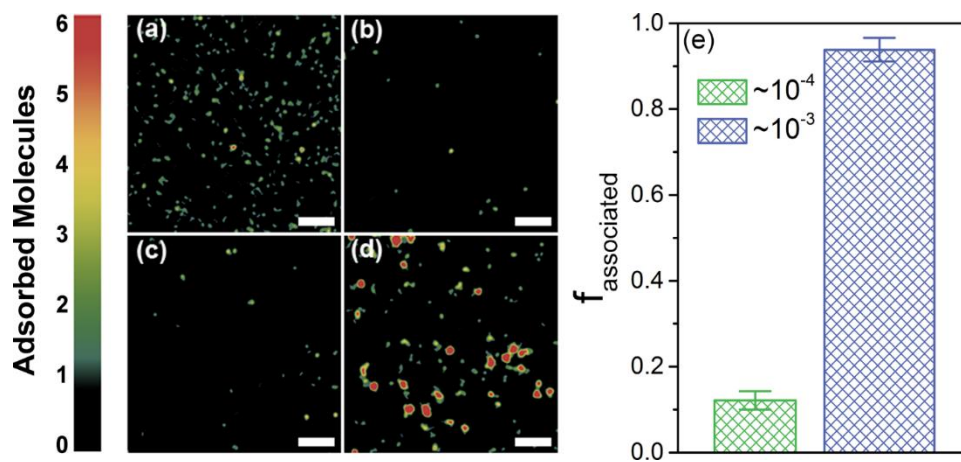


Figure 2-7. Super-resolution maps of donor-labeled HSA molecules adsorbing to (a) bare NH_2 surface sites, or (b) sites pre-occupied by acceptor-labeled molecules at an HSA area fraction of 10^{-4} ; and similarly, donor-labeled HSA molecules adsorbing to (c) bare NH_2 surface sites or (d) sites pre-occupied by acceptor-labeled molecules at an HSA area fraction of 10^{-3} . Scale bar = 2 μm . (e) The fraction of associated molecules upon adsorption at area fractions of 10^{-4} (green) and 10^{-3} (violet), respectively.

Two-channel super-resolution adsorption maps (**Figures 2-7 a–d**) were generated to visualize the impact of protein-protein associations at different levels of the surface coverage. If a donor-labeled molecule adsorbed directly to the bare surface, the location of the adsorption site was indicated in the donor channel map (**Figures 2-7a and 2-7c**). Otherwise, if a donor-labeled protein adsorbed on a site already occupied by one or more acceptor-labeled molecules, the location was indicated in the acceptor channel maps (**Figures 2-7b and 2-7d**). Experiments were carried out at surface area fractions of 10^{-4} and 10^{-3} , associated with the minimum and the subsequent increase of surface heterogeneity. With 10^{-4} of the surface covered by HSA, the surface was largely homogeneous (without the appearance of “hot spots”) with fluorescent molecules mainly identified in the donor channel (**Figure 2-7a**) and very few appearing in the acceptor channel (**Figure 2-7b**), suggesting that most proteins adsorbed directly to the bare surface and protein-protein associations were negligible. In contrast, with the surface area fraction increased to 10^{-3} , the majority of donor molecules adsorbed to sites that were already occupied, resulting in acceptor emission, indicating the importance of protein-protein associations during the adsorption process. Thus, the acceptor map (**Figure 2-7d**) illustrates many more adsorption events than the donor map (**Figure 2-7c**). In particular, strong adsorption sites only appeared in the acceptor map, emphasizing the crucial importance of pre-adsorbed proteins on the formation of new “strong sites”. To further quantify these results, we calculated the percentage of molecules that exhibited protein-protein association upon adsorption, i.e. molecules that adsorbed to sites that were apparently pre-occupied by protein clusters (**Figure 2-7e**). At the lower area fraction, only 10% of the molecules adsorbed to protein-occupied sites, while at the higher area fraction, over 90% of them adsorbed to such sites.

These results suggest that instead of forming a homogeneous layer, as they apparently did on TMS, FS and OEG, HSA proteins on NH₂ surfaces aggregated into heterogeneous clusters at a relatively low surface area fraction. Thus, the aggregation of proteins was indirectly dependent on surface-protein interactions, with the NH₂ surface chemistry causing increased protein-protein associations. We speculate that proteins may potentially undergo conformational and/or orientational changes in contact with the NH₂ surface functionality,^{44, 74-78} potentially exposing highly interactive regions, resulting the “cooperative adsorption” of vicinal proteins.⁷⁹⁻⁸⁴ Evidently, increasing the average surface coverage did not attenuate the “cooperative effect” or “cover” the protein clusters since the surface heterogeneity did not decrease even in the presence of much higher protein concentration.

As shown above in **Figure 2-5**, strong adsorption sites on TMS, FS and OEG surfaces retained molecules longer than weak sites; a similar phenomenon was also observed on NH₂ surfaces at low surface coverage (**Figure 2-8a**). Additionally, at high surface area fraction, molecules exhibited longer residence times on the protein clusters compared to the bare surface. This is related to previous observations by Langdon et al. that protein oligomers remained on a surface longer than protein monomers,²² and that monomers undergoing one or more intermolecular associations resided on a surface longer than monomers that did not associate.²¹ As a result, the mean residence times as a function of HSA coverage on NH₂ surfaces (**Figure 2-8b**) first dropped to a minimum value due to site blocking, then increased and remained high, consistent with the sustained presence of apparent protein clusters. Interestingly, these findings suggest that site blocking using HSA on NH₂ surfaces exhibits a “Goldilocks” principle, where the use of excessive HSA blocking agent may result in the unfortunate creation of additional strong binding sites.

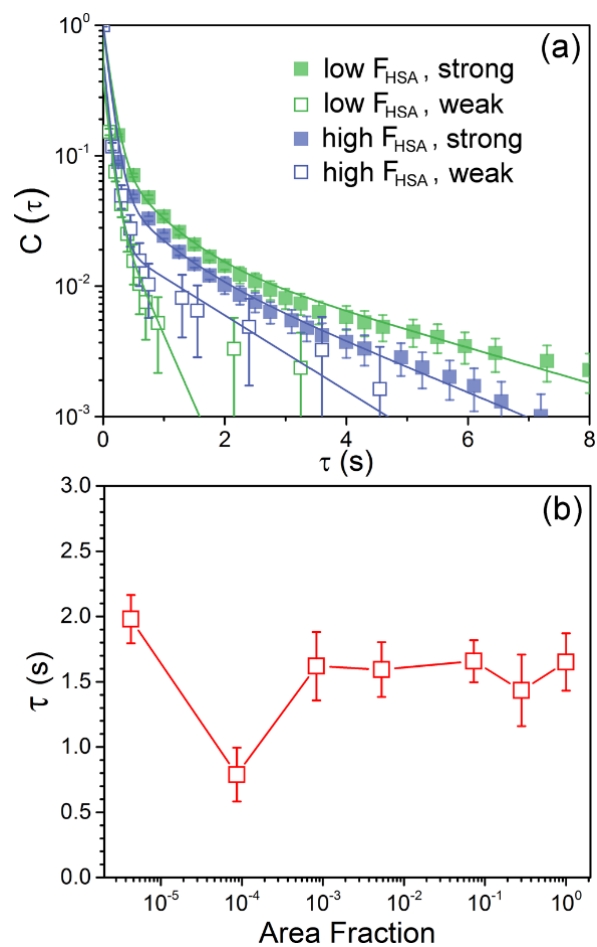


Figure 2-8. (a) Representative cumulative residence time distributions of HSA on strong sites (closed squares) and weak sites (open squares) at low area fraction (green) and high area fraction (violet), respectively. Solid lines represent multiple exponential fits. (b) Mean residence times of HSA on NH₂ surface.

2.5 CONCLUSIONS

The effects of surface coverage on the dynamics of HSA on four model surfaces was investigated using single-molecule tracking. On TMS, FS and OEG surfaces, adsorption became more spatially homogeneous and proteins were more transient with increased coverage by HSA. These phenomena were presumably due to the blocking of strong binding sites, which led to excessive adsorption and long retention times due to their anomalous chemical and/or topographical features. The blocking processes were found to be closely associated with fractional surface coverage as opposed to solution concentration. Contrarily, site blocking on NH_2 surfaces showed a Goldilocks principle with surface heterogeneity and residence times first decreasing and then increasing at high surface area fraction. This unexpected phenomenon was caused by strong protein-protein associations, which potentially resulted in cooperative adsorption.

These results suggest that distinct surface chemistries potentially result in dramatically different adsorption rates, surface-protein associations, protein-protein associations, and ultimately lead to diverse dynamic behavior of adsorbed protein molecules. While the use of a blocking agent can be a powerful way to reduce non-specific adsorption, our results suggest that the improper use of a blocking agent can actually exacerbate undesirable effects due to the creation of new strong binding sites associated with intermolecular protein interactions. Therefore, the choice and amount of blocking agent must be carefully considered and tested on a case-by-case basis.

2.6 REFERENCES

1. Wang, S.; Yong, W.; Liu, J.; Zhang, L.; Chen, Q.; Dong, Y., Development of an indirect competitive assay-based aptasensor for highly sensitive detection of tetracycline residue in honey. *Biosens. Bioelectron.* **2014**, *57*, 192-8.
2. Shiddiky, M. J.; Kithva, P. H.; Kozak, D.; Trau, M., An electrochemical immunosensor to minimize the nonspecific adsorption and to improve sensitivity of protein assays in human serum. *Biosens. Bioelectron.* **2012**, *38* (1), 132-7.
3. Hideshima, S.; Sato, R.; Inoue, S.; Kuroiwa, S.; Osaka, T., Detection of tumor marker in blood serum using antibody-modified field effect transistor with optimized BSA blocking. *Sens. Actuators, B* **2012**, *161* (1), 146-150.
4. Rabe, M.; Verdes, D.; Seeger, S., Understanding protein adsorption phenomena at solid surfaces. *Adv. Colloid Interface Sci.* **2011**, *162* (1-2), 87-106.
5. Yang, D.; Lu, X.; Hong, Y.; Xi, T.; Zhang, D., The molecular mechanism of mediation of adsorbed serum proteins to endothelial cells adhesion and growth on biomaterials. *Biomaterials* **2013**, *34* (23), 5747-58.
6. Li, L.; Qian, Y.; Jiang, C.; Lv, Y.; Liu, W.; Zhong, L.; Cai, K.; Li, S.; Yang, L., The use of hyaluronan to regulate protein adsorption and cell infiltration in nanofibrous scaffolds. *Biomaterials* **2012**, *33* (12), 3428-45.
7. Wang, L.; Cai, Y.; Jing, Y.; Zhu, B.; Zhu, L.; Xu, Y., Route to hemocompatible polyethersulfone membranes via surface aminolysis and heparinization. *J. Colloid Interface Sci.* **2014**, *422*, 38-44.
8. Saxena, A.; Tripathi, B. P.; Kumar, M.; Shahi, V. K., Membrane-based techniques for the separation and purification of proteins: an overview. *Adv. Colloid Interface Sci.* **2009**, *145* (1-2), 1-22.
9. Bhambure, R.; Sharma, I.; Pattanayek, S. K.; Rathore, A. S., Qualitative and quantitative examination of non-specific protein adsorption on filter membrane disks of a commercially available high throughput chromatography device. *J. Membr. Sci.* **2014**, *451*, 312-318.

10. Kang, S. H.; Yeung, E. S., Dynamics of Single-Protein Molecules at a Liquid/Solid Interface: Implications in Capillary Electrophoresis and Chromatography. *Anal. Chem.* **2002**, *74* (24), 6334-6339.
11. Nakanishi, K.; Sakiyama, T.; Imamura, K., On the adsorption of proteins on solid surfaces, a common but very complicated phenomenon. *J. Biosci. Bioeng.* **2001**, *91* (3), 233-244.
12. Ljunglof, A.; Hjorth, R., Confocal microscopy as a tool for studying protein adsorption to chromatographic matrices. *J. Chromatogr. A* **1996**, *743*, 75-83.
13. Sun, S.; Yue, Y.; Huang, X.; Meng, D., Protein adsorption on blood-contact membranes. *J. Membr. Sci.* **2003**, *222* (1-2), 3-18.
14. Belanger, M.-C.; Marois, Y., Hemocompatibility, Biocompatibility, Inflammatory and in Vivo Studies of Primary Reference Materials Low-Density Polyethylene and Polydimethylsiloxane: A Review. *J. Biomed. Mater. Res.* **2001**, *58* (5), 467-477.
15. Allen, L. T.; Tosetto, M.; Miller, I. S.; O'Connor, D. P.; Penney, S. C.; Lynch, I.; Keenan, A. K.; Pennington, S. R.; Dawson, K. A.; Gallagher, W. M., Surface-induced changes in protein adsorption and implications for cellular phenotypic responses to surface interaction. *Biomaterials* **2006**, *27* (16), 3096-108.
16. Hsieh, H. Y.; Wang, P. C.; Wu, C. L.; Huang, C. W.; Chieng, C. C.; Tseng, F. G., Effective enhancement of fluorescence detection efficiency in protein microarray assays: application of a highly fluorinated organosilane as the blocking agent on the background surface by a facile vapor-phase deposition process. *Anal. Chem.* **2009**, *81* (19), 7908-16.
17. Xiao, Y.; Isaacs, S. N., Enzyme-linked immunosorbent assay (ELISA) and blocking with bovine serum albumin (BSA)--not all BSAs are alike. *J. Immunol. Methods* **2012**, *384* (1-2), 148-51.
18. Miller-Jaster, K. N.; Petrie Aronin, C. E.; Guilford, W. H., A Quantitative Comparison of Blocking Agents in the In Vitro Motility Assay. *Cell. Mol. Bioeng.* **2011**, *5* (1), 44-51.
19. Zhang, B.; Wang, X.; Liu, F.; Cheng, Y.; Shi, D., Effective reduction of nonspecific binding by surface engineering of quantum dots with bovine serum albumin for cell-targeted imaging. *Langmuir* **2012**, *28* (48), 16605-13.

20. Langdon, B. B.; Kastantin, M.; Schwartz, D. K., Surface Chemistry Influences Interfacial Fibrinogen Self-Association. *Biomacromolecules* **2015**, *16*, 3201-3208.
21. Langdon, B. B.; Kastantin, M.; Walder, R.; Schwartz, D. K., Interfacial protein-protein associations. *Biomacromolecules* **2014**, *15* (1), 66-74.
22. Langdon, B. B.; Mirhossaini, R. B.; Mabry, J. N.; Sriram, I.; Lajmi, A.; Zhang, Y.; Rojas, O. J.; Schwartz, D. K., Single-molecule resolution of protein dynamics on polymeric membrane surfaces: the roles of spatial and population heterogeneity. *ACS Appl. Mater. Interfaces* **2015**, *7* (6), 3607-17.
23. Sengupta, P.; Jovanovic-Talisman, T.; Skoko, D.; Renz, M.; Veatch, S. L.; Lippincott-Schwartz, J., Probing protein heterogeneity in the plasma membrane using PALM and pair correlation analysis. *Nat. Methods* **2011**, *8* (11), 969-75.
24. Gritti, F.; Guiochon, G., Heterogeneity of the adsorption mechanism of low molecular weight compounds in reversed-phase liquid chromatography. *Anal. Chem.* **2006**, *78* (16), 5823-34.
25. Mabry, J. N.; Skaug, M. J.; Schwartz, D. K., Single-molecule insights into retention at a reversed-phase chromatographic interface. *Anal. Chem.* **2014**, *86* (19), 9451-8.
26. Rimola, A.; Costa, D.; Sodupe, M.; Lambert, J. F.; Ugliengo, P., Silica surface features and their role in the adsorption of biomolecules: computational modeling and experiments. *Chem. Rev.* **2013**, *113* (6), 4216-313.
27. Puddu, V.; Perry, C. C., Peptide Adsorption on Silica Nanoparticles: Evidence of Hydrophobic Interactions. *ACS Nano* **2012**, *6* (7), 6356-6363.
28. San Paulo, A.; García, R., Tip-surface forces, amplitude, and energy dissipation in amplitude-modulation (tapping mode) force microscopy. *Phys. Rev. B* **2001**, *64* (19), 193411.
29. Möller, C.; Allen, M.; Elings, V.; Engel, A.; Müller, D. J., Tapping-mode atomic force microscopy produces faithful high-resolution images of protein surfaces. *Biophys. J.* **1999**, *77* (2), 1150-1158.
30. Wang, M. S.; Palmer, L. B.; Schwartz, J. D.; Razatos, A., Evaluating protein attraction and adhesion to biomaterials with the atomic force microscope. *Langmuir* **2004**, *20* (18), 7753-7759.

31. Kidoaki, S.; Matsuda, T., Adhesion forces of the blood plasma proteins on self-assembled monolayer surfaces of alkanethiolates with different functional groups measured by an atomic force microscope. *Langmuir* **1999**, *15* (22), 7639-7646.
32. Walder, R.; Nelson, N.; Schwartz, D. K., Super-resolution surface mapping using the trajectories of molecular probes. *Nat. Commun.* **2011**, *2*, 515.
33. Ma, H.; Hyun, J.; Stiller, P.; Chilkoti, A., “Non-Fouling” Oligo (ethylene glycol)-Functionalized Polymer Brushes Synthesized by Surface-Initiated Atom Transfer Radical Polymerization. *Adv. Mater.* **2004**, *16* (4), 338-341.
34. Asenath Smith, E.; Chen, W., How to prevent the loss of surface functionality derived from aminosilanes. *Langmuir* **2008**, *24* (21), 12405-12409.
35. Tsukruk, V. V.; Bliznyuk, V. N., Adhesive and friction forces between chemically modified silicon and silicon nitride surfaces. *Langmuir* **1998**, *14* (2), 446-455.
36. Monserud, J. H.; Schwartz, D. K., Effects of molecular size and surface hydrophobicity on oligonucleotide interfacial dynamics. *Biomacromolecules* **2012**, *13* (12), 4002-4011.
37. Bavari, S.; Bosio, C. M.; Wiegand, E.; Ruthel, G.; Will, A. B.; Geisbert, T. W.; Hevey, M.; Schmaljohn, C.; Schmaljohn, A.; Aman, M. J., Lipid Raft Microdomains A Gateway for Compartmentalized Trafficking of Ebola and Marburg Viruses. *J. Exp. Med.* **2002**, *195* (5), 593-602.
38. Wang, D.; Hu, R.; Mabry, J. N.; Miao, B.; Wu, D. T.; Koynov, K.; Schwartz, D. K., Scaling of Polymer Dynamics at an Oil-Water Interface in Regimes Dominated by Viscous Drag and Desorption-Mediated Flights. *J. Am. Chem. Soc.* **2015**, *137*, 12312-12320.
39. Honciuc, A.; Harant, A. W.; Schwartz, D. K., Single-molecule observations of surfactant diffusion at the solution-solid interface. *Langmuir* **2008**, *24*, 6562-6566.
40. Wang, D.; He, C.; Stoykovich, M. P.; Schwartz, D. K., Nanoscale Topography Influences Polymer Surface Diffusion. *ACS Nano* **2015**, *9* (2), 1656-1664.
41. Kastantin, M.; Schwartz, D. K., Connecting Rare DNA Conformations and Surface Dynamics Using Single-Molecule Resonance Energy Transfer. *ACS Nano* **2011**, *5* (12), 9861-9869.

42. Jager, M.; Nir, E.; Weiss, S., Site-specific labeling of proteins for single-molecule FRET by combining chemical and enzymatic modification. *Protein Sci.* **2006**, *15* (3), 640-6.
43. Lu, M.; Chai, J.; Fu, D., Structural basis for autoregulation of the zinc transporter YiiP. *Nat. Struct. Mol. Biol.* **2009**, *16* (10), 1063-7.
44. Majumdar, D. S.; Smirnova, I.; Kasho, V.; Nir, E.; Kong, X.; Weiss, S.; Kaback, H. R., Single-molecule FRET reveals sugar-induced conformational dynamics in LacY. *Proc. Natl. Acad. Sci. U. S. A.* **2007**, *104* (31), 12640-5.
45. Modi, S.; M, G. S.; Goswami, D.; Gupta, G. D.; Mayor, S.; Krishnan, Y., A DNA nanomachine that maps spatial and temporal pH changes inside living cells. *Nat. Nanotechnol.* **2009**, *4* (5), 325-30.
46. Kiselev, M. A.; Gryzunov, I. A.; Dobretsov, G. E.; Komarova, M. N., Size of Human Serum Albumin in Solution. *Biofizika* **2000**, *46*, 423-427.
47. Wang, J. S.; Brown, G. J.; Hung, W. C.; Wai, C. M., Supercritical fluid deposition of uniform PbS nanoparticle films for energy-transfer studies. *Chemphyschem* **2012**, *13* (8), 2068-73.
48. Thakur, G.; Jiang, K.; Lee, D.; Prashanthi, K.; Kim, S.; Thundat, T., Investigation of pH-induced protein conformation changes by nanomechanical deflection. *Langmuir* **2014**, *30* (8), 2109-16.
49. Kurrat, R.; Prenosil, J.; Ramsden, J., Kinetics of human and bovine serum albumin adsorption at silica–titania surfaces. *J. Colloid Interface Sci.* **1997**, *185* (1), 1-8.
50. Bloomfield, V., The Structure of Bovine Serum Albumin at Low pH*. *Biochemistry* **1966**, *5* (2), 684-689.
51. Oliva, F. Y.; Avalle, L. B.; Cámara, O. R.; De Pauli, C. P., Adsorption of human serum albumin (HSA) onto colloidal TiO₂ particles, Part I. *J. Colloid Interface Sci.* **2003**, *261* (2), 299-311.
52. McClellan, S. J.; Franses, E. I., Effect of concentration and denaturation on adsorption and surface tension of bovine serum albumin. *Colloids Surf., B* **2003**, *28* (1), 63-75.

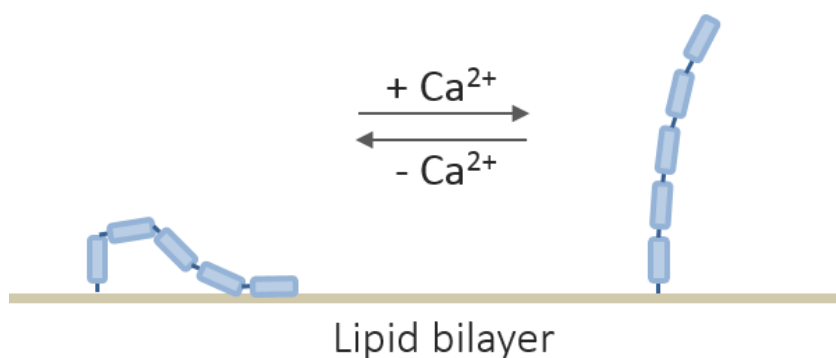
53. Kim, J.; Somorjai, G. A., Molecular packing of lysozyme, fibrinogen, and bovine serum albumin on hydrophilic and hydrophobic surfaces studied by infrared-visible sum frequency generation and fluorescence microscopy. *J. Am. Chem. Soc.* **2003**, *125* (10), 3150-3158.
54. Carter, D. C.; Ho, J. X., Structure of serum albumin. *Adv. Protein Chem.* **1994**, *45* (45), 153-203.
55. Luik, A.; Naboka, Y. N.; Mogilevich, S.; Hushcha, T.; Mischenko, N., Study of human serum albumin structure by dynamic light scattering: two types of reactions under different pH and interaction with physiologically active compounds. *Spectrochim. Acta Mol. Biomol. Spectrosc.* **1998**, *54* (10), 1503-1507.
56. Kisley, L.; Chen, J.; Mansur, A. P.; Shuang, B.; Kourentzi, K.; Poongavanam, M. V.; Chen, W. H.; Dhamane, S.; Willson, R. C.; Landes, C. F., Unified superresolution experiments and stochastic theory provide mechanistic insight into protein ion-exchange adsorptive separations. *Proc. Natl. Acad. Sci. U. S. A.* **2014**, *111* (6), 2075-80.
57. Kisley, L.; Chen, J.; Mansur, A. P.; Dominguez-Medina, S.; Kulla, E.; Kang, M. K.; Shuang, B.; Kourentzi, K.; Poongavanam, M. V.; Dhamane, S.; Willson, R. C.; Landes, C. F., High ionic strength narrows the population of sites participating in protein ion-exchange adsorption: a single-molecule study. *J. Chromatogr. A* **2014**, *1343*, 135-42.
58. Tauzin, L. J.; Shuang, B.; Kisley, L.; Mansur, A. P.; Chen, J.; de Leon, A.; Advincula, R. C.; Landes, C. F., Charge-dependent transport switching of single molecular ions in a weak polyelectrolyte multilayer. *Langmuir* **2014**, *30* (28), 8391-9.
59. Kastantin, M.; Schwartz, D. K., Identifying multiple populations from single-molecule lifetime distributions. *Chemphyschem* **2013**, *14* (2), 374-80.
60. Zhao, J.; Granick, S., Polymer Lateral Diffusion at the Solid-Liquid Interface. *J. Am. Chem. Soc.* **2004**, *126*, 6242-6243.
61. Zhao, J.; Granick, S., How polymer surface diffusion depends on surface coverage. *Macromolecules* **2007**, *40*, 1243-1247.
62. Herrera, E.; Giacomelli, C. E., Surface coverage dictates the surface bio-activity of D-amino acid oxidase. *Colloids Surf., B* **2014**, *117*, 296-302.
63. Tie, Y.; Calonder, C.; Van Tassel, P. R., Protein adsorption: kinetics and history dependence. *J. Colloid Interface Sci.* **2003**, *268* (1), 1-11.

64. Stradner, A.; Sedgwick, H.; Cardinaux, F.; Poon, W. C. K.; Egelhaaf, S. U.; Schurtenberger, P., Equilibrium cluster formation in concentrated protein solutions and colloids. *Nature* **2004**, *432*, 492-495.
65. Krisdhasima, V.; McGuire, J.; Sproull, R., Surface hydrophobic influences on β -lactoglobulin adsorption kinetics. *J. Colloid Interface Sci.* **1992**, *154* (2), 337-350.
66. Podhileux, N.; Krisdhasima, V.; McGuire, J., Molecular charge effects on protein behavior at hydrophobic and hydrophilic solid surfaces. *Food hydrocolloids* **1996**, *10* (3), 285-293.
67. Luey, J.-K.; McGuire, J.; Sproull, R. D., The effect of pH and NaCl concentration on adsorption of β -lactoglobulin at hydrophilic and hydrophobic silicon surfaces. *J. Colloid Interface Sci.* **1991**, *143* (2), 489-500.
68. McUmber, A. C.; Randolph, T. W.; Schwartz, D. K., Electrostatic Interactions Influence Protein Adsorption (but Not Desorption) at the Silica-Aqueous Interface. *J. Phys. Chem. Lett.* **2015**, *6* (13), 2583-7.
69. Zheng, J.; Li, L.; Chen, S.; Jiang, S., Molecular simulation study of water interactions with oligo (ethylene glycol)-terminated alkanethiol self-assembled monolayers. *Langmuir* **2004**, *20* (20), 8931-8938.
70. Bolis, V.; Cavenago, A.; Fubini, B., Surface heterogeneity on hydrophilic and hydrophobic silicas: water and alcohols as probes for H-bonding and dispersion forces. *Langmuir* **1997**, *13* (5), 895-902.
71. Charmas, B.; Leboda, R., Effect of surface heterogeneity on adsorption on solid surfaces: application of inverse gas chromatography in the studies of energetic heterogeneity of adsorbents. *J. Chromatogr. A* **2000**, *886* (1), 133-152.
72. Isaienko, O.; Borguet, E., Hydrophobicity of Hydroxylated Amorphous Fused Silica Surfaces. *Langmuir* **2013**, *29* (25), 7885-7895.
73. Zhuravlev, L., The surface chemistry of amorphous silica. Zhuravlev model. *Colloids Surf., A* **2000**, *173* (1), 1-38.
74. Roach, P.; Farrar, D.; Perry, C. C., Interpretation of protein adsorption: surface-induced conformational changes. *J. Am. Chem. Soc.* **2005**, *127* (22), 8168-73.

75. Sethuraman, A.; Belfort, G., Protein structural perturbation and aggregation on homogeneous surfaces. *Biophys. J.* **2005**, *88* (2), 1322-33.
76. Talasaz, A. H.; Nemat-Gorgani, M.; Liu, Y.; Ståhl, P.; Dutton, R. W.; Ronaghi, M.; Davis, R. W., Prediction of protein orientation upon immobilization on biological and nonbiological surfaces. *Proc. Natl. Acad. Sci. U. S. A.* **2006**, *103* (40), 14773-14778.
77. Lhoest, J. B.; Detrait, E.; Van Den Bosch De Aguilar, P.; Bertrand, P., Fibronectin adsorption, conformation, and orientation on polystyrene substrates studied by radiolabeling, XPS, and ToF SIMS. *J. Biomed. Mater. Res.* **1998**, *41* (1), 95-103.
78. Marchesi, V.; Tillack, T.; Jackson, R.; Segrest, J.; Scott, R., Chemical characterization and surface orientation of the major glycoprotein of the human erythrocyte membrane. *Proc. Natl. Acad. Sci. U. S. A.* **1972**, *69* (6), 1445-1449.
79. Rabe, M.; Verdes, D.; Zimmermann, J.; Seeger, S., Surface organization and cooperativity during nonspecific protein adsorption events. *J. Phys. Chem. B* **2008**, *112* (44), 13971-13980.
80. Minton, A. P., Effects of excluded surface area and adsorbate clustering on surface adsorption of proteins: I. Equilibrium models. *Biophys. Chem.* **2000**, *86* (2), 239-247.
81. Chatelier, R. C.; Minton, A. P., Adsorption of globular proteins on locally planar surfaces: models for the effect of excluded surface area and aggregation of adsorbed protein on adsorption equilibria. *Biophys. J.* **1996**, *71* (5), 2367.
82. Asanov, A. N.; Delucas, L. J.; Oldham, P. B.; Wilson, W. W., Heteroenergetics of bovine serum albumin adsorption from good solvents related to crystallization conditions. *J. Colloid Interface Sci.* **1997**, *191* (1), 222-235.
83. Vasina, E. N.; Déjardin, P.; Rezaei, H.; Grosclaude, J.; Quiquampoix, H., Fate of prions in soil: Adsorption kinetics of recombinant unglycosylated ovine prion protein onto mica in laminar flow conditions and subsequent desorption. *Biomacromolecules* **2005**, *6* (6), 3425-3432.
84. Nygren, H.; Alaeddin, S.; Lundström, I.; Magnusson, K.-E., Effect of surface wettability on protein adsorption and lateral diffusion. Analysis of data and a statistical model. *Biophys. Chem.* **1994**, *49* (3), 263-272.

Chapter 3

Cadherin Diffusion in Supported Lipid Bilayers Exhibits Calcium-Dependent Dynamic Heterogeneity



Reproduced from Cai, Y. et al., *Biophysical Journal*, **2016**, *111* (12), 2658–2665.

3.1 ABSTRACT

Ca^{2+} ions are critical to cadherin ectodomain rigidity, which is required for the activation of adhesive functions. Therefore, changes in Ca^{2+} concentration, both in vivo and in vitro, can affect cadherin conformation and function. We employed single-molecule tracking to measure the diffusion of cadherin ectodomains tethered to supported lipid bilayers at varying Ca^{2+} concentrations. At a relatively high Ca^{2+} concentration of 2 mM, cadherin molecules exhibited a “fast” diffusion coefficient that was identical to that of individual lipid molecules in the bilayer

($D_{fast} \approx 3 \mu\text{m}^2/\text{s}$). At lower Ca^{2+} concentrations, where cadherin molecules were less rigid, the ensemble-average cadherin diffusion coefficient was systematically smaller. Individual cadherin trajectories were temporally heterogeneous, exhibiting alternating periods of fast and slow diffusion; the periods of slow diffusion ($D_{slow} \approx 0.1 \mu\text{m}^2/\text{s}$) were more prevalent at lower Ca^{2+} concentration. These observations suggested that more flexible cadherin ectodomains at lower Ca^{2+} concentration alternated between upright and lying-down conformations, where the latter interacted with more lipid molecules and experienced greater viscous drag.

3.2 INTRODUCTION

Cadherins are a group of transmembrane proteins that play essential roles in cell adhesion.¹⁻³ They rely on Ca^{2+} ions to maintain their elongated structure and enable their adhesive functions.⁴⁻⁸ The normal physiological extracellular calcium level is 2.12-2.62 mM; with ~40% of the Ca^{2+} ions binding to proteins and ~10% of them bound to various anions in complexes, the corresponding free calcium level is 1.16-1.31 mM.⁹⁻¹¹ In cell culture, a wide range of Ca^{2+} concentrations (even as low as 0.02 mM) are sometimes employed.¹²⁻¹⁴ Because cadherin structure is extremely sensitive to Ca^{2+} ions, fluctuations in Ca^{2+} concentration in the extracellular environment can influence the conformation of cadherin and ultimately affect their function.¹⁵⁻²⁰ While relatively small variations in Ca^{2+} concentration are associated with disease pathology in vivo, more significant decreases (to ~0.8 mM) were predicted in active synaptic clefts using simulations.²¹ Furthermore, remarkable drops (as low as 0.3 mM) were identified experimentally in synaptic clefts during high frequency stimulation.^{19, 20, 22} At such low Ca^{2+}

concentrations, the binding of Ca^{2+} would be significantly reduced, resulting in the loss of rigid cadherin ectodomain structure.²³

The conformation and transport of cadherin ectodomains on biomembranes are critical for cis/trans interactions and junction formation.^{8, 24-26} Although the effect of Ca^{2+} on the structure of cadherin extracellular fragments has been extensively studied, the effects of calcium-dependent conformational changes on the biomembrane transport of cadherin remain unclear. Various experimental techniques (e.g. circular dichroism spectroscopy, scanning electron microscopy) have been used to study cadherin extracellular domain conformations.^{4,5} However, these methods provide only ensemble-average information and are insensitive to the potential presence of multiple molecular populations and/or the dynamic heterogeneity of individual molecules. Here, we employed a high-throughput single-molecule tracking approach, which allowed the rapid and parallel acquisition of a large number of individual molecular trajectories and enabled statistically valid analysis of multiple modes and populations. This method allowed us to obtain detailed information about the interplay between cadherin diffusion and conformation at the molecular level. Specifically, we performed a series of Ca^{2+} concentration-dependent experiments, which provided a systematic picture of cadherin diffusion on lipid bilayers as a function of Ca^{2+} concentration. This allowed us to elucidate the inherent connection between diffusion and conformational changes in the cadherin extracellular region. The findings presented here provide new insights into dynamics of proteins on biological membranes in different environments.

3.3 EXPERIMENTAL METHODOLOGY

3.3.1 Materials

1,2-dioleoyl-sn-glycero-3-phosphocholine (DOPC), 1,2-dioleoyl-sn-glycero-3-[(N-(5-amino-1-carboxypentyl)iminodiacetic acid)succinyl] (nickel salt) (DGS-NTA-Ni) and 1,2-dioleoyl-*sn*-glycero-3-phosphoethanolamine-N-(lissamine rhodamine B sulfonyl) (ammonium salt) (DOPE-LR) were purchased from Avanti Polar Lipids, Inc.

The soluble, recombinant extracellular domain EC1-5 of *Xenopus* cleavage stage cadherin (C-cadherin) with a C-terminal hexahistidine tag were expressed by stably expressed in Chinese Hamster Ovary cells.^{27, 28} The soluble, expressed hexahistidine-tagged ectodomains were first purified by affinity chromatography on an Affigel column, as described.²⁸ Sodium dodecyl sulfate polyacrylamide gel electrophoresis (SDS PAGE) confirmed the purity of the final protein. The thus purified cadherin ectodomain was further labeled with Alexa Fluor 532 NHS ester (succinimidyl ester, Invitrogen, Carlsbad, CA), at a stoichiometry of ~4 fluorophores per molecule.²⁹

3.3.2 Sample Preparation

DOPC and DGS-NTA-Ni lipids were dissolved in chloroform with a mole ratio of 20,000:1 in a glass culture tube. After solvent evaporation under a stream of nitrogen, a thin film of lipids was formed on the side of the tube, which was then hydrated with HEPES buffer (containing 25 mM HEPES, 100 mM NaCl, 10 mM KCl and 0-2 mM CaCl₂, pH 7.4). The resulting aqueous suspension was vigorously mixed with vortex and then sonicated for 0.5 h. In

order to attain unilamellar liposomes with a more homogeneous size distribution, we extruded the suspension through a 50 nm filter membrane (Whatman) for 20 times. Fluorescently labeled cadherin ectodomains were added to the liposome solution and incubated for 2 h, allowing the formation of coordination bonds between the His-tags on the ectodomains and the nickel-chelated headgroups. The mole ratio of cadherin to DGS-NTA-Ni was controlled to be 1:1,000, leading to an appropriate cadherin surface density for single-molecule imaging (which was approximately equivalent to a surface area fraction of 10^{-6}).

To prepare supported lipid bilayers, glass coverslips (Electron Microscopy Sciences) were cleaned in warm piranha solution (~70 °C) and treated by UV-ozone [CAUTION: piranha is hazardous and should be handled with extreme caution]. The protein-modified liposomes were then introduced to the pretreated slides in a perfusion chamber. After incubating for 2 h at room temperature, liposomes fused on the substrate, and spontaneously formed a supported lipid bilayer.^{30, 31} The bilayer was rinsed thoroughly with water to remove excess liposomes and protein, and then exchanged into HEPES/CaCl₂ buffer at the desired Ca²⁺ concentration.^{32, 33} For control experiments, pure DOPC lipid bilayers and DOPC lipid bilayers containing a low concentration of fluorescent DOPE-LR as probes were prepared using the procedure described above. These bilayers were used to characterize the diffusivity of lipids within a supported lipid bilayer in the absence of cadherin.

3.3.3 Single-Molecule Tracking

All experiments were performed at room temperature using an objective-based Nikon Ti-E total internal reflection fluorescence microscope (TIRFM) with a 100x Apo TIRF oil

objective.³⁴ An EMCDD camera (iXon DU897) cooled to $-80\text{ }^{\circ}\text{C}$ was used to capture sequences of images (3000 frames per movie). Multiple movies with an acquisition time of either 40 ms or 50 ms were collected for each experimental condition. Fluorescently labeled cadherin ectodomains or lipids were excited by a 561 nm laser. We found that photo-bleaching and blinking were insignificant on the timescales of the measurements used in the analysis presented below, and the emission of non-labeled lipids was negligible. Given the acquisition time and excitation intensity that were determined to be optimal for these experiments, the localization precision was determined to be $\sim 60\text{ nm}$. Although the concentration of fluorescent molecules in solution was negligible in these experiments, the rapid diffusion of any residual solution-phase fluorescent molecules following the rinsing and buffer exchange was beyond the temporal resolution of TIRFM, and thus contributed only to the fluorescent background without affecting the apparent diffusion coefficients of molecules in the lipid bilayer.

3.3.4 Data Analysis

The diffusive trajectories of individual fluorescent molecules were determined using custom algorithms implemented in Mathematica as described previously.³⁵ Any trajectory with a total residence time shorter than 0.75 s was ignored for the purpose of statistical analysis. Due to the unavoidable defects in lipid bilayers, we observed a small fraction of immobile or highly confined trajectories in each experiment.³² To avoid the influence of this anomalous population, we removed any trajectory with a net average diffusion coefficient $<0.2\text{ }\mu\text{m}^2/\text{s}$.

3.3.4.1 Mean Squared Displacement and Mean Diffusion Coefficient – The ensemble diffusion coefficient D_E at each experimental condition was determined by calculating the

ensemble mean squared displacement (MSD) $\langle r^2(\tau) \rangle$ as a function of lag time τ . The corresponding function

$$\langle r^2(\tau) \rangle = 4D_E\tau \quad (\text{Eq. 3-1})$$

was fitted to a linear model. The apparent diffusion coefficient D of each single trajectory was calculated by the same method.

3.3.4.2 Diffusion Coefficient Distributions – Histograms of diffusion coefficients were generated and fitted to a reciprocal normal distribution.³⁶ According to the Einstein relation³⁷

$$D = \frac{k_B T}{f} \quad (\text{Eq. 3-2})$$

the diffusion coefficient D is inversely related to the friction factor f . Since the friction factor is expected to be Gaussian distributed ($1/D \sim N(\mu, \sigma^2)$) for a given population, the distribution of diffusion coefficients can be described by a reciprocal normal distribution

$$N_t(D) = \frac{P}{\sqrt{2\pi}\sigma D^2} \exp\left(-\frac{(1/D - \mu)^2}{2\sigma^2}\right) \quad (\text{Eq. 3-3})$$

where μ and σ are the mean and standard deviation of the Gaussian-distributed $1/D$, and P accounts for the number of trajectories used in the analysis. In general one might use a mixture of reciprocal normal distributions (each with characteristic values of μ and σ) to describe systems with multiple molecular populations, this was not necessary for the data presented here.

3.3.4.3 Step Size Distributions – The step sizes (absolute values of displacements) at a lag time of 50 ms were converted into histograms, potentially exhibiting multiple modes of diffusion. A Rayleigh mixture model was used to fit the distributions (32):

$$N_s(r) = Q \sum_{i=1}^M f_i \frac{r}{\lambda_i^2} \exp\left(\frac{-r^2}{2\lambda_i^2}\right) \quad (\text{Eq. 3-4})$$

where N_s is the number of steps with a displacement of r . The scale parameter λ_i is related to the diffusion coefficient D_i by $\lambda_i^2 = 2D_i\Delta t$ and f_i represents the corresponding fraction for the i th mode. M is the total number of modes. Q accounts for the number of trajectories used in the analysis. The average diffusion coefficient D_{avg} for each experimental condition was calculated using the expression

$$D_{\text{avg}} = \sum_{i=1}^M f_i D_i \quad (\text{Eq. 3-5})$$

3.4 RESULTS AND DISCUSSION

3.4.1 Calcium-Dependent Ensemble Average Diffusion

In order to investigate how the concentration of Ca^{2+} ions affects cadherin transport on lipid bilayers (DOPC), single-molecule experiments were performed at 5 different Ca^{2+} ion concentrations ranging from 0 mM to 2 mM. On average, the diffusion of the membrane-bound cadherin decreased systematically with decreasing Ca^{2+} concentration. For example, as shown in **Figure 3-1**, the slope of the mean squared displacement (MSD) vs time plot, which is associated with the ensemble-averaged diffusion coefficient, decreased systematically with decreasing Ca^{2+} concentration. At a concentration of 2 mM, where cadherin ectodomains were presumably saturated by Ca^{2+} ions and possessed a relatively rigid elongated structure,^{1, 3, 4, 8, 15, 38} the diffusion coefficient was determined to be $3.173 \pm 0.003 \mu\text{m}^2/\text{s}$. To understand this value, we

measured the diffusion coefficient of fluorescently labeled lipids in a pure lipid bilayer (DOPC/DOPE-LR) at the same Ca^{2+} concentration, and determined an almost identical value ($3.124 \pm 0.005 \mu\text{m}^2/\text{s}$). This result suggested that in its rod-like configuration at high Ca^{2+} concentration, each cadherin ectodomain interacted only with the lipid to which it was bound, and any additional friction associated with bulk water was negligible compared to the friction within the lipid bilayer.

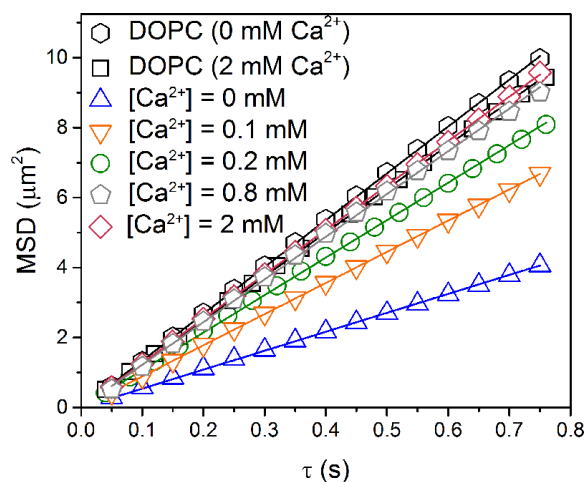


Figure 3-1. Ensemble mean squared displacements (MSD) vs lag time (τ) for the diffusion of cadherin in supported lipid bilayers at different Ca^{2+} concentrations (colored symbols) and for the diffusion of fluorescently labeled lipids (black symbols). Symbols represent experimental data points and solid lines represent linear fits.

When the Ca^{2+} ion concentration was decreased to 0.8 mM, the ensemble-average diffusion coefficient was reduced only slightly to $3.05 \pm 0.01 \mu\text{m}^2/\text{s}$. This value decreased further to $2.677 \pm 0.005 \mu\text{m}^2/\text{s}$ at a Ca^{2+} concentration of 0.2 mM, to $2.225 \pm 0.002 \mu\text{m}^2/\text{s}$ at a Ca^{2+} concentration of 0.1 mM, and eventually to $1.354 \pm 0.003 \mu\text{m}^2/\text{s}$ when the buffer was free of Ca^{2+} ions. Notably, in order to rule out a possible effect of Ca^{2+} on lipids, we measured the diffusion coefficient of fluorescently labeled lipids (DOPC/DOPE-LR) in a buffer free of Ca^{2+} ,

and attained a corresponding value of $3.346 \pm 0.005 \mu\text{m}^2/\text{s}$. This value was very close to the one in a buffer with 2 mM Ca^{2+} , demonstrating a negligible influence of Ca^{2+} concentration on the diffusivity of pure lipids. Because of the well-established dependence of the cadherin configuration on the Ca^{2+} concentration,^{4-8, 15} we hypothesized that the measured trend in diffusion coefficient was related to these conformational changes. Specifically, the fast diffusion at high Ca^{2+} concentration suggested that the rigid, fully-folded cadherin interacted with the bilayer only via the single lipid to which it was attached, while at lower Ca^{2+} concentrations, increasingly flexible cadherin ectodomains collapsed onto the lipid bilayer and therefore experienced increased friction, leading to slower diffusion.³² A conceptually similar type of conformation-dependent diffusion was previously observed by Herold et al,³⁹ who studied the motion of coiled and globular DNA adsorbed on cationic lipid bilayers. Interestingly, the trend of the ensemble-average diffusion coefficient with Ca^{2+} concentration correlated very strongly with the loss of cadherin secondary structure reported by Pokutta et al using circular dichroism spectroscopy.^{4, 15} At very low Ca^{2+} concentrations (0 – 0.2 mM), both the conformation and the diffusion changed rapidly with concentration; while at higher Ca^{2+} ion concentrations (> 0.2 mM), they were much less sensitive and gradually saturated. As shown below, this variation of secondary structure and mobility exhibited remarkable correlation.

While the correlation between cadherin conformation and ensemble-average diffusivity suggested a mechanistic connection between these properties, various molecular-level phenomena can lead to changes in ensemble averages. The conceptually simplest scenario involves the homogeneous diffusive slowing of a single cadherin population with decreasing Ca^{2+} concentration. However, the decrease in the ensemble-average diffusion may also be a consequence of heterogeneous behavior. For example, if the available Ca^{2+} ions were not

sufficient to saturate all cadherin molecules, multiple molecular populations could potentially be present (e.g. fast and slow) due to heterogeneous binding of Ca^{2+} ions with different cadherin molecules, and the relative fractions of these populations could vary systematically with Ca^{2+} concentration. Alternatively, even with only one molecular population, individual cadherin molecules may exhibit dynamic heterogeneity, switching between fast and slow modes within a given trajectory. Since the non-covalent binding of calcium to cadherin is highly reversible,^{4, 7, 15, 40} this diffusive heterogeneity could hypothetically be related to the dynamic association and dissociation of Ca^{2+} ions in calcium-deficient situations. These scenarios can be distinguished directly by careful statistical analysis of single molecule trajectories.

3.4.2 Step Size Distributions and Diffusive Heterogeneity

To determine whether the behavior was homogeneous or heterogeneous, we constructed histograms of step sizes (absolute displacements in 50 ms time intervals) based on molecular trajectories obtained from single molecule experiments, and employed a Rayleigh mixture model to fit and quantify the distributions (**Figure 3-2**). We observed distinct populations of step sizes with peaks at two locations, and the relative magnitudes of the two peaks varied systematically with Ca^{2+} concentration. This observation immediately allowed us to eliminate the possibility that the slowing with decreasing Ca^{2+} concentration was due to homogeneous slowing of a single cadherin molecular population.

The peaks in the histograms were observed at $\sim 0.10 \mu\text{m}$ (associated with an apparent diffusion coefficient of $\sim 0.1 \mu\text{m}^2/\text{s}$) and $\sim 0.56 \mu\text{m}$ (associated with an apparent diffusion coefficient of $\sim 3.1 \mu\text{m}^2/\text{s}$). These two peaks can be assigned to “slow” and “fast” modes or

populations, respectively. In **Figure 3-2a**, with no Ca^{2+} in the buffer, the step size distribution was dominated by the slow mode, while it was still heavy tailed due to a small number of

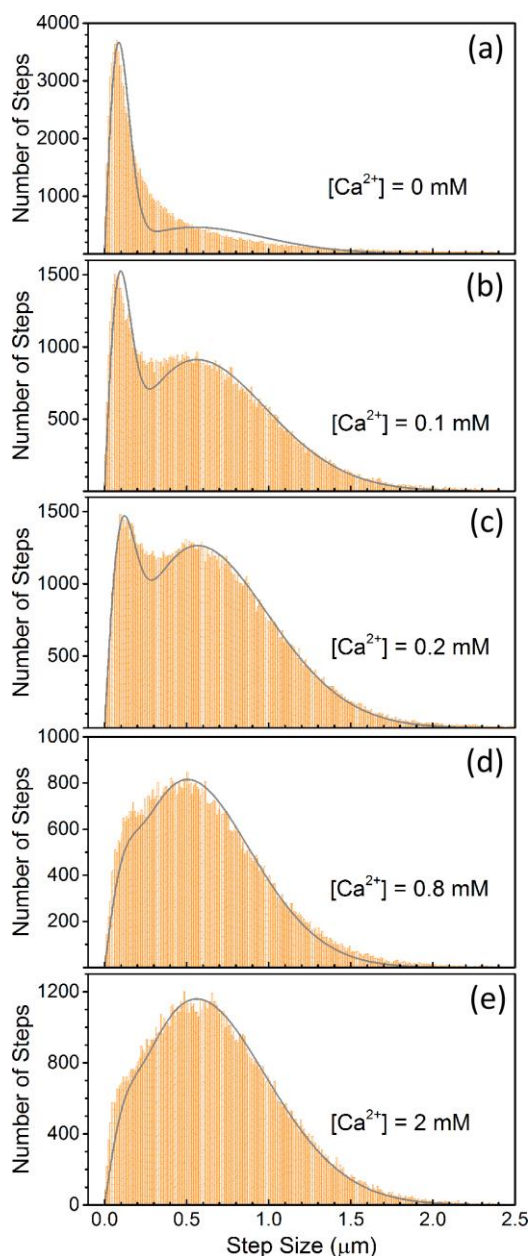


Figure 3-2. Histograms of step sizes for (a) 54,032 steps at $[\text{Ca}^{2+}] = 0$ mM, (b) 89,433 steps at $[\text{Ca}^{2+}] = 0.1$ mM, (c) 121,311 steps at $[\text{Ca}^{2+}] = 0.2$ mM, (d) 75740 steps at $[\text{Ca}^{2+}] = 0.8$ mM and (e) 94,862 steps at $[\text{Ca}^{2+}] = 2$ mM. Trajectories with overall diffusion coefficients lower than $0.2 \mu\text{m}^2/\text{s}$ were removed before plotting those histograms. Solid lines represent fixed to a Rayleigh-distribution mixture model.

apparent long steps. As Ca^{2+} concentration increased, from **Figure 3-2a** to **Figure 3-2e**, the peak representing the slow mode decreased and the peak associated with the fast mode increased systematically, completely dominating the distribution at the highest Ca^{2+} ion concentration. Additionally, it is likely that multiple unresolved states were present in the slow mode regime and the values of λ_I (the scale parameter associated with the slow diffusion mode as defined in Equation 4) increased slightly with increasing Ca^{2+} (**Table B-1** in Appendix B), indicating that the overall motion associated with the slow modes became faster.

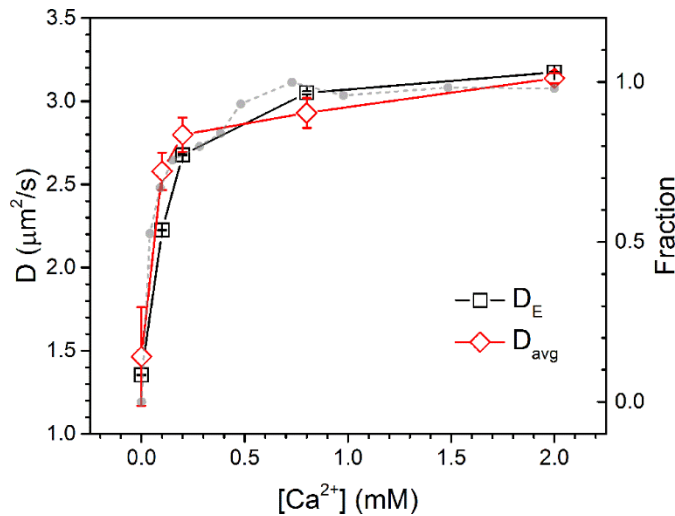


Figure 3-3. Ensemble diffusion coefficients (D_E , calculated by fitting the MSD plots) and average diffusion coefficients (D_{avg} , calculated by fitting the step size distributions) of cadherin on supported lipid bilayers as a function of Ca^{2+} concentrations. Error bars represent fitting uncertainties obtained using the respective statistical models. Symbols in light grey represent the recovery of cadherin molar ellipticity (data adapted from Fig 4 in reference 4).

According to the fitting parameters (**Table B-1** in Appendix B), by adding 2 mM Ca^{2+} to the buffer, the fraction of steps associated with the slow mode/population decreased from 0.54 to 0.02, while the fraction of steps associated with the fast mode/population increased from 0.46 to 0.98. Interestingly, even in the absence of Ca^{2+} , some long apparent steps were still observed,

suggesting that cadherin molecules could still spontaneously adopt conformations that facilitate fast diffusion, even in the absence of Ca^{2+} . **Figure 3-3** shows that the average diffusion coefficients calculated by fitting the step size distributions for a single lag time (see **Table B-1** in Appendix B) were in fact very close to the ones calculated by fitting the MSD plots as a function of lag time (see above and **Table B-2** in Appendix B). It also allows us to visualize the correlation between the cadherin secondary structure measured using circular dichroism spectroscopy (data adapted from Fig 4 in reference 4, represented by grey symbols) and the average cadherin diffusion coefficient as a function of Ca^{2+} concentrations,⁴ suggesting a potential correlation between the conformation and diffusion of cadherin molecules.

3.4.3 Support for a Single Diffusive Population

While **Figure 3-2** clearly indicates the presence of heterogeneity, it does not explicitly distinguish between the possibility of heterogeneous populations (some molecules move rapidly and some slowly) and the possibility of dynamic heterogeneity (individual trajectories of a single molecular population switch dynamically between slow and fast modes). To test for the presence of multiple molecular populations, histograms of molecular diffusion coefficients (i.e. for individual trajectories) at different Ca^{2+} concentrations were accumulated and analyzed (**Figure 3-4**). Diffusion coefficients presented here correspond to the “short-range diffusion coefficients” in the formalism of Saxton et al,⁴¹ and did not show a dependence on trajectory length.

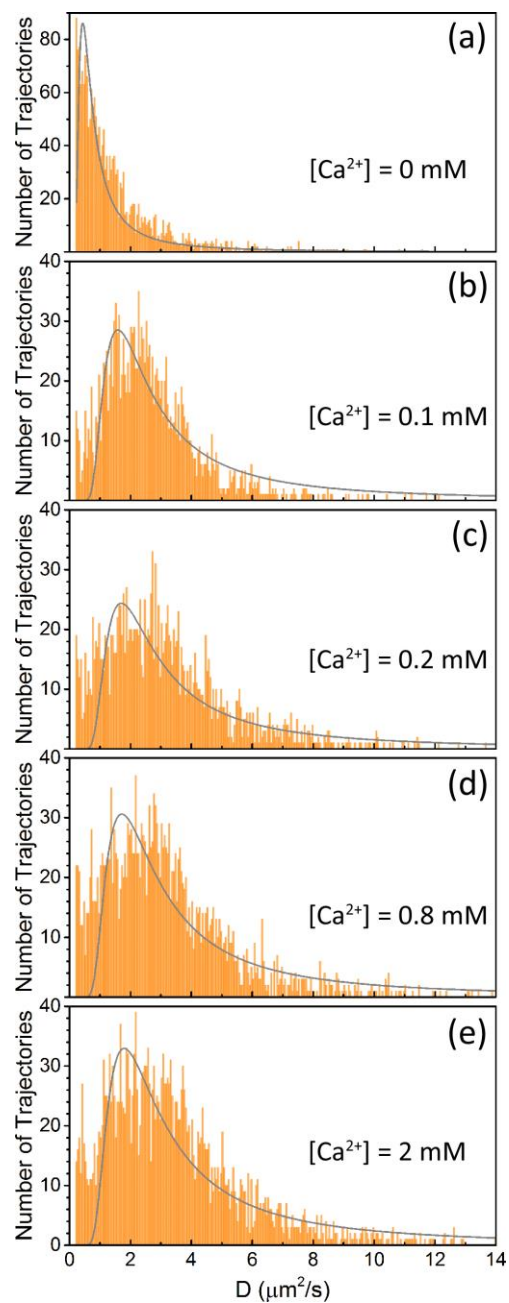


Figure 3-4. Histograms of diffusion coefficients for (a) 2214 trajectories at $[\text{Ca}^{2+}] = 0 \text{ mM}$, (b) 2159 trajectories at $[\text{Ca}^{2+}] = 0.1 \text{ mM}$, (c) 2595 trajectories at $[\text{Ca}^{2+}] = 0.2 \text{ mM}$, (d) 2742 trajectories at $[\text{Ca}^{2+}] = 0.8 \text{ mM}$ and (e) 2695 trajectories at $[\text{Ca}^{2+}] = 2 \text{ mM}$. Trajectories with overall diffusion coefficients lower than $0.2 \mu\text{m}^2/\text{s}$ were removed. Solid lines represent reciprocal normal fits.

Notably, each of these distributions exhibited only one peak, consistent with the presence of a single population, which is in conflict with the alternative hypothesis that multiple conformational populations may be present due to heterogeneous binding of Ca^{2+} ions. As Ca^{2+} concentration was increased, (**Figures 3-4 a–d**) the location of the peak shifted to the right, indicating that as cadherin ectodomains were further saturated by Ca^{2+} ions, they diffused faster on average. As described above, these distributions were statistically analyzed, assuming that the friction factors (characteristic values of friction, represented by μ) for the diffusion of lipid-binding cadherin ectodomains were Gaussian-distributed (and therefore that the diffusion coefficients, which were associated with the inverse of frictions, should follow a reciprocal normal distribution as described in Eq. 4). This model provided satisfactory fits in all cases, again suggesting that only a single molecular population was present. The fitting parameters are shown in **Table B-3** in Appendix B. With increasing Ca^{2+} concentration, the value of μ decreased, indicating lower average friction as cadherin ectodomains “stood up” on the lipid bilayer. Correspondingly, the inverse-friction $1/\mu$ (expected to be proportional to the apparent diffusion coefficient through the Einstein relation) increased systematically while adding Ca^{2+} ions. Notably, the trend of $1/\mu$, and of the ensemble-average diffusion coefficient D_E , vs Ca^{2+} concentration were similar, demonstrating the effectiveness of this fitting model (**Table B-3**).

Since only one molecular population was identified in the distributions of diffusion coefficients (**Figure 3-3**), we ascribed the presence of two peaks in the step size distributions (**Figure 3-2**) to the dynamic switching of diffusion modes within each trajectory. Moreover, this behavior can be directly observed in representative trajectories that randomly assembled, as shown in **Figure 3-5**. In the absence of Ca^{2+} ions in the buffer (**Figure 3-5a**), cadherin molecules were predominantly observed in the slow mode (represented by short steps), while they

occasionally shifted into the fast mode as represented by rare long steps. With 0.1 mM Ca^{2+} in the buffer (**Figure 3-5b**), many more long steps were identified, and the shifting between the two states became more pronounced. At the saturated Ca^{2+} ion concentration (**Figure 3-5c**), short steps were seen only rarely, and cadherin molecules diffused essentially in the fast mode.

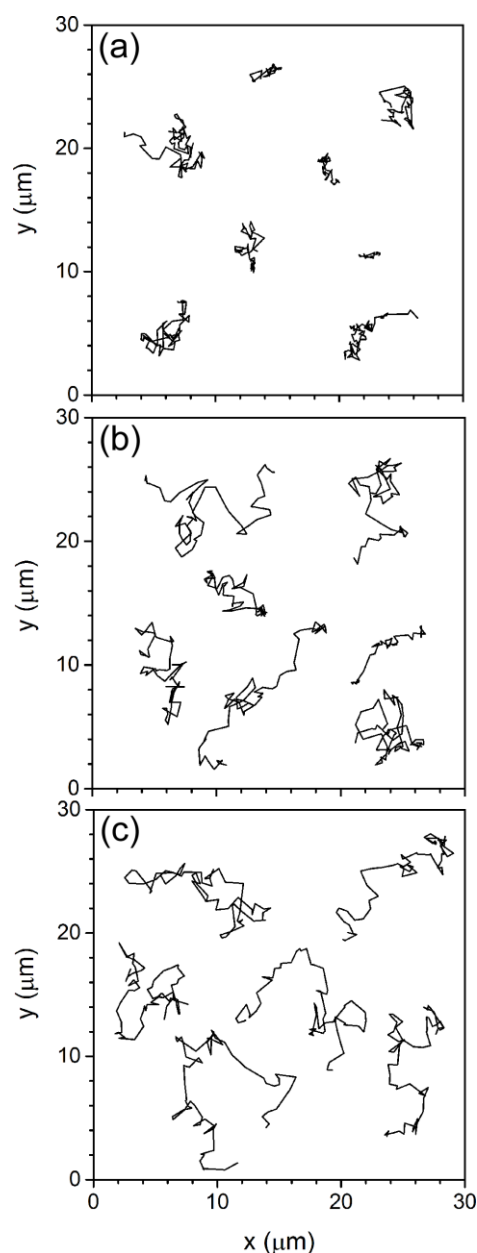


Figure 3-5. Representative trajectories of cadherin diffusion on lipid bilayers at Ca^{2+} concentrations of (a) 0 mM, (b) 0.1 mM and (c) 2 mM.

3.4.4 Interpretation of the Observed Dynamic Heterogeneity

Based on the calcium-dependent heterogeneous diffusion of cadherin that we observed, and the strong dependence of cadherin conformation on Ca^{2+} concentrations,^{4, 8, 15, 38} we hypothesized that the dynamic heterogeneity of cadherin on lipid bilayers was potentially correlated with conformational changes. Specifically, when a cadherin ectodomain diffuses in the presence of a lipid bilayer, it can undergo conformational changes, which may be caused by the dynamic association and dissociation of Ca^{2+} ions. When supported by Ca^{2+} ions, a rigid cadherin molecule is most likely to “stand up” and interact with only the one lipid to which it is bound, therefore diffusing in a fast mode identical to that of individual lipid molecules. However, transient Ca^{2+} dissociation from various binding sites would render the protein more flexible,^{4, 15, 38} and at very low Ca^{2+} concentrations, cadherin could intermittently collapse onto the lipid bilayer, thus interacting with more lipid molecules, experiencing more friction, and slowing the motion.³² The characteristic diffusion coefficient associated with the slow mode was roughly 1/30 of the diffusion coefficient for the fast mode, suggesting that if this hypothesis is correct, the collapsed cadherin molecule in the slow mode was contacting as many as 30 lipids (assuming a simple superposition model for the friction factor). Considering the size of a lipid headgroup ($\sim 70 \text{ \AA}^2$) and the dimensions of a cadherin domain ($\sim 45 \text{ \AA} \times 30 \text{ \AA}$), the area of 30 lipids is equivalent to 1-2 of the five extracellular domains, when lying down.^{1, 7, 25, 42-46}

3.5 CONCLUSIONS

The concentration of Ca^{2+} ions can both determine the cadherin conformation, and influence cadherin diffusion on supported lipid bilayers. Specifically, as the cadherin ectodomain became more flexible with decreasing Ca^{2+} concentration,^{4, 15, 38} we also observed overall slower cadherin diffusion on the membrane. By analyzing the distributions of diffusion coefficients and step sizes, we found that cadherin ectodomains alternated between slow and fast modes when diffusing in association with a lipid bilayer. With decreasing Ca^{2+} concentration, cadherin molecules experienced more friction and spent more time in the slow state, possibly because they adopted more flexible conformations and were in contact with more lipids. In contrast with the typical behavior of proteins on solid surfaces, where the unfolding of proteins is generally irreversible and can sometimes cause aggregation,⁴⁷⁻⁵⁰ the results reported above suggest that the conformational changes of cadherin on lipid bilayers membrane appears to be highly dynamic and reversible. While the correlation between the calcium-dependence of diffusion and conformation is compelling, it is also possible that Ca^{2+} concentration may cause indirect effects that could influence the diffusive dynamics of cadherin for other reasons; therefore, future work will address the structural dynamics of cadherin directly.

3.6 REFERENCES

1. Leckband, D.; de Rooij, J., Cadherin adhesion and mechanotransduction. *Annual review of cell and developmental biology* **2014**, *30*, 291-315.
2. Takeichi, M., Cadherin cell adhesion receptors as a morphogenetic regulator. *Science* **1991**, *251* (5000), 1451-1455.

3. Leckband, D.; Prakasam, A., Mechanism and dynamics of cadherin adhesion. *Annu. Rev. Biomed. Eng.* **2006**, 8, 259-287.
4. Pokutta, S.; Herrenknecht, K.; Kemler, R.; ENGEL, J., Conformational changes of the recombinant extracellular domain of E-cadherin upon calcium binding. *European journal of biochemistry* **1994**, 223 (3), 1019-1026.
5. Pertz, O.; Bozic, D.; Koch, A. W.; Fauser, C.; Brancaccio, A.; Engel, J., A new crystal structure, Ca²⁺ dependence and mutational analysis reveal molecular details of E-cadherin homoassociation. *The EMBO journal* **1999**, 18 (7), 1738-1747.
6. Grunwald, G. B., The structural and functional analysis of cadherin calcium-dependent cell adhesion molecules. *Current opinion in cell biology* **1993**, 5 (5), 797-805.
7. Nagar, B.; Overduin, M.; Ikura, M.; Rini, J. M., Structural basis of calcium-induced E-cadherin rigidification and dimerization. *Nature* **1996**.
8. Vunnam, N.; Pedigo, S., Sequential binding of calcium leads to dimerization in neural cadherin. *Biochemistry* **2011**, 50 (14), 2973-2982.
9. Elzouki, A. Y.; Stapleton, F.; Harfi, H.; Oh, W.; Whitley, R.; Nazer, H., *Textbook of clinical pediatrics*. Springer Science & Business Media: 2011.
10. Andreasen, P., Free and total calcium concentrations in the blood of rainbow trout, *Salmo gairdneri*, during 'stress' conditions. *J. Exp. Biol.* **1985**, 118, 111-120.
11. Moore, E. W., Ionized calcium in normal serum, ultrafiltrates, and whole blood determined by ion-exchange electrodes. *J. Clin. Invest.* **1970**, 49 (2), 318.
12. Hennings, H.; Michael, D.; Cheng, C.; Steinert, P.; Holbrook, K.; Yuspa, S. H., Calcium regulation of growth and differentiation of mouse epidermal cells in culture. *Cell* **1980**, 19 (1), 245-254.
13. Yuspa, S. H.; Koehler, B.; Kulesz-Martin, M.; Hennings, H., Clonal growth of mouse epidermal cells in medium with reduced calcium concentration. *J. Invest. Dermatol.* **1981**, 76 (2), 144-146.
14. Boyce, S. T.; Ham, R. G., Calcium-regulated differentiation of normal human epidermal keratinocytes in chemically defined clonal culture and serum-free serial culture. *J. Invest. Dermatol.* **1983**, 81, 33-40.

15. Koch, A. W.; Pokutta, S.; Lustig, A.; Engel, J., Calcium binding and homoassociation of E-cadherin domains. *Biochemistry* **1997**, *36* (25), 7697-7705.
16. Maurer, P.; Hohenester, E.; Engel, J., Extracellular calcium-binding proteins. *Current opinion in cell biology* **1996**, *8* (5), 609-617.
17. Brown, E. M.; Vassilev, P. M.; Hebert, S. C., Calcium ions as extracellular messengers. *Cell* **1995**, *83* (5), 679-682.
18. Hou, S. H.; Zhao, J.; Ellman, C. F.; Hu, J.; Griffin, Z.; Spiegel, D. M.; Bourdeau, J. E., Calcium and phosphorus fluxes during hemodialysis with low calcium dialysate. *Am. J. Kidney Dis.* **1991**, *18* (2), 217-224.
19. Benninger, C.; Kadis, J.; Prince, D., Extracellular calcium and potassium changes in hippocampal slices. *Brain Res.* **1980**, *187* (1), 165-182.
20. Nicholson, C.; Ten Bruggencate, G.; Stockle, H.; Steinberg, R., Calcium and potassium changes in extracellular microenvironment of cat cerebellar cortex. *J. Neurophysiol.* **1978**, *41* (4), 1026-1039.
21. Wiest, M. C.; Eagleman, D. M.; King, R. D.; Montague, P. R., Dendritic spikes and their influence on extracellular calcium signaling. *Journal of neurophysiology* **2000**, *83* (3), 1329-1337.
22. Kim, S. A.; Tai, C.-Y.; Mok, L.-P.; Mosser, E. A.; Schuman, E. M., Calcium-dependent dynamics of cadherin interactions at cell-cell junctions. *Proceedings of the National Academy of Sciences* **2011**, *108* (24), 9857-9862.
23. Baumgartner, W.; Golenhofen, N.; Grundhöfer, N.; Wiegand, J.; Drenckhahn, D., Ca²⁺ dependency of N-cadherin function probed by laser tweezer and atomic force microscopy. *The Journal of neuroscience* **2003**, *23* (35), 11008-11014.
24. Biswas, K. H.; Hartman, K. L.; Yu, C.-h.; Harrison, O. J.; Song, H.; Smith, A. W.; Huang, W. Y.; Lin, W.-C.; Guo, Z.; Padmanabhan, A., E-cadherin junction formation involves an active kinetic nucleation process. *Proc. Natl. Acad. Sci. U. S. A.* **2015**, *112* (35), 10932-10937.
25. Wu, Y.; Jin, X.; Harrison, O.; Shapiro, L.; Honig, B. H.; Ben-Shaul, A., Cooperativity between trans and cis interactions in cadherin-mediated junction formation. *Proceedings of the National Academy of Sciences* **2010**, *107* (41), 17592-17597.

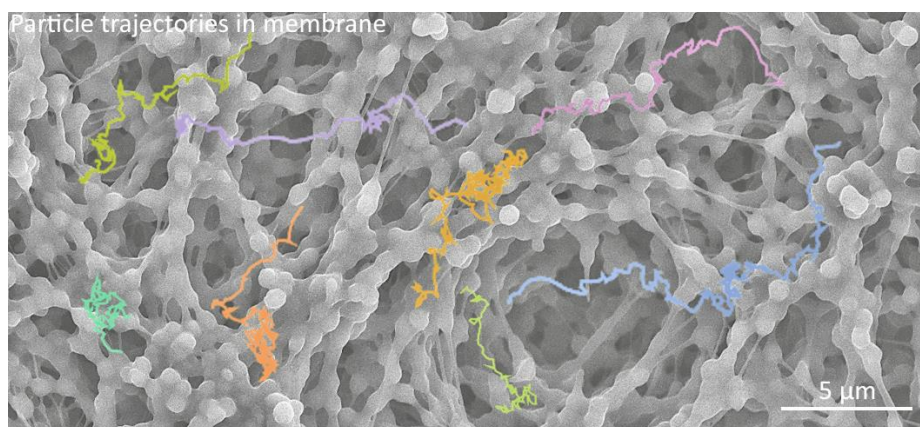
26. Boggon, T. J.; Murray, J.; Chappuis-Flament, S.; Wong, E.; Gumbiner, B. M.; Shapiro, L., C-cadherin ectodomain structure and implications for cell adhesion mechanisms. *Science* **2002**, *296* (5571), 1308-1313.
27. Prakasam, A.; Maruthamuthu, V.; Leckband, D., Similarities between heterophilic and homophilic cadherin adhesion. *Proc. Natl. Acad. Sci. USA* **2006**, *103* (42), 15434-15439.
28. Sivasankar, S.; Briehar, W.; Lavrik, N.; Gumbiner, B.; Leckband, D., Direct molecular force measurements of multiple adhesive interactions between cadherin ectodomains. *Proc. Natl. Acad. Sci. USA* **1999**, *96* (21), 11820-11824.
29. Nikiforov, T. T.; Beechem, J. M., Development of homogeneous binding assays based on fluorescence resonance energy transfer between quantum dots and Alexa Fluor fluorophores. *Anal. Biochem.* **2006**, *357* (1), 68-76.
30. Cremer, P. S.; Boxer, S. G., Formation and spreading of lipid bilayers on planar glass supports. *The Journal of Physical Chemistry B* **1999**, *103* (13), 2554-2559.
31. Richter, R. P.; Bérat, R.; Brisson, A. R., Formation of solid-supported lipid bilayers: an integrated view. *Langmuir* **2006**, *22* (8), 3497-3505.
32. Knight, J. D.; Lerner, M. G.; Marciano-Velázquez, J. G.; Pastor, R. W.; Falke, J. J., Single molecule diffusion of membrane-bound proteins: window into lipid contacts and bilayer dynamics. *Biophysical journal* **2010**, *99* (9), 2879-2887.
33. Ziemba, B. P.; Knight, J. D.; Falke, J. J., Assembly of membrane-bound protein complexes: detection and analysis by single molecule diffusion. *Biochemistry* **2012**, *51* (8), 1638-1647.
34. Wang, D.; Hu, R.; Mabry, J. N.; Miao, B.; Wu, D. T.; Koynov, K.; Schwartz, D. K., Scaling of Polymer Dynamics at an Oil–Water Interface in Regimes Dominated by Viscous Drag and Desorption-Mediated Flights. *J. Am. Chem. Soc.* **2015**, *137* (38), 12312-12320.
35. Honciuc, A.; Harant, A. W.; Schwartz, D. K., Single-molecule observations of surfactant diffusion at the solution– solid interface. *Langmuir* **2008**, *24* (13), 6562-6566.
36. Johnson, N. L.; Kotz, S.; Balakrishnan, N., *Continuous univariate distributions*. John Wiley & Sons: New York, 1994.

37. Edward, J. T., Molecular volumes and the Stokes-Einstein equation. *J. Chem. Educ.* **1970**, *47* (4), 261.
38. Sotomayor, M.; Schulten, K., The allosteric role of the Ca²⁺ switch in adhesion and elasticity of C-cadherin. *Biophys. J.* **2008**, *94* (12), 4621-4633.
39. Herold, C.; Schwille, P.; Petrov, E. P., DNA condensation at freestanding cationic lipid bilayers. *Phys. Rev. Lett.* **2010**, *104* (14), 148102.
40. Courjean, O.; Chevreux, G.; Perret, E.; Morel, A.; Sanglier, S.; Potier, N.; Engel, J.; Van Dorsselaer, A.; Feracci, H., Modulation of E-cadherin monomer folding by cooperative binding of calcium ions. *Biochemistry* **2008**, *47* (8), 2339-2349.
41. Saxton, M. J., Single-particle tracking: the distribution of diffusion coefficients. *Biophysical journal* **1997**, *72* (4), 1744.
42. Chang, H.; Reitstetter, R.; Gruener, R., Lipid-ion channel interactions: increasing phospholipid headgroup size but not ordering acyl chains alters reconstituted channel behavior. *J. Membr. Biol.* **1995**, *145* (1), 13-19.
43. Marsh, D., Intrinsic curvature in normal and inverted lipid structures and in membranes. *Biophys. J.* **1996**, *70* (5), 2248.
44. Koltover, I.; Salditt, T.; Safinya, C., Phase diagram, stability, and overcharging of lamellar cationic lipid-DNA self-assembled complexes. *Biophys. J.* **1999**, *77* (2), 915-924.
45. Chothia, C.; Jones, E. Y., The molecular structure of cell adhesion molecules. *Annual review of biochemistry* **1997**, *66* (1), 823-862.
46. Lambert, O.; Taveau, J.-C.; Him, J. L. K.; Al Kurdi, R.; Gulino-Debrac, D.; Brisson, A., The basic framework of VE-cadherin junctions revealed by cryo-EM. *J. Mol. Biol.* **2005**, *346* (5), 1193-1196.
47. Cai, Y.; Schwartz, D. K., Influence of protein surface coverage on anomalously strong adsorption sites. *ACS Appl. Mater. Interfaces* **2015**.
48. Roach, P.; Farrar, D.; Perry, C. C., Interpretation of protein adsorption: surface-induced conformational changes. *J. Am. Chem. Soc.* **2005**, *127* (22), 8168-73.

49. Rabe, M.; Verdes, D.; Zimmermann, J.; Seeger, S., Surface organization and cooperativity during nonspecific protein adsorption events. *J. Phys. Chem. B* **2008**, *112* (44), 13971-13980.
50. Sethuraman, A.; Belfort, G., Protein structural perturbation and aggregation on homogeneous surfaces. *Biophys. J.* **2005**, *88* (2), 1322-33.

Chapter 4

Mapping the Functional Tortuosity and Spatio-temporal Heterogeneity of Porous Polymer Membranes with Super-Resolution Nanoparticle Tracking



Reproduced from Cai, Y. and Schwartz, D. K., *ACS Applied Materials & Interfaces*, **2017**, 9 (49), 43258–43266.

4.1 ABSTRACT

As particles flow through porous media, they follow complex pathways and experience heterogeneous environments that are challenging to characterize. Tortuosity is often used as a parameter to characterize the complexity of pathways in porous materials and is useful in understanding hindered mass transport in industrial filtration and mass separation processes. However, conventional calculations of tortuosity provide only average values under static

conditions; they are insensitive to the intrinsic heterogeneity of porous media and do not account for potential effects of operating conditions. Here, we employ a high-throughput nanoparticle tracking method, which enables the observation of actual particle trajectories in polymer membranes under relevant operating conditions. Our results indicate that tortuosity is not simply a structural material property, but is instead a functional property that depends on flow rate and particle size. We also resolved the spatio-temporal heterogeneity of flowing particles in these porous media. The distributions of tortuosity and of local residence/retention times were surprisingly broad, exhibiting heavy tails representing a population of highly tortuous trajectories and local regions with anomalously long residence times. Interestingly, local tortuosity and residence times were directly correlated, suggesting the presence of highly confining regions that cause more meandering trajectories and longer retention times. The comprehensive information about tortuosity and spatio-temporal heterogeneity provided by these methods will advance the understanding of complex mass transport and assist rational design and synthesis of porous materials.

4.2 INTRODUCTION

Hindered mass transport is essential to many applications including water filtration, chromatography, groundwater movement, heterogeneous catalytic processes and cancer therapeutics.¹⁻⁹ Though it has been studied intensively for decades, there are no universal models capable of predicting mass transport quantitatively due to the complexity of real porous materials. Tortuosity is a specific parameter that can be used to quantify the complexity of pathways in porous materials, and to study the travel distance and time of particle transport.¹⁰⁻¹³ It is defined

geometrically by the ratio of the contour length to the end-to-end distance (i.e. Euclidean length) of pathways.¹⁰ A variety of approaches have been applied to characterize the tortuosity of porous materials. For example, the effective tortuosity can be determined by comparing the diffusion coefficients of solutes in porous media and in bulk solvent using nuclear magnetic resonance (NMR),¹⁴ however, the tortuosity calculated under stagnant conditions in this approach provides only static structural information at limited length scales. Electrical conductivity measurements can also be used to determine the effective tortuosity of some porous materials.^{15, 16} However, since conductivity is highly sensitive to the cross-sectional area of pathways, it is difficult to unambiguously interpret these measurements in the context of particle pathways in mass transport processes.^{17, 18} Additionally, there is a vast literature providing mathematical models to characterize tortuosity with computational methods.^{10, 17, 19} While some of the models are highly idealized,²⁰⁻²² others are more empirical and account for particle dispersion or constrictions in porous materials.²³⁻²⁵ Still, none these approaches can identify actual pathways in porous media and measure tortuosity directly under varying operating conditions.

The relevant tortuosity of a specific material is determined by the actual pathways through which particles flow. For example, in water filtration processes, we hypothesize that these pathways are highly dependent on operating parameters such as flow rate and particle size. While conventional methods neglect the significant impacts of operating conditions and fail to provide direct measurements of pathways,^{14, 16, 19} single-particle tracking enable the direct observation of tracer particle trajectories in porous media, including membranes and hydrogel matrices.²⁶⁻²⁸ In the present work, we developed and employed a high-throughput single-particle tracking approach under flow conditions, allowing us to acquire and analyze actual particle trajectories and achieve statistically meaningful results. Specifically, we used polymer filtration

membranes as model porous media and investigated the transport of different sizes of tracer particles under various flow conditions in order to study the impacts of operating conditions on apparent tortuosity. Compared to conventional methods that measure tortuosity under stagnant conditions, this approach provides information about porous materials under a range of flow conditions that are relevant to practical operating conditions and permits the examination of heterogeneous transport behavior, i.e. the tortuosity of individual pathways and the retention of tracer particles at different locations. This approach provides detailed spatial-temporal information about particle trajectories that is necessary feedback for the rational design of filtration media and other porous materials.

4.3 EXPERIMENTAL METHODOLOGY

4.3.1 Materials and Sample Preparation

Durapore (PVDF) filtration membranes were purchased from MilliporeSigma. They have a nominal pore size of 0.65 μm and a thickness of 120 μm (**Figure 4-1 a, b**). Membranes were cut into annuli with an inner diameter of 7 mm and an outer diameter of 8 mm. In each experiment, an annulus of membrane was sealed in the flow cell between a glass coverslip and a metal plate with integrated inlet and outlet tubes (diameter = 0.5 mm) as shown in **Figure 4-1c**. Tracer particle solution was introduced from the inlet (in the center of the annulus) and flowed radially outward through the 500 μm -wide annulus of membrane. Given that the area of the field of view ($\sim 100 \times 100 \mu\text{m}^2$) was small relative to the curvature of the annulus, the direction of flow within a field of view showed minimal divergence. This flow represented a dead-end

filtration process in which fluid was constrained to flow through the membrane sample (**Figure 4-1c**). Since the membrane microstructure was nominally isotropic, it was expected that the transport (parallel to the focal plane) was representative. In order to minimize light scattering from the internal surfaces of porous materials, index-matching liquid ($n=1.42$) was formulated with isopropyl alcohol and Triton X-100 (volume ratio 64:36).^{26, 27, 29} Triton X-100 also worked as a surfactant to reduce nonspecific adsorption of nanoparticles to the internal membrane surfaces. The solvent showed Newtonian properties in rheology tests (see **Figure C-1** in Appendix C for more details).³⁰ FluoSpheres carboxylate-modified microspheres (Invitrogen) with nominal sizes of 0.04 μm (dark red fluorescent, 660/680) and 0.2 μm (orange fluorescent, 540/560) were used as tracer particles (see **Figure C-2** in Appendix C for particle hydrodynamic radius characterization). For single particle tracking experiments, the volume fractions of nanoparticle solutions were controlled to be in the range $10^{-8} - 10^{-6}$ to minimize particle-particle interactions and enable localization of individual particles. A flow rate controlling syringe pump (NE-1000) was used to provide pressure driven flows. The experimentally accessible range of particle velocity in the membrane was 1—10 $\mu\text{m/s}$; this was limited by various parameters, including the imaging speed of the camera, the injection rate of the syringe pump and the pressure limit of the flow cell. Taking into account the membrane porosity of 75%, this range of velocity translated to an effective flux range of approximately 2.7-27 $\text{L}/(\text{h}\cdot\text{m}^2)$.

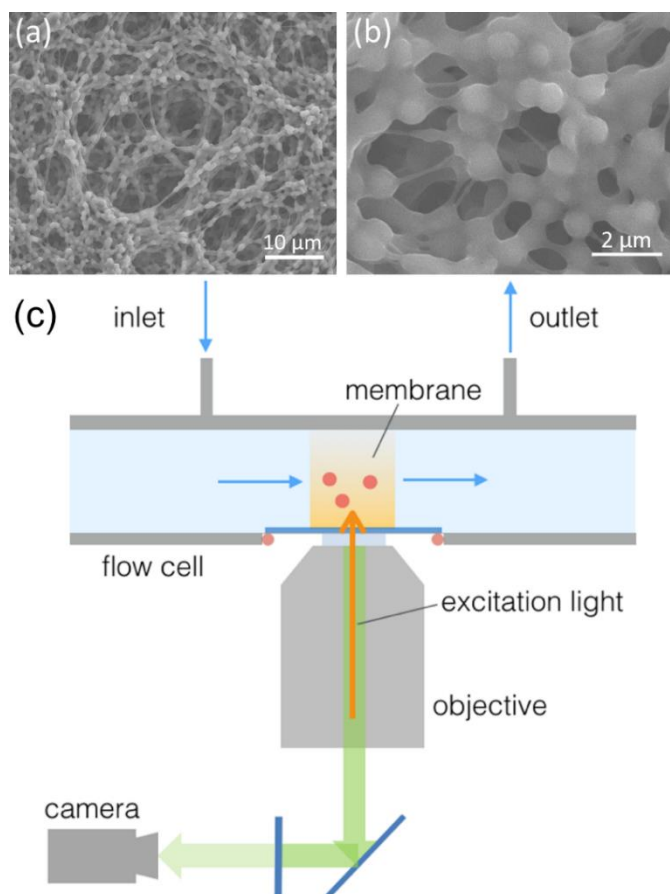


Figure 4-1. (a, b) Scanning electron microscope (SEM) images of Durapore (PVDF) filtration membranes with nominal pore size of 0.65 μm . (c) Schematic diagram showing the flow cell construction (only the part of membrane annulus being imaged is shown) and the imaging system.

4.3.2 Single-Particle Tracking

All experiments were performed at room temperature using a Nikon Ti-E epifluorescence microscope with a CFI Plan Apo Lambda 100 \times oil immersion objective. A CMOS camera (Hamamatsu) was used to capture images with a pixel size of 0.26 μm and an acquisition time of 50 ms. Multiple movies (3,000 frames per movie) were collected for each experimental condition. Dark red fluorescent particles were illuminated by a 640 nm diode-pumped solid state laser (CrystaLaser) and orange fluorescent particles were illuminated by a 532 nm diode-pumped solid state laser (Cobolt AB). A 532/638 C-TIRF filter cube (Chroma) was used in the light path. Trajectories of individual particles were determined using custom algorithms implemented in Mathematica as described previously.³¹ Any trajectory with a total residence time shorter than 0.5 s was ignored for the purpose of statistical analysis. Several thousand trajectories (contributing tens of thousands of sub-trajectories) were analyzed for each observation. Within the flow cell, the mean direction of flow was nominally parallel to the focal plane. Given the depth of focus of $\sim 3\mu\text{m}$, it was expected that the beginning and end of trajectories were defined by a particle's entry and exit from the focal volume of the microscope, so particles whose trajectories frequently meandered large distances in the z -direction were generally excluded from the analysis. The analysis therefore emphasized trajectories that happened to have large residence times within the focal volume, which was extensive in the x - y plane, but shallow in the z -direction. However, since the membrane material was isotropic, it was expected that these trajectories were representative. Inevitably, a small fraction of tracer particles adsorbed to the interior surface of membrane (perhaps to anomalously strong binding sites) and were immobile over the entire observation period of a given experiments.³² These immobile trajectories represent abnormally large apparent tortuosity values (sometimes on the order of 10^5) and long

retention times that exceeded the scope of observation. Therefore, it was impossible to measure the actual retention times and tortuosity of these immobile particles accurately. Since these anomalous values were not relevant to the actual flow pathways in the membrane and could potentially skew the analysis, immobile trajectories were excluded from the analysis to avoid the influence of this anomalous population (~20% for 0.04 μm tracer particles and ~10% for 0.2 μm tracer particles).³³ Three dimensional (3D) tracking experiments were also performed under a subset of operating conditions using double-helix point spread function (DH-PSF) microscopy (SPINDLE module, DoubleHelix LLC, Boulder, CO).^{34, 35}

4.3.3 Data Analysis

4.3.3.1 Mean squared displacements – Diffusion coefficients for tracer particles suspended in bulk solvent (D_b) and within the internal pore space of membranes (D_m) were determined by calculating the two-dimensional (2D) ensemble-averaged mean squared displacement (MSD, $\langle r^2(t) \rangle$) as a function of lag time t . The corresponding function for 2D Brownian motion,

$$\langle r^2(t) \rangle = 4Dt \quad (\text{Eq. 4-1})$$

was used to fit the data.

4.3.3.2 Péclet number – To account for the significance of the observed lateral diffusion during membrane transport, we used the dimensionless Péclet number (Pe) to compare the behavior of different size tracer particles on an equal basis.^{36, 37} Péclet numbers were calculated with the following equation:

$$Pe = \frac{Lu}{D} \quad (\text{Eq. 4-2})$$

where L is the characteristic length of the porous medium (the nominal membrane pore size of 0.65 μm was used), u is the local velocity of tracer particles and D is the corresponding diffusion coefficient of tracer particles in bulk solvent.³⁸ The syringe pump flow rate was varied in order to control the Péclet number over the desired range.

4.3.3.3 Tortuosity – In order to understand both local and global properties of membrane, local tortuosity and global tortuosity were calculated, respectively. To calculate mean local tortuosity $\langle\tau_L\rangle$, each trajectory was divided into sub-trajectories with equal durations of 10 time steps. For each sub-trajectory, partial tortuosity τ_s was calculated by

$$\tau_s = L_s/C_s \quad (\text{Eq. 4-3})$$

where L_s is the contour length and C_s is the end-to-end distance of the sub-trajectory. For each experimental condition, the mean local tortuosity $\langle\tau_L\rangle$ was the average of all sub-trajectory tortuosities sampled in the field of view using the equation

$$\langle\tau_L\rangle = \sum \tau_s/s \quad (\text{Eq. 4-4})$$

The local tortuosity values provided spatial information about membranes on length scales of approximately 10-100 times the characteristic pore size, which are highly relevant to particle transport and retention in membranes. With tens of thousands of sub-trajectories for each experimental condition, we successfully generated statistically significant probability distributions of local tortuosity.

As a complementary approach, we calculated the apparent global tortuosity τ_G which considered each measured trajectory to be a fragment of a complete pathway through the

membrane (the beginning and end of each fragment was determined by motion into and out of the focal plane of the microscope). τ_G was calculated by the sum of all contour lengths divided by the sum of all displacements projected in the global flow direction,

$$\tau_G = \frac{\sum L_n}{\sum C_{n,p}} \quad (\text{Eq. 4-5})$$

where L_n and $C_{n,p}$ are the contour length and the projection of the displacement in the global flow direction, respectively, for the n th trajectory. Global tortuosity involves length scales more than 1,000 times larger than the characteristic pore size. Compared to local tortuosity, it provides only a single average value, and heavily depends on trajectory segments whose net direction is lateral to the global flow direction. However, this metric does contain information about the overall flow directions of trajectories (i.e. it accounts for the fact that some trajectory fragments involved sideways, or even backwards, motion).

In order to maintain consistency in trajectory resolution for different flow rates, we adjusted the sampling of data points (in trajectories) based on mean particle velocity. Specifically, the same number of observations were sampled over a given distance traveled for particles with different velocities. This approach eliminated a potential source of bias by maintaining approximately equal spatial resolution for particles under different flow conditions.

4.3.3.4 Normalized residence time distributions – In studies of water flow through model geological formations, Berkowitz and coworkers pioneered statistical analyses that are appropriate for the characterization of anomalous and highly heterogeneous flow behavior, and these methods guided our approach here.^{8, 9} In particular, since our analysis of tortuosity indicated the presence of complex and heterogeneous pathways, we speculated that the local

particle residence times likely exhibited similarly heterogeneous behavior. To characterize this, we calculated histograms of normalized residence times by dividing each field of view into small bins ($1.56 \times 1.56 \mu\text{m}^2$). All trajectories passing through a given bin were identified and a mean residence time was calculated for each bin.⁹ These residence times were then normalized by the average residence time for all bins. For each experimental condition, a histogram was generated from these normalized mean residence times.

4.4 RESULTS AND DISCUSSION

4.4.1 Conventional Measurements of Apparent Tortuosity under Stagnant Conditions

One conventional, but indirect, method of measuring tortuosity involves a comparison of the apparent diffusion coefficient within the porous membrane (D_m), under stagnant conditions, to the diffusion coefficient in bulk solvent (D_b), using the expression $\tau_D = \sqrt{D_b/D_m}$.¹⁴ **Figure 4-2** shows MSD versus lag-time data for 40 nm and 200 nm tracer particles in bulk solvent and in the PVDF membrane, calculated from particle trajectories measured under stagnant conditions. As expected, the diffusion was slower for the larger particles compared to smaller particles, which was consistent with the Stokes – Einstein relation, which predicts that diffusion coefficients are inversely related to hydrodynamic radii of particles.³⁹ Meanwhile, for tracer particles of both sizes, diffusion was lower within the void space of the membrane than in unconfined bulk solution of the same liquid.^{26, 27} This effect was related to the tortuosity of membrane, whereby particles had to follow meandering pathways within the membrane therefore

traverse a greater length along the pathway in order to travel a certain Euclidean distance; while in bulk solvent, particles were able to explore the vicinity faster without any hindrance, and exhibited higher diffusion coefficients.^{10, 14} Using the diffusion coefficients calculated by fitting these MSD data to a linear model, τ_D for both tracer particles were determined to be 2.2 ± 0.1 (see **Table C-1** in Appendix C for fitting parameters). Obviously, this approach provides only an approximate average value for the structural tortuosity under stagnant conditions, but does not account for any effects that may depend on operating conditions.^{10, 14, 16, 17, 19} Nevertheless, it provides a useful baseline to which more detailed measurements can be compared.

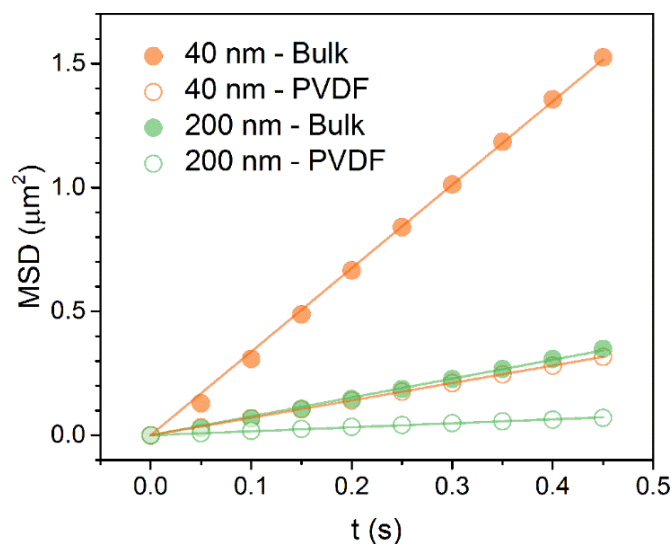


Figure 4-2. Mean squared displacements vs. time plots for 40 nm (orange) and 200 nm (green) nanoparticles diffusing in un-confined bulk solvent (filled symbols) and in PVDF membranes (open symbols). Solid lines represent linear fits to the equation $MSD = 4Dt$ (see **Table C-1** in Appendix C for fitting parameters and calculated absolute diffusion coefficients).

4.4.2 Tortuosity of Nanoparticle Trajectories Depends on Pe and Tracer Particle Size

To study the functional tortuosity of membranes under relevant operating conditions, we tracked individual tracer nanoparticles of different sizes under various flow conditions, and found that instead of being a simple structural material property, the effective membrane tortuosity was actually a functional property, which depended on both the flow conditions and the tracer size.

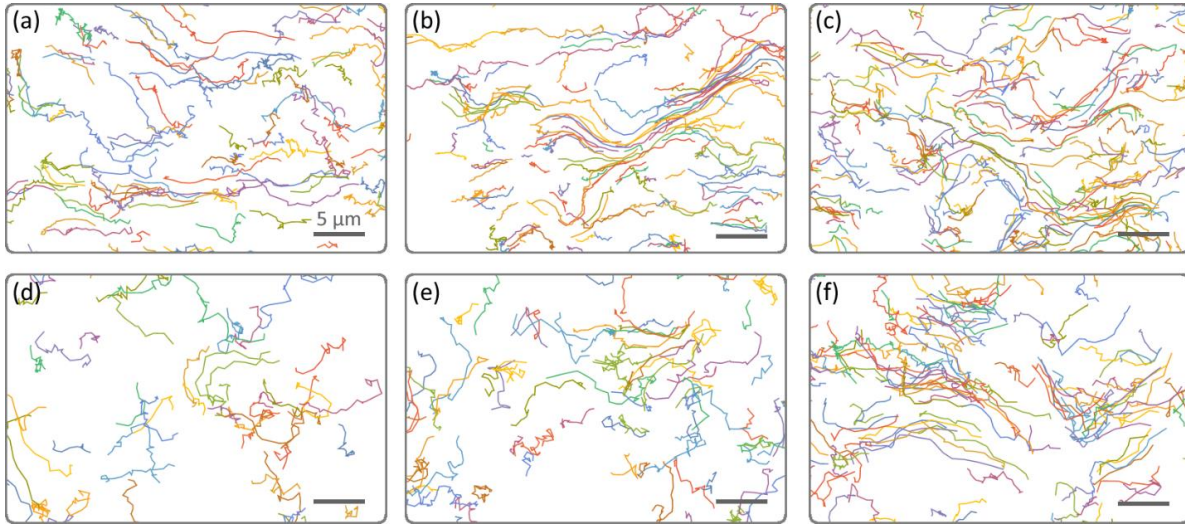


Figure 4-3. Trajectory maps (in different fields of view) obtained with 40 nm tracer particles (panels a-c) and 200 nm tracer particles (panels d-f) at varying Pe . $Pe = 3.3 \pm 0.3$, 5.3 ± 0.1 , and 6.7 ± 0.2 for panels a, b, and c, respectively. $Pe = 3.2 \pm 0.2$, 4.9 ± 0.2 , and 6.3 ± 0.2 for panels d, e, and f, respectively. Tracer particles flowed from the left to the right in these maps. Scale bar = 5 μm . The trajectory colors are arbitrary for the sake of visibility.

To visualize pathways under different experimental conditions, trajectory maps were constructed by overlaying trajectories obtained in representative experiments for 40 nm tracer particles (**Figures 4-3 a–c**) and 200 nm tracer particles (**Figure 4-3 d–f**) at various Péclet numbers (Pe) in PVDF membrane samples. As described above, we used Pe (the ratio of advection to diffusion) as the basis for comparison for tracer particles in different sizes, since the difference in diffusive mobility clearly had a significant impact on the resulting pathways through the membrane.^{36, 37} Interestingly, the observed pathways in these maps appeared to be sparse and heterogeneous, with some regions traversed by multiple particles, and others never sampled. The observation of regions through which no particles passed was possibly caused by a combination of flow restrictions/geometry and sparse sampling. However, since multiple trajectories were generally sampled in occupied regions, we believe that the apparent void spaces were most likely caused by flow restrictions and/or pathway geometry. For both particle sizes, the sampled pathways became less tortuous with increasing Pe . Additionally, when compared at similar Pe , the pathways followed by the larger tracer particles were systematically more tortuous than pathways followed by the smaller particles. **Figure 4-4** shows the values of mean local tortuosity $\langle\tau_L\rangle$ (**Figure 4-4a**) and global tortuosity τ_G (**Figure 4-4b**) for the two tracer particles as a function of Pe . Mean tortuosity values calculated in both ways exhibited the same trends. For the 40 nm tracers, $\langle\tau_L\rangle$ decreased systematically from 2.4 ± 0.2 to 1.8 ± 0.1 while τ_G decreased from 2.0 ± 0.2 to 1.6 ± 0.1 as Pe increased from 3.3 ± 0.3 to 6.7 ± 0.2 . $\langle\tau_L\rangle$ and τ_G measured with the 200 nm tracer were systematically higher in a similar Pe range. In particular, for 200 nm particles, $\langle\tau_L\rangle$ decreased from 3.0 ± 0.1 to 2.4 ± 0.1 and τ_G decreased from 4.6 ± 0.3 to 3.1 ± 0.2 as Pe increased from 3.2 ± 0.3 to 6.3 ± 0.2 . Again, these quantitative values explicitly demonstrated that the tortuosity relevant to nanoparticle transport was a functional property that

depended on operating conditions. We hypothesize that the decrease of tortuosity with increasing Pe may be related to the fact that particles flowed more deterministically in the flow direction at higher Pe due to reduced diffusive exploration of alternative pathways.^{6, 36, 40, 41} The increase of apparent tortuosity for larger tracer particles may be related to the fact that larger particles were more likely to be forced into alternative pathways due to an inability to pass through smaller constrictions.^{36, 42-44} These hypotheses will be tested below by direct analysis of local retention times.

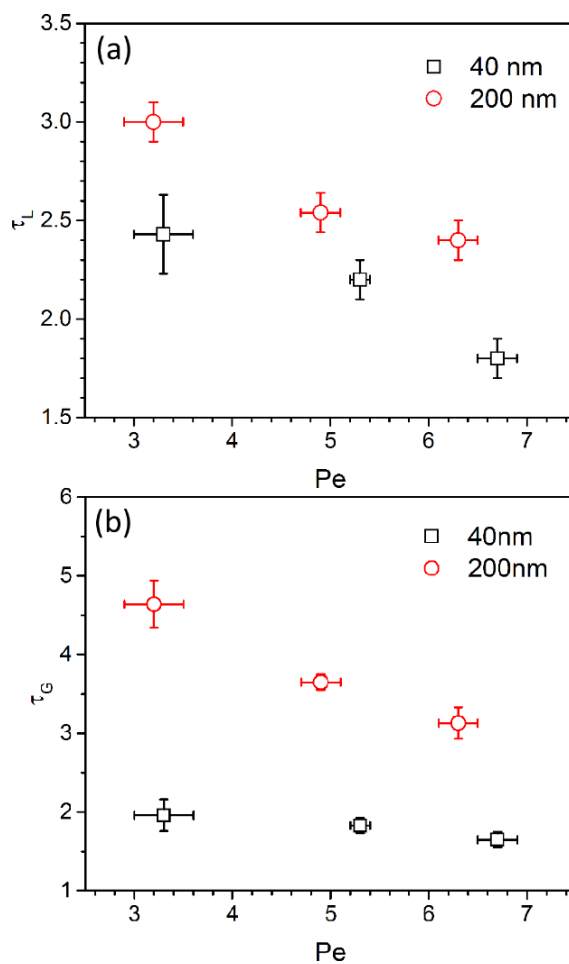


Figure 4-4. (a) Apparent mean local tortuosity (τ_L) and (b) global tortuosity τ_G for 40 nm and 200 nm tracer particles at increasing Pe . Error bars were calculated as the standard error of measurements from multiple independent experiments.

In addition to the 2D tracking results, we also performed 3D particle tracking experiments in order to directly measure the motion of particles in the z direction.^{34, 35} As described above, our choice to focus on particles that exhibited long in-focus trajectory segments, led us to exclude particles whose trajectories included large excursions in the z -direction. This was borne out by the 3D tracking results, which showed that for the sampled trajectories that remained in the focal plane for relatively long times, fluctuations in the z direction were minor, and therefore the resulting 3D tortuosity values were nearly identical to 2D tortuosity values (see **Figure C-3** in Appendix C for more details).³⁶ Since the membrane material was isotropic, it is expected that these trajectories and tortuosity values represented an unbiased sample. We note that this would not necessarily be the case for anisotropic or asymmetric membranes.

4.4.3 Spatial Heterogeneity

Since each sub-trajectory provided a separate value of local tortuosity, we obtained detailed information about the distribution of local tortuosity values under various operating conditions, which provided insights into the structural heterogeneity of the membrane void space. **Figure 4-5** shows probability distributions of local tortuosity values for 40 nm tracer particles (**Figures 4-5a**) and 200 nm tracer particles (**Figures 4-5b**) in PVDF membranes. These distributions exhibited heavy tails (i.e. the tails of these distribution were not exponentially bounded), which were associated with the significant numbers of sub-trajectories that were highly tortuous (3–4 times greater than the mean tortuosity), illustrating the remarkable spatial heterogeneity and inherent complexity of the membrane.³² Notably, this spatial heterogeneity decreased with Pe for both tracer particles sizes, as the tails of distributions shifted significantly

to the left. When comparing distributions for different size particles at similar values of Pe , heavier tails were observed for the larger particle, indicating increased spatial heterogeneity associated with the trajectories of larger tracer particles.

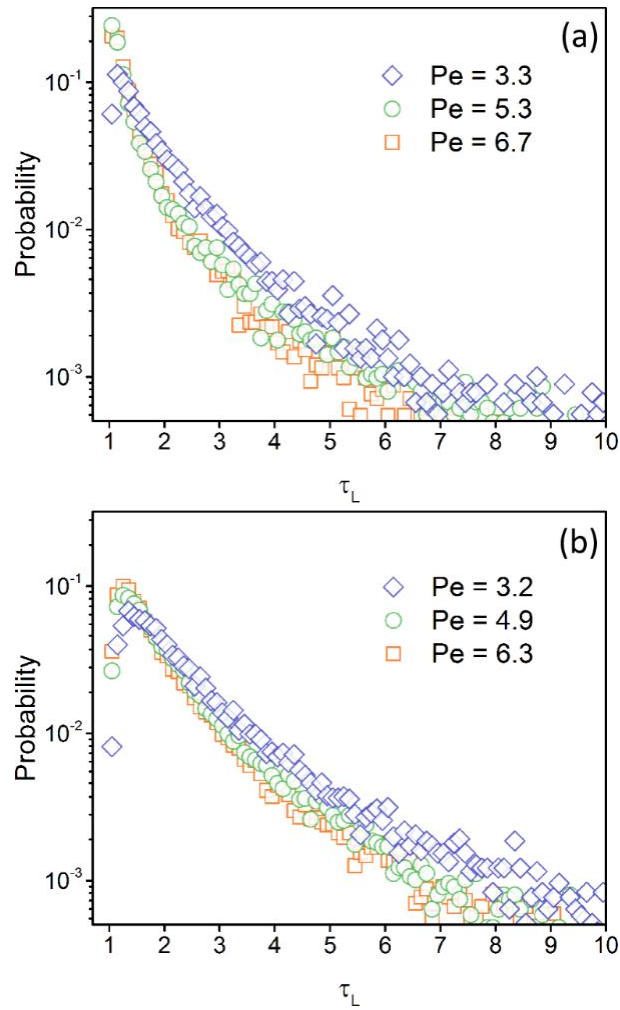


Figure 4-5. Probability distributions of local tortuosity τ_L for (a) 40 nm particle trajectories and (b) 200 nm particle trajectories at various Pe .

4.4.4 Temporal Heterogeneity

Tortuosity provides quantitative information about trajectories and pathways that is purely structural and geometrical, and ignores the dynamic information that is also obtained in the single-particle tracking experiments. For example, the instantaneous velocity of particles within a given membrane was highly heterogeneous, both between different trajectories and even within a given trajectory. To quantitatively characterize this information, we investigated the local residence times of tracer particles within the membrane under different operating conditions, which provided information about the temporal heterogeneity of particle transport. Specifically, we calculated normalized residence time distributions (as described in the experimental methodology section) for tracer particles of two different sizes at different Pe . **Figure 4-6** shows a representative heat-map of residence times for 200 nm particles flowing through a membrane at $Pe = 3.2$. The heterogeneity of residence times is readily visible, with most of the regions exhibiting short residence times and a smaller subset of highly retaining regions with long residence times. Particles that adsorbed to the pore walls were eliminated in the analysis and therefore did not influence the residence times.

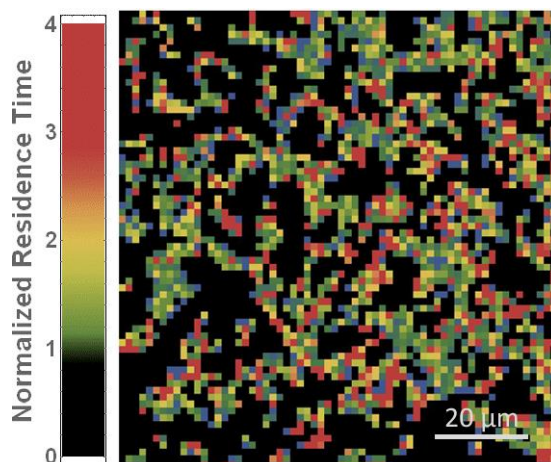


Figure 4-6. Representative heat map of normalized residence times for 200 nm tracer particles in a PVDF membrane at $Pe = 3.2$. Temporal heterogeneity (indicated by different colors) is visible in the heat map.

Figure 4-7 shows histograms of normalized residence times in each spatial location (i.e., “bin”) for 40 nm tracer particles (**Figures 4-7 a–c**) and 200 nm tracer particles (**Figures 4-7 d–f**) as a function of Pe . Narrow distributions with small standard deviation values would be expected if particles experienced uniform flow within the membranes. In contrast, the actual distributions were highly asymmetric (with skewness values of ~ 3) with heavy tails caused by a substantial fraction of local regions with anomalously long residence times.⁹ The temporal heterogeneity was quantified by calculating the standard deviations of these distributions, where larger standard deviation values were associated with greater temporal heterogeneity. The calculated standard deviation values are annotated on the graphs in **Figure 4-7** (see **Table C-2** in Appendix C for calculated standard deviation values, including uncertainties, for replicate experiments). Interestingly, the same overall trends were observed for temporal heterogeneity as for spatial heterogeneity as a function of Pe and tracer particle size; i.e., the standard deviation values decreased with increasing Pe , and increased with increasing particle size at similar Pe values.

Specifically, as Pe increased from ~ 3 to above 6, the calculated standard deviation value decreased from 0.90 to 0.65 for the 40 nm tracer and from 0.93 to 0.77 for the 200 nm tracer. Therefore, the temporal heterogeneity decreased with increasing Pe , and increased with increasing particle size at similar Pe values.

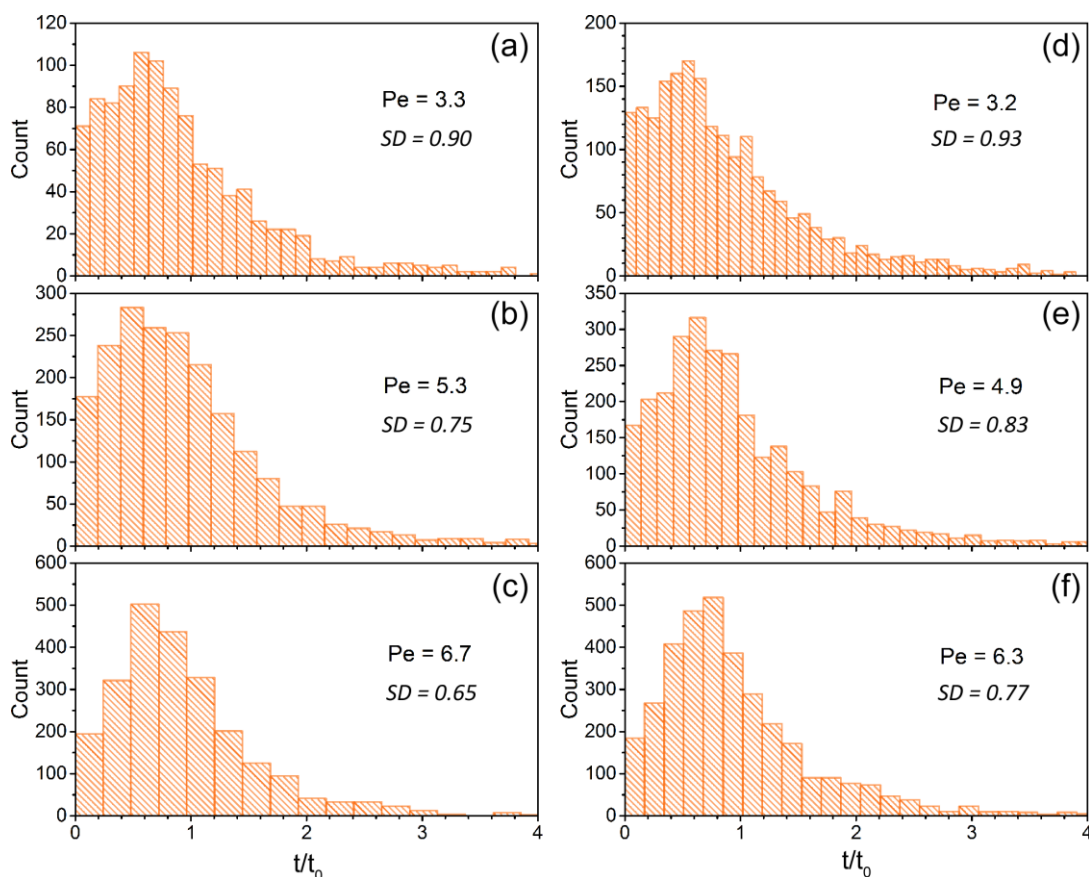


Figure 4-7. Histograms of normalized residence times per bin for (a–c) 40 nm tracer particles and (d–f) 200 nm tracer particles in PVDF membrane at various Pe (see **Table C-2** in Appendix C for standard deviation values and uncertainties calculated for all six histograms).

4.4.5 Correlation between Tortuosity and Retention

We emphasize that the correlation in the trends associated with spatial and temporal heterogeneity is a non-trivial result since the data associated with the tortuosity and residence time distributions are completely independent. Specifically, the tortuosity distributions are calculated on a per-trajectory basis, are based solely on the shape of trajectories, and contain no information about the local particle velocity, while the residence time distributions are associated with the average velocity of multiple trajectories that pass through a given spatial location. Therefore, since the same qualitative trends were observed in both spatial and temporal heterogeneity, we hypothesized that there might be a direct mechanistic correlation connecting them. Specifically, we hypothesized a scenario in which localized highly-confining regions in the membrane lead to anomalously long local residence times and also divert particles passing through those regions into highly meandering trajectories.^{9, 26, 45-47} To test this hypothesis, we correlated tortuosity to retention in two distinct ways.

In one approach, we identified locations in the membrane associated with anomalously long residence times. Specifically, bins with a residence time of >2 times the average residence time were defined as “long-retaining” regions. Consequently, trajectories that passed through any of those long-retaining regions at least once were assigned to the long-retaining group, while the other trajectories were assigned to the short-retaining group (see **Figure C-4** in Appendix C for more details). $\langle\tau_L\rangle$ calculated for “long-retaining” trajectories and “short-retaining” trajectories are shown for 40 nm (**Figure 4-8a**) and 200 nm tracer particles (**Figure 4-8b**) as a function of Pe . Interestingly, for both particle sizes, the trajectories that passed through long-

retaining regions were systematically more tortuous than trajectories that did not pass through long-retaining regions, suggesting a direct correlation between temporal and spatial heterogeneity, as we hypothesized.

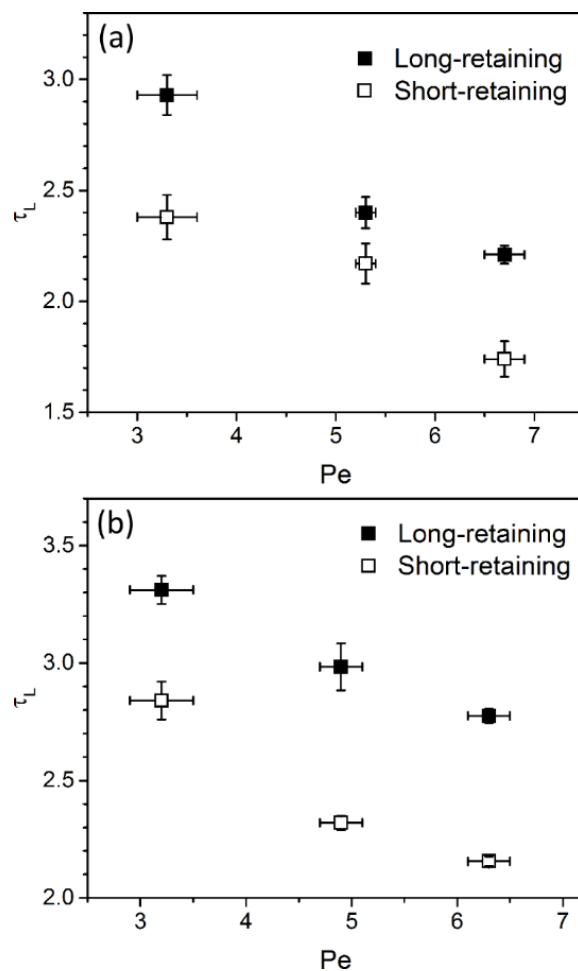


Figure 4-8. Local tortuosity τ_L for trajectories of (a) 40 nm tracer particles and (b) 200 nm tracer particles at increasing Pe . Filled symbols represent τ_L for trajectories that passed through long-retaining region(s) and open symbols represent τ_L for trajectories that flowed only through short-retaining region(s).

As a complementary approach, we also calculated the mean residence time per length (t_i , i.e. the mean residence time in each bin) for each trajectory, and correlated t_i to the tortuosity for each trajectory (τ_i). **Figure 4-9** shows heat maps correlating retention versus tortuosity for the 40 nm (**Figures 4-9 a–c**) and 200 nm tracer particles (**Figures 4-9 d–f**) under varying experimental conditions. For each trajectory, the mean residence time in each bin (vertical axis) and the logarithm of tortuosity (horizontal axis) were calculated and plotted, respectively. Heat maps were then generated based on the density of data points. As shown in **Figure 4-9**, under different experimental conditions, the majority of data points fell into diagonal regions, suggesting that trajectories with higher tortuosity had longer retention time per length as well. This trend was significantly more dramatic for the 200nm particles than for 40nm particles. By comparison, the correlation of tortuosity and retention was much weaker for trajectories obtained in bulk solvent (see **Figure C-5** and **Table C-3** in Appendix C for heat maps and more discussion), consistent with the more homogeneous Brownian motion expected for unconfined particles in solution.

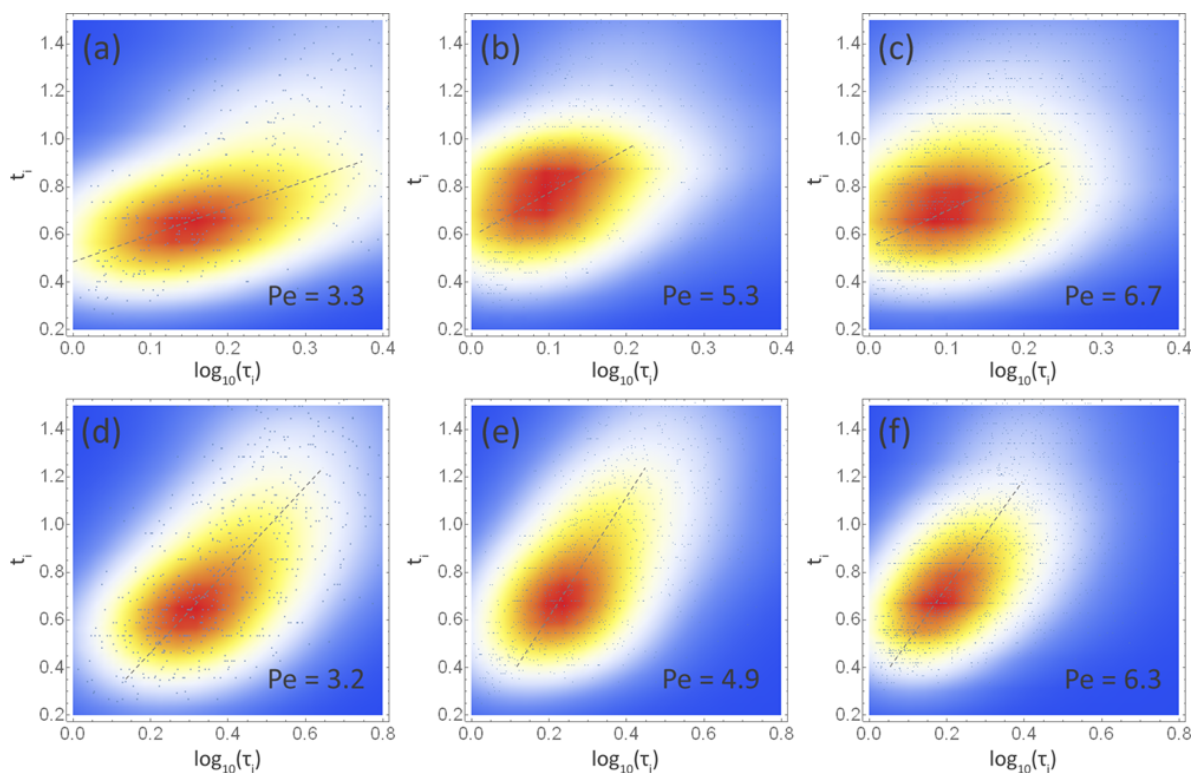


Figure 4-9. Heat maps showing correlations of normalized mean residence time per length (t_i) vs. the logarithm of tortuosity for each trajectory. Panels (a-c) show correlations for 40 nm tracer particles and panels (d-f) show correlations for 200 nm tracer particles at different Pe . Dashed lines are guides to the eye.

Both approaches described above support the hypothetical connection between tortuosity and retention. Specifically, we found that particles passing through highly-retaining regions exhibited more tortuous trajectories, and also that more tortuous trajectories exhibited longer residence times per length. Furthermore, as previously discussed, both spatial and temporal heterogeneity decreased with increasing Pe and increased with increasing particle size. At higher values of Pe , trajectories were presumably less tortuous because there was less diffusive

exploration of secondary pathways, and particles had greater momentum to break through confining regions; so trajectories appeared to be less spatially and temporally heterogeneous;^{9, 36} We speculate that the heavy tails in the tortuosity distributions were largely due to anomalously meandering trajectories that resulted when particles visit highly-retaining regions and were forced into a less-direct pathway. While this trend may seem counterintuitive for those familiar with size-exclusion chromatography, we emphasize that all particles used in these experiments were significantly smaller than the nominal pore size, so the situation is subtly different. Moreover, although smaller particles might experience a slightly larger subset of pathways, the small particles were dramatically less likely to be affected by highly-retaining regions. In comparison, larger particles (with diameters 4-5 times larger than the smaller particles on average) were more likely to experience the relative rare highly-retaining regions, since constrictions that trapped large particles may not trap small particles, thus the trajectories of large particles were more spatially and temporally heterogeneous.^{26, 27}

We note that an alternative explanation for the higher temporal heterogeneity of the 200 nm tracer particles could be related to the stronger van der Waals (vdW) interactions expected between the larger particles and the interior surface of membrane pores (vdW forces increase linearly with particle size in the Derjaguin approximation),⁴⁸ which could influence the retention times of particles in the membrane. However, the index-matched system resulted in a very small effective Hamaker constant (related by Lifshitz theory to the difference between the dielectric constants of the materials and the surrounding medium) and therefore the corresponding vdW interactions were relatively weak in general.^{48, 49} In fact, contrary to the trend expected from the strength of vdW interactions, we observed fewer adsorption events for the 200 nm particles compared to the 40 nm particles, presumably due to the fact that larger particles experienced

greater shear force in flow and were dislodged more readily from the interior surfaces of the membrane.⁵⁰ As a result, we believe that differences in the vdW interactions for the two particle sizes did not determine the trends in spatio-temporal heterogeneity.

4.5 CONCLUSIONS

A high-throughput single-particle tracking approach was employed to explicitly characterize both the spatial heterogeneity of observed pathways and temporal heterogeneity of tracer particle retention in porous filtration membranes. We observed the dependence of tortuosity on operating conditions, i.e. the apparent tortuosity decreased with Péclet number (Pe) and increased with tracer particle size. With thousands of individual trajectories identified in different membrane locations, we also resolved the spatial heterogeneity and temporal heterogeneity of particle trajectories through the membranes, which exhibited similar trends with Pe and tracer size, and were correlated with each other. The correlation of tortuosity and retention reinforced the hypothetical scenario that anomalous highly confining regions were instrumental in causing more meandering trajectories and longer residence times. Moreover, the existence of those confining regions had more pronounced effects on larger particles and at lower Pe . We suggest that the reduction of these highly confining regions may represent an important practical goal for the design and synthesis of porous materials, especially filtration membranes.

Importantly, single-particle tracking techniques enabled measurements of tortuosity of porous materials under various operating conditions. This comprehensive picture of tortuosity has the potential to advance the understanding of complex mass transport in porous media, and at the same time, the resulting tortuosity measurements can provide more accurate reference values

to design and synthesize porous materials in rational ways.⁵¹⁻⁵⁴ Finally, this accurate measurement of tortuosity will permit valid correlations with other properties of interest, such as the membrane fouling during filtration processes.⁵⁵⁻⁵⁸

4.6 REFERENCES

1. van Reis, R.; Zydney, A., Bioprocess membrane technology. *J. Membr. Sci.* **2007**, 297 (1), 16-50.
2. Shannon, M. A.; Bohn, P. W.; Elimelech, M.; Georgiadis, J. G.; Mariñas, B. J.; Mayes, A. M., Science and technology for water purification in the coming decades. *Nature* **2008**, 452 (7185), 301-310.
3. McDowell-Boyer, L. M.; Hunt, J. R.; Sitar, N., Particle transport through porous media. *Water Resour. Res.* **1986**, 22 (13), 1901-1921.
4. O'Melia, C. R., Particles, pretreatment, and performance in water filtration. *J. Environ. Eng.* **1985**, 111 (6), 874-890.
5. Parlett, C. M.; Wilson, K.; Lee, A. F., Hierarchical porous materials: catalytic applications. *Chem. Soc. Rev.* **2013**, 42 (9), 3876-3893.
6. Van Deemter, J. J.; Zuiderweg, F.; Klinkenberg, A. v., Longitudinal diffusion and resistance to mass transfer as causes of nonideality in chromatography. *Chem. Eng. Sci.* **1956**, 5 (6), 271-289.
7. Minchinton, A. I.; Tannock, I. F., Drug penetration in solid tumours. *Nat. rev., Cancer* **2006**, 6 (8), 583-592.
8. Dentz, M.; Cortis, A.; Scher, H.; Berkowitz, B., Time behavior of solute transport in heterogeneous media: transition from anomalous to normal transport. *Adv. Water Resour.* **2004**, 27 (2), 155-173.
9. Edery, Y.; Guadagnini, A.; Scher, H.; Berkowitz, B., Origins of anomalous transport in heterogeneous media: Structural and dynamic controls. *Water Resour. Res.* **2014**, 50 (2), 1490-1505.

10. Ghanbarian, B.; Hunt, A. G.; Ewing, R. P.; Sahimi, M., Tortuosity in Porous Media: A Critical Review. *Soil Sci. Soc. Am. J.* **2013**, 77 (5), 1461-1477.
11. David, C., Geometry of flow paths for fluid transport in rocks. *J. Geophys. Res.: Solid Earth* **1993**, 98 (B7), 12267-12278.
12. Koponen, A.; Kataja, M.; Timonen, J., Tortuous flow in porous media. *Phys. Rev. E* **1996**, 54 (1), 406-410.
13. Lee, Y.; Andrade Jr, J. S.; Buldyrev, S. V.; Dokholyan, N. V.; Havlin, S.; King, P. R.; Paul, G.; Stanley, H. E., Traveling time and traveling length in critical percolation clusters. *Phys. Rev. E* **1999**, 60 (3), 3425.
14. Nicolay, K.; Braun, K. P.; Graaf, R. A. d.; Dijkhuizen, R. M.; Kruiskamp, M. J., Diffusion NMR spectroscopy. *NMR Biomed.* **2001**, 14 (2), 94-111.
15. DuBeshter, T.; Sinha, P. K.; Sakars, A.; Fly, G. W.; Jorne, J., Measurement of tortuosity and porosity of porous battery electrodes. *J. Electrochem. Soc.* **2014**, 161 (4), A599-A605.
16. Landesfeind, J.; Hattendorff, J.; Ehrl, A.; Wall, W. A.; Gasteiger, H. A., Tortuosity determination of battery electrodes and separators by impedance spectroscopy. *J. Electrochem. Soc.* **2016**, 163 (7), A1373-A1387.
17. Vallabh, R.; Banks-Lee, P.; Seyam, A.-F., New approach for determining tortuosity in fibrous porous media. *J. Eng. Fiber Fabr.* **2010**, 5 (3), 7-19.
18. Suman, R.; Ruth, D., Formation factor and tortuosity of homogeneous porous media. *Transport Porous Med.* **1993**, 12 (2), 185-206.
19. Vervoort, R.; Cattle, S., Linking hydraulic conductivity and tortuosity parameters to pore space geometry and pore-size distribution. *J. Hydrol.* **2003**, 272 (1), 36-49.
20. Shen, L.; Chen, Z., Critical review of the impact of tortuosity on diffusion. *Chem. Eng. Sci.* **2007**, 62 (14), 3748-3755.
21. Bhatia, S., Directional autocorrelation and the diffusional tortuosity of capillary porous media. *J. Catal.* **1985**, 93 (1), 192-196.

22. Dykhuizen, R. C.; Casey, W. H., An analysis of solute diffusion in rocks. *Geochim. Cosmochim. Acta* **1989**, *53* (11), 2797-2805.
23. Berg, C. F.; Held, R., Fundamental transport property relations in porous media incorporating detailed pore structure description. *Transport Porous Med.* **2016**, *112* (2), 467-487.
24. Ghanbarian, B.; Hunt, A. G.; Sahimi, M.; Ewing, R. P.; Skinner, T. E., Percolation theory generates a physically based description of tortuosity in saturated and unsaturated porous media. *Soil Sci. Soc. Am. J.* **2013**, *77* (6), 1920-1929.
25. Meyer, D. W.; Bijeljic, B., Pore-scale dispersion: Bridging the gap between microscopic pore structure and the emerging macroscopic transport behavior. *Phys. Rev. E* **2016**, *94* (1), 013107.
26. Skaug, M. J.; Schwartz, D. K., Tracking nanoparticle diffusion in porous filtration media. *Ind. Eng. Chem. Res.* **2015**, *54* (16), 4414-4419.
27. Skaug, M. J.; Wang, L.; Ding, Y.; Schwartz, D. K., Hindered nanoparticle diffusion and void accessibility in a three-dimensional porous medium. *ACS Nano* **2015**, *9* (2), 2148-2156.
28. Jiang, L.; Granick, S., Real-space, in situ maps of hydrogel pores. *ACS Nano* **2016**, *11* (1), 204-212.
29. Wiederseiner, S.; Andreini, N.; Epely-Chauvin, G.; Ancey, C., Refractive-index and density matching in concentrated particle suspensions: a review. *Exp. Fluids* **2011**, *50* (5), 1183-1206.
30. White, F. M.; Corfield, I., *Viscous fluid flow*. McGraw-Hill Higher Education Boston: 2006; Vol. 3.
31. Honciuc, A.; Harant, A. W.; Schwartz, D. K., Single-molecule observations of surfactant diffusion at the solution– solid interface. *Langmuir* **2008**, *24* (13), 6562-6566.
32. Cai, Y.; Schwartz, D. K., Influence of protein surface coverage on anomalously strong adsorption sites. *ACS Appl. Mater. Interfaces* **2015**, *8* (1), 511-520.
33. Cai, Y.; Shashikanth, N.; Leckband, D. E.; Schwartz, D. K., Cadherin diffusion in supported lipid bilayers exhibits calcium-dependent dynamic heterogeneity. *Biophys. J.* **2016**, *111* (12), 2658-2665.
34. Pavani, S. R. P.; Thompson, M. A.; Biteen, J. S.; Lord, S. J.; Liu, N.; Twieg, R. J.; Piestun, R.; Moerner, W., Three-dimensional, single-molecule fluorescence imaging beyond the

diffraction limit by using a double-helix point spread function. *Proc. Natl. Acad. Sci.* **2009**, *106* (9), 2995-2999.

35. Thompson, M. A.; Lew, M. D.; Badieirostami, M.; Moerner, W., Localizing and tracking single nanoscale emitters in three dimensions with high spatiotemporal resolution using a double-helix point spread function. *Nano Lett.* **2009**, *10* (1), 211-218.

36. He, K.; Retterer, S. T.; Srijanto, B. R.; Conrad, J. C.; Krishnamoorti, R., Transport and dispersion of nanoparticles in periodic nanopost arrays. *ACS Nano* **2014**, *8* (5), 4221-4227.

37. Datta, S. S.; Chiang, H.; Ramakrishnan, T.; Weitz, D. A., Spatial fluctuations of fluid velocities in flow through a three-dimensional porous medium. *Phys. Rev. Lett.* **2013**, *111* (6), 064501.

38. Tufenkji, N.; Elimelech, M., Correlation equation for predicting single-collector efficiency in physicochemical filtration in saturated porous media. *Environ. Sci. Technol.* **2004**, *38* (2), 529-536.

39. Edward, J. T., Molecular volumes and the Stokes-Einstein equation. *J. Chem. Educ.* **1970**, *47* (4), 261.

40. Qian, H.; Sheetz, M. P.; Elson, E. L., Single particle tracking. Analysis of diffusion and flow in two-dimensional systems. *Biophys. J.* **1991**, *60* (4), 910-921.

41. Eckstein, E. C.; Bailey, D. G.; Shapiro, A. H., Self-diffusion of particles in shear flow of a suspension. *J. Fluid Mech.* **1977**, *79* (1), 191-208.

42. Stevenson, D., Flow and filtration through granular media—The effect of grain and particle size dispersion. *Water Res.* **1997**, *31* (2), 310-322.

43. Cho, J.; Amy, G.; Pellegrino, J., Membrane filtration of natural organic matter: factors and mechanisms affecting rejection and flux decline with charged ultrafiltration (UF) membrane. *J. Membr. Sci.* **2000**, *164* (1), 89-110.

44. Kusumi, A.; Sako, Y.; Yamamoto, M., Confined lateral diffusion of membrane receptors as studied by single particle tracking (nanovid microscopy). Effects of calcium-induced differentiation in cultured epithelial cells. *Biophys. J.* **1993**, *65* (5), 2021-2040.

45. Levitz, P., Off-lattice reconstruction of porous media: critical evaluation, geometrical confinement and molecular transport. *Adv. Colloid Interface Sci.* **1998**, *76*, 71-106.

46. Jacob, J. D. C.; He, K.; Retterer, S. T.; Krishnamoorti, R.; Conrad, J. C., Diffusive dynamics of nanoparticles in ultra-confined media. *Soft Matter* **2015**, *11* (38), 7515-7524.
47. He, K.; Babaye Khorasani, F.; Retterer, S. T.; Thomas, D. K.; Conrad, J. C.; Krishnamoorti, R., Diffusive dynamics of nanoparticles in arrays of nanoposts. *ACS Nano* **2013**, *7* (6), 5122-5130.
48. Graf, K.; Kappl, M., *Physics and chemistry of interfaces*. John Wiley & Sons: 2006.
49. Milling, A.; Mulvaney, P.; Larson, I., Direct measurement of repulsive van der Waals interactions using an atomic force microscope. *J. Colloid Interface Sci.* **1996**, *180* (2), 460-465.
50. Janna, W. S., *Introduction to fluid mechanics*. CRC press: 2009.
51. Prasad, R.; Sirkar, K., Dispersion-free solvent extraction with microporous hollow-fiber modules. *AIChE J.* **1988**, *34* (2), 177-188.
52. Liu, Y.; Hu, E.; Khan, E. A.; Lai, Z., Synthesis and characterization of ZIF-69 membranes and separation for CO₂/CO mixture. *J. Membr. Sci.* **2010**, *353* (1), 36-40.
53. Wang, G.; Coppins, M.-O., Rational design of hierarchically structured porous catalysts for autothermal reforming of methane. *Chem. Eng. Sci.* **2010**, *65* (7), 2344-2351.
54. Viegas, R.; Rodriguez, M.; Luque, S.; Alvarez, J.; Coelho, I.; Crespo, J., Mass transfer correlations in membrane extraction: analysis of Wilson-plot methodology. *J. Membr. Sci.* **1998**, *145* (1), 129-142.
55. Chang, I.-S.; Le Clech, P.; Jefferson, B.; Judd, S., Membrane fouling in membrane bioreactors for wastewater treatment. *J. Environ. Eng.* **2002**, *128* (11), 1018-1029.
56. Guo, W.; Ngo, H.-H.; Li, J., A mini-review on membrane fouling. *Bioresour. technol.* **2012**, *122*, 27-34.
57. Henry, C.; Minier, J.-P.; Lefèvre, G., Towards a description of particulate fouling: From single particle deposition to clogging. *Adv. colloid interface sci.* **2012**, *185*, 34-76.

58. Meng, F.; Chae, S.-R.; Drews, A.; Kraume, M.; Shin, H.-S.; Yang, F., Recent advances in membrane bioreactors (MBRs): membrane fouling and membrane material. *Water Res.* **2009**, *43* (6), 1489-1512.

Chapter 5

Single-Nanoparticle Tracking Reveals Mechanisms of Membrane Fouling

Reproduced from Cai, Y. and Schwartz, D. K., *Journal of Membrane Science*, **2018**, 563, 888–895.

5.1 ABSTRACT

While membrane fouling has been studied for decades, it remains challenging to obtain direct information about the dominant mechanism of fouling in a specific scenario. Here, we employed a high-throughput particle-tracking approach, which enabled the visualization of particle transport in actual microfiltration membranes under flow conditions and provided direct evidence for distinct fouling mechanisms under different operating conditions. Our results suggest that the “stickiness” of particles can qualitatively change the dominant fouling mechanism. In particular, the evolutions of effective flux, particle velocity and pathway tortuosity were found to be systematically different under “sticking” vs “reduced-sticking” conditions in two different microfiltration membranes, composed of PVDF and PTFE, respectively. Under “sticking” conditions, fouling was rapid, and individual pathways were observed to disappear with the reduction of flux. However, the average particle velocity and the tortuosity of particle trajectories were unchanged throughout the fouling process, consistent with the complete blocking of random pathways. Conversely, under “reduced-sticking” conditions,

the average particle velocity decreased and the tortuosity of particle pathways increased systematically with fouling, consistent with the gradual narrowing of pathways causing increased resistance. The comprehensive information about particle dynamics in membranes achieved with this approach will assist design and optimization of reduced-fouling separation processes as well as advance the understanding of complex mass transport.

5.2 INTRODUCTION

Microfiltration is a type of separation process used to remove undesired contaminants in liquid formulations, and is commonly applied in bio-processing, water treatment, dairy processing and pharmaceutical purification.¹⁻¹⁰ Despite intensive efforts and significant improvements, membrane fouling remains an impediment for filtration technology since it can cause rapid declines in permeate flux and reduce the efficiency of separations, resulting in higher costs related to energy, operation time, and membrane maintenance/replacement in order to maintain productivity.¹¹⁻¹³ In recent decades, researchers have conducted extensive studies on membrane fouling and developed mathematical models to describe different fouling processes, including complete blocking, intermediate blocking, standard blocking and cake filtration.¹¹⁻¹⁵ The most common way to study fouling mechanism is to measure the permeate flux as a function of time, and then determine the most likely mechanism(s) by comparing experimental flux curves to mathematical models.^{14, 16-18} However, this approach clearly provides indirect and model-dependent information about fouling processes. Here we developed a complementary approach based on direct visualization of particle transport within filtration membranes under flow conditions, providing explicit evidence for distinct fouling mechanisms.¹⁹

It has been previously reported that the decrease of membrane permeability can be related to the binding of solutes to the membrane.^{15, 16} Here, we applied a particle tracking approach to study the effects of particle sticking on fouling mechanisms systematically. Specifically, we used fluorescent nanoparticles as foulants and traced the fouling processes in two model polymer microfiltration membranes. Conditions representing “sticking” and “reduced-sticking” environments were formulated in both membranes, and the behaviors of fluorescent tracer particles were directly imaged using epifluorescence microscopy under the two types of condition, respectively. Compared to conventional methods that measure ensemble-average information of permeate flux through membrane, the particle-tracking technique applied here enables the observation of individual particle motions during fouling processes and provides direct evidence for fouling mechanisms.^{19, 20} For example, decreased flux may be due to a reduction of open pathways, slower flow velocities, or a combination of the two. In typical macroscopic measurements, these effects cannot be distinguished, but particle tracking provides this information directly. Moreover, we explored the evolution of the functional membrane tortuosity as a function of fouling. The detailed information provided by this approach affords new insights into membrane fouling mechanisms as well as valuable reference data for the rational design of reduced-fouling separation processes.

5.3 EXPERIMENTAL METHODOLOGY

5.3.1 Materials and Sample Preparation

Durapore (PVDF) membrane filters and LCR (PTFE) membrane filters were purchased from MilliporeSigma. The Durapore (PVDF) membrane filters had a nominal pore size of 0.65

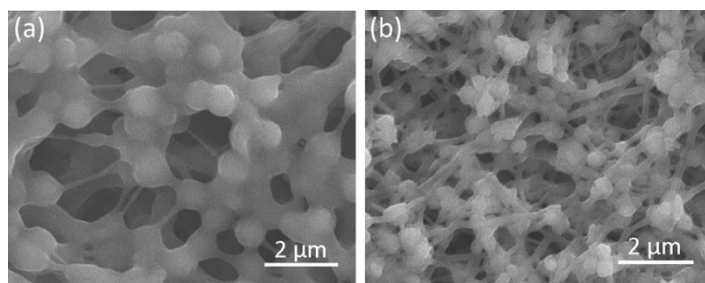


Figure 5-1. Scanning electron microscope (SEM) images of a (a) Durapore (PVDF) filtration membrane with nominal pore size of 0.65 μm and an (b) LCR (PTFE) filtration membrane with nominal pore size of 0.45 μm .

μm , a thickness of 125 μm and a porosity of 70% (**Figure 5-1a**). The LCR (PTFE) membrane filters had a nominal pore size of 0.45 μm , a thickness of 140 μm (maximum) and a porosity of 80% (**Figure 5-1b**). Both membranes were modified to be hydrophilic by the manufacturer. Membrane filters were cut into annuli and sealed in a flow cell for imaging as described previously.¹⁹ A schematic diagram describing the experimental setup is shown in **Figure 5-2**. Tracer particle solutions were introduced from the inlet and flowed radially outward through the annulus of the membrane being imaged. The mean direction of flow was nominally parallel to the focal plane within the flow cell. As discussed in previous work, with the depth of focus being relatively shallow ($\sim 3\mu\text{m}$), this approach emphasized trajectories that were extensive in the x - y plane but barely meandered in the z -direction.¹⁹ For experimental consistency, the focal plane was set to be 20 μm from the external surface of membrane in each experiment. FluoSpheres carboxylate-modified microspheres (Invitrogen) with nominal sizes of 0.04 μm (dark red fluorescent, 660/680) and 0.2 μm (orange fluorescent, 540/560) were used as tracer particles. The tracer particle concentration in solution was $\sim 3 \times 10^8$ particles/mL for single particle tracking experiments in PVDF membranes and $\sim 10^{10}$ particles/mL for experiments in PTFE membranes.

These concentrations were low enough to minimize particle-particle interactions and enable localization of individual particles in membrane. Hydrostatic pressure was used to drive flows through membranes and the pressure drop (~ 0.2 psi for experiments in PVDF membranes and ~ 0.3 psi for experiments in PTFE membranes) for each experiment was constant. The corresponding initial flux values were estimated using the initial velocity and membrane porosity, which was $\sim 10 \pm 1$ L/(h·m²) in PVDF membranes and $\sim 15 \pm 3$ L/(h·m²) in PTFE membranes.

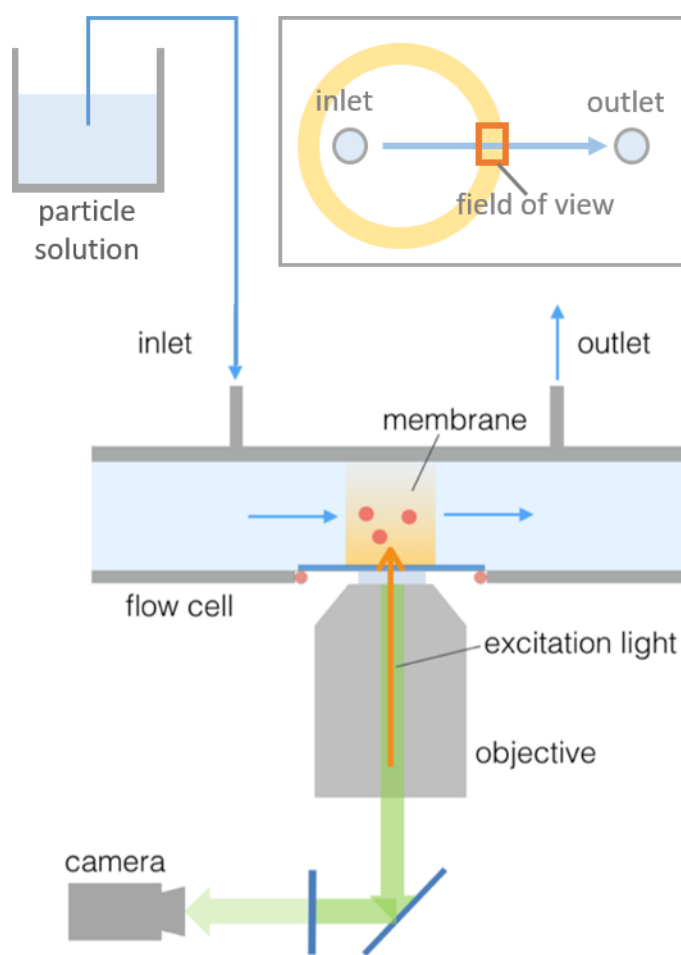


Figure 5-2. Schematic diagram showing the flow cell construction (with flow driven by hydrostatic pressure) and the imaging system (only the part of membrane being imaged is shown). Top right inset demonstrates the shape of membrane sample and the field of view being imaged.

Due to limitations of our current imaging capabilities, these flow rates were substantially lower than those employed in actual industrial filtration processes. While the initial velocity as well as initial flux values were similar under the same pressure drop, no systematic effects of initial flux on fouling behavior were observed in those experiments.

In order to minimize light scattering from the interior surfaces of membranes, index-matching liquids were formulated with alcohols and Triton X-100 for the two materials. Triton X-100 also functioned as a surfactant to reduce the immobilization of tracer particles. Index-matching liquids with different concentrations of surfactant were used to create conditions with desired particle “stickiness” as indicated in **Table 5-1**.

Table 5-1. Compositions of index-matching liquids and tracer particles used to formulate “reduced-sticking” and “sticking” conditions in PVDF and PTFE membranes.

Membrane	“Stickiness”	Tracer	Index-matching liquid composition
Durapore (PVDF) (n = 1.42)	reduced	200 nm	64% 2-propanol + 36% Triton X-100
	sticky	40 nm	64% 2-propanol + 36% Triton X-100
		200 nm	69% 2-propanol + 30% 2, 2'-thiodiethanol +1% Triton X-100
LCR (PTFE) (n=1.36)	reduced	40 nm	49% methanol + 50% 2-propanol +1% Triton X-100
	sticky	40 nm	49.8% methanol + 50% 2-propanol +0.2% Triton X-100

5.3.2 Fluorescence Microscopy and Single-Particle Tracking

All experiments were performed at 21 °C on a Nikon Ti-E epifluorescence microscope with a CFI Plan Apo Lambda 100× oil immersion objective and a 532/638 C-TIRF filter cube

(Chroma). A CMOS camera (Hamamatsu) was used to capture images with a pixel size of 0.13 μm and an acquisition time of 50 ms. Multiple movies (3000 frames per movie) were collected for each time period in every observation. Fluorescent tracer particles were illuminated by either a 640 nm diode-pumped solid state laser (CrystaLaser, for dark red fluorescence) or a 532 nm diode-pumped solid state laser (Cobolt AB, for orange fluorescence). Custom algorithms implemented in Mathematica were used to determine trajectories of individual particles as described previously.²¹⁻²³ All trajectories with residence times shorter than 0.5 s were excluded for the purpose of statistical analysis. Completely immobile trajectories resulting from fluorescent objects adsorbed to the interior surface of membrane were excluded from the analyses for effective flux (i.e. the quantity of liquid passing through the membrane), particle velocity and tortuosity distributions. Several thousand trajectories were analyzed for the initial time period of each fouling experiment, and the number of trajectories analyzed decreased gradually as a function of fouling.

5.3.3 Normalized Flux and Normalized Mean Particle Velocity

Under the assumption that the concentration of tracer particles was constant throughout each experiment, the effective normalized flux in the membrane (representing the quantity of liquid passing through the membrane) was calculated using the number of flowing objects appearing in the field of view within a certain period of time, normalized to the initial flux at the beginning of each fouling experiment. Similarly, the mean velocity of tracer particles was calculated for different time periods and normalized to the initial mean velocity for each experiment.

5.3.4 Tortuosity Distributions

Local tortuosity was calculated as described previously.¹⁹ Briefly, each trajectory was divided into sub-trajectories with equal durations of 10 time steps, and the local tortuosity for each sub-trajectory was calculated as the ratio of its contour length to its Euclidean end-to-end distance. For each experimental condition, a probability distribution was calculated using the accumulated local tortuosity values.

5.4 RESULTS AND DISCUSSIONS

5.4.1 Controlling the “Stickiness” of Tracer Particles in Membrane

Fluorescent nanoparticles were used as foulants and detailed fouling processes in PVDF and PTFE membranes were imaged using epifluorescence microscopy. Interestingly, we found that the “stickiness” of tracer particles (how readily they stuck to the interior surfaces of membranes or to other particles) in both membranes played a significant role in determining different regimes of fouling behaviors. Notably, under the non-aqueous conditions employed in these experiments (chosen to provide optical index matching), the particle–particle and particle–surface interactions were likely dominated by van der Waals forces. Based on our experimental observations, the sticking of particles strongly depended on two major factors: tracer particle size and the concentration of surfactant in solvent. We observed that larger tracer particles appeared to be less sticky to the pore walls, presumably because they experienced greater shear force in flow and were dislodged more easily from the interior surfaces of membrane.^{19, 24} Also, since

surfactant can passivate particle surfaces and the interior membrane surfaces, increasing the concentration of surfactant in solvent reduced the sticking of particles to surfaces as well as to other particles.²⁵⁻²⁷ To study the effects of particle sticking systematically, we formulated “reduced-sticking” and “sticking” conditions for both PVDF and PTFE membranes (see **Table 5-1** for details). For the PVDF membrane, 200 nm tracer particles were used to achieve the “reduced-sticking” experimental condition; experiments with 40 nm tracer particles and experiments with 200 nm tracer particles in a solvent with reduced concentration of surfactant

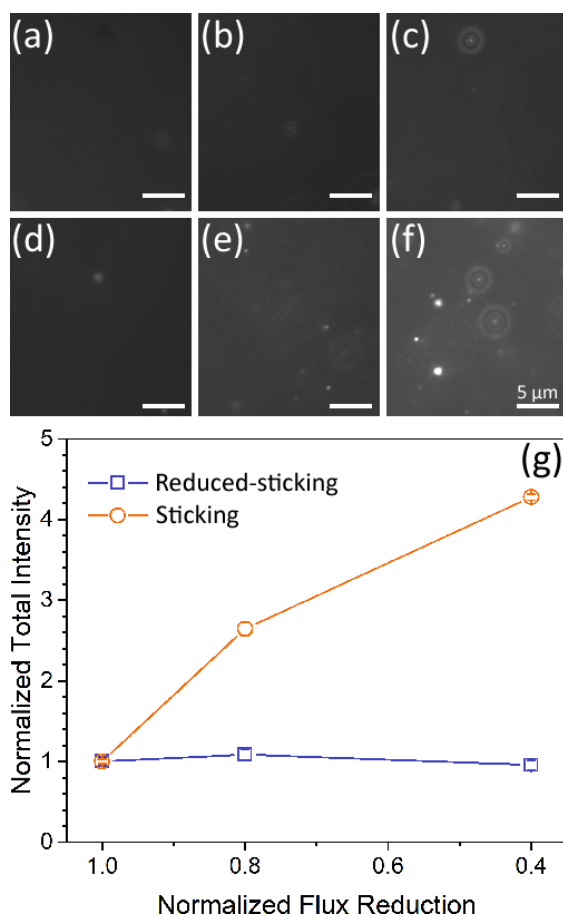


Figure 5-3. Snapshots of 200 nm tracer particles in the field of view in (a–c) a “reduced-sticking” condition (high surfactant concentration) and (d–f) a “sticking” condition (reduced surfactant) in PVDF membrane. Panels (a) and (d) correspond to a normalized flux of 100%; panels (b) and (e) correspond to a normalized flux of ~80%; panels (c) and (f) correspond to an effective flux of ~40%. (g) Normalized total fluorescence intensity of the field of view vs normalized flux reduction for the two experimental conditions.

were used to study membrane fouling in “sticking” conditions. For the PTFE membrane, which has low surface energy and therefore lower affinity to solutes,²⁸ we formulated the “reduced-sticking” condition with 40 nm tracer particles in a solvent with 1% surfactant, and the “sticking” condition used 40 nm tracer particle in a solvent with only 0.2% surfactant. To directly demonstrate the difference in “stickiness” of tracer particles during fouling processes, snapshots of 200 nm tracer particles in a PVDF membrane under a “reduced-sticking” condition and a “sticking” condition at different fouling stages are shown in **Figure 5-3**. Bright spots in these snapshots indicate fluorescent tracer particles, and the sticking of particles to the interior surface of membrane resulted in the appearance of a larger number of visible bright spots and an increase in the overall brightness in the field of view (due to background fluorescence out of the focal plane). Under “reduced-sticking” conditions (**Figures 5-3 a–c**), no dramatic change was observed with fouling, indicating minimal adsorption to the interior surface of membrane. In contrast, under “sticking” conditions (**Figures 5-3 d–f**), many more particle sticking events were observed as the membrane was increasingly fouled, and the background of the field of view became visibly brighter. Notably, the very bright objects in **Figure 5-3f** gradually grew to be larger than that of the point-spread-function (i.e. they were not diffraction-limited), consistent with the formation of large clusters/aggregates of tracer particles. To quantify the evolution of particle sticking, we calculated the total intensity of all the pixels in the field of view as a function of flux reduction, as shown in **Figure 5-3g**. While the total intensity remained almost constant in “reduced-sticking” conditions, it increased strikingly to more than four times the original value under “sticking” conditions, demonstrating the qualitative difference between these two experimental conditions.

5.4.2 Visualizing Particle Trajectories in Fouling Processes

To visualize particle trajectories in different fouling scenarios, we constructed representative trajectory maps in PVDF membranes under “reduced-sticking” (200 nm tracer particles with 36% surfactant, **Figures 5-4 a–c**) and “sticking” conditions (200 nm tracer particles with 1% surfactant, **Figures 5-4 d–f**), respectively, at different stages of fouling (see **Figure D1** & **Figure D2** in Appendix D for representative trajectory maps of 40 nm tracer particles in PVDF and PTFE membranes). In each panel, trajectories of particles flowing in the field of view within 7.5 minutes were overlaid. In both cases, the number of sampled trajectories decreased significantly as membranes were increasingly fouled, as only a subset of pathways was followed by tracer particles at later stages of fouling. Fouling behaviors in these two cases were visibly different. Qualitatively, fouling occurred faster under “sticking” conditions since the reduction of sampled trajectories appeared to be more dramatic (as shown in **Figures 5-4e** & **5-4f**). In comparison, for the conditions with reduced-sticking, a minimal decrease in the number of sampled trajectories was observed in 55 minutes as shown in **Figure 5-4b**, and a considerable number of trajectories were still sampled after 90 minutes of fouling (**Figure 5-4c**). Additionally, the shapes of trajectories (representing the geometrical shapes of the available pathways in membrane) under “sticking” conditions were similar at different fouling stages; while in the “reduced-sticking” case, the sampled trajectories appeared to be more tortuous as fouling progressed (especially in **Figure 5-4c**). These effects are analyzed more quantitatively below.

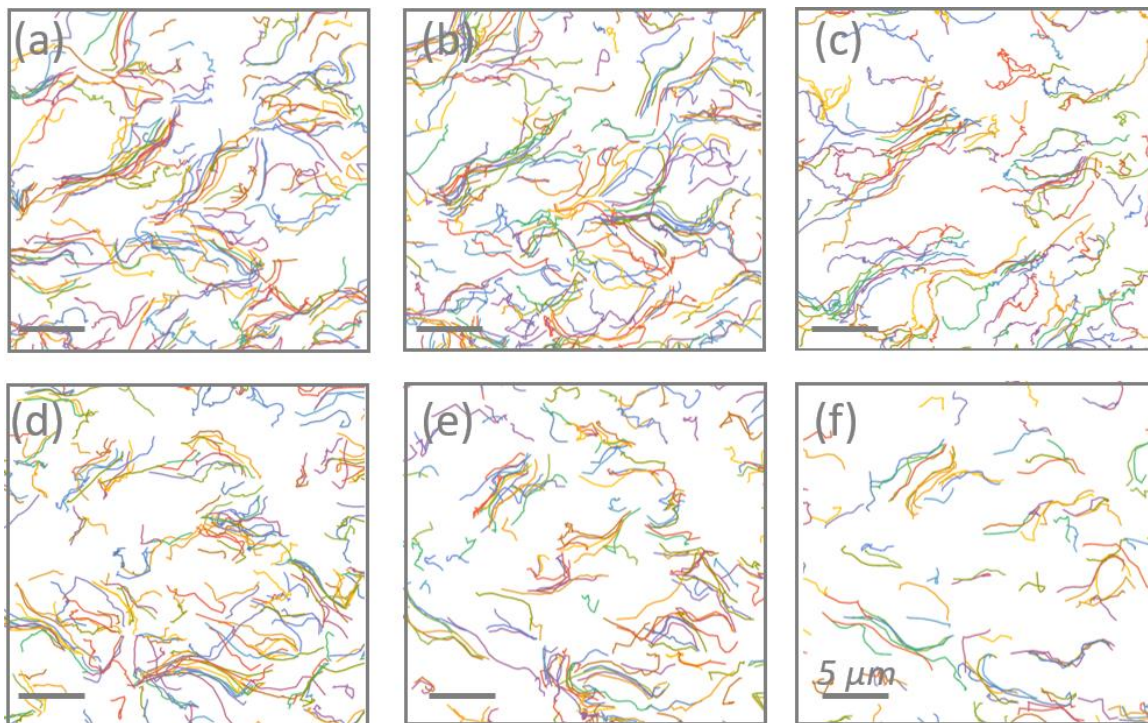


Figure 5-4. (a–c) Representative trajectory maps of 200 nm tracer particles in a PVDF membrane under “reduced-sticking” conditions. Trajectories collected in (a) 0–7.5 min, (b) 55–62.5 min and (c) 90–97.5 min were overlaid in each panel. (d–f) Representative trajectory maps of 200 nm tracer particles in PVDF membrane under “sticking” conditions. Trajectories collected in (d) 0–7.5 min, (e) 55–62.5 min and (f) 85–92.5 min were overlaid in each panel.

5.4.3 Evolution of Effective Flux and Particle Velocity

While different fouling behaviors in the “reduced-sticking” and the “sticking” conditions were qualitatively visible in the trajectory maps, we performed detailed statistical analyses to compare those behaviors quantitatively. Specifically, we analyzed how the effective flux and the velocity of particles evolved over time in different fouling scenarios. Since the experiments in each membrane were conducted under the same pressure drop and the initial flux values were similar, we used normalized flux to compare the fouling behaviors under different experiment conditions. **Figure 5-5** shows the normalized effective flux (estimated by the number of moving objects appeared in the field of view within a certain time period) versus time curves for fouling in PVDF (**Figure 5-5a**) and PTFE membranes (**Figure 5-5b**) under “reduced-sticking” and “sticking” conditions, respectively. Each data point was averaged from two replicate experiments. Despite the fact that the two membrane materials had very different properties in terms of both surface chemistry and geometrical structure, we found the effect of sticking on fouling behaviors in the two membranes to be qualitatively similar. For both membranes, the decrease of flux appeared to be much more gradual in the “reduced-sticking” condition compared to the “sticking” condition(s). For example, the effective flux dropped to 50% in less than 60 min under all “sticking” conditions in the two membranes, while it required ~120 min (for PVDF membranes) or even longer (for PTFE membranes) under “reduced-sticking” conditions. Evidently, fouling was significantly attenuated by the reduction of particle sticking.

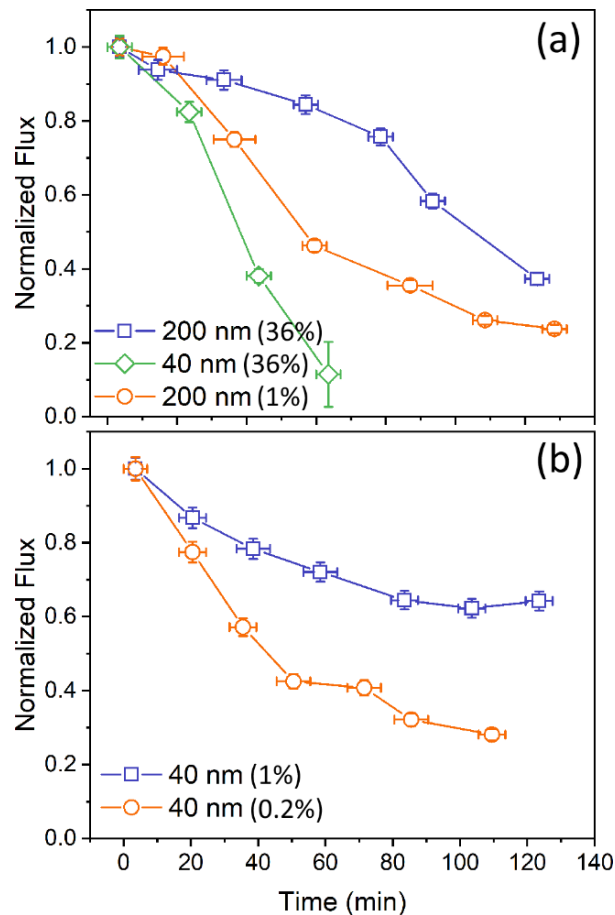


Figure 5-5. Normalized effective flux vs time for (a) PVDF and (b) PTFE membranes under various experimental conditions. Percentages in parentheses in legends indicate surfactant concentrations. Dark blue symbols represent “reduced-sticking” conditions, orange and green symbols represent “sticking” conditions. Error bars for the time axis indicate the duration of “bins” (i.e. time intervals that trajectories were collected) within which flux was averaged. The error bars for normalized flux represent uncertainties in counted particles assuming Poisson statistics.

Moreover, with the single-particle tracking approach, we were able to characterize the velocity of particles flowing through individual pathways, which was determined by the local resistance of the corresponding pathways. Again, we used normalized velocity to compare different experimental conditions as the initial velocity values were similar in each membrane. Normalized mean particle velocity versus normalized flux reduction curves were constructed and shown in **Figure 5-6** for different experimental conditions. For both membranes, the particle velocity exhibited minimal changes with flux reduction under “sticking” conditions. In contrast, for the “reduced-sticking” conditions, the particle velocity decreased systematically with flux reduction. For example, for the PVDF membrane under “reduced-sticking” conditions, the mean velocity decreased to ~50% as the effective flux declined to ~40%. Similarly, the mean velocity decreased to ~70% at an effective flux of ~50% for PTFE membrane under “reduced-sticking” conditions. Since all experiments were performed under constant pressure conditions, the decrease of velocity was attributed to the increase of resistance in individual pathways through which the particles flowed.^{13, 29} As a result, we hypothesized that available pathways were “narrowed” in the “reduced-sticking” conditions as membranes were increasingly fouled, based on the explicit correlations between particle velocity and flux reduction.^{30, 31} Notably, since the effective flux actually declined somewhat more than the particle velocity in both membranes under “reduced-sticking” conditions, this suggested that as pathways were increasingly narrowed, a small fraction of them eventually became too narrow for particles to flow through; and the closure of those pathways represented a secondary contributor for flux reduction in “reduced-sticking” conditions. As discussed in more detail below, we hypothesize that this narrowing of pathways was dominated by the deposition of particles within constrictions, which occurred

gradually under reduced sticking conditions due to the weak particle–particle and particle–surface interactions.

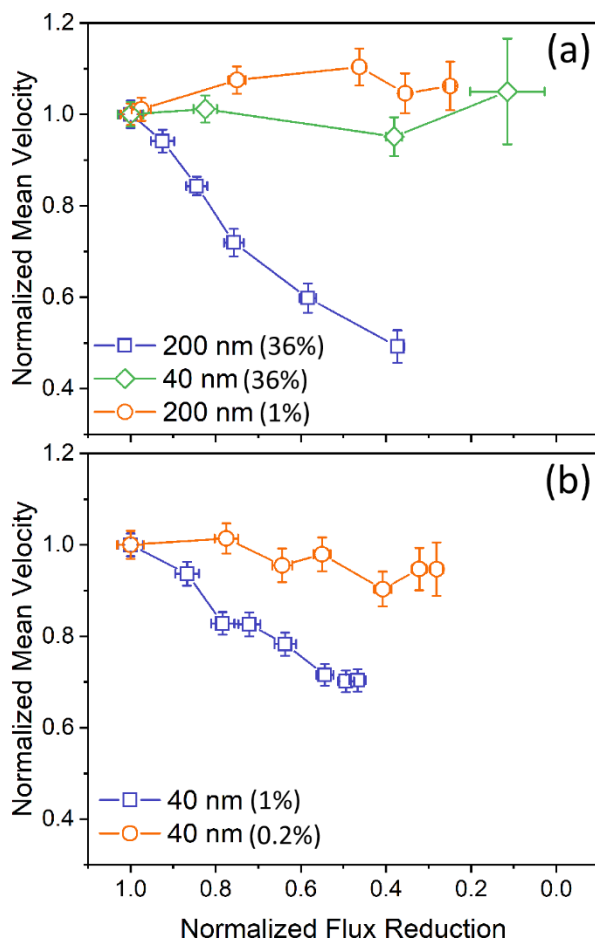


Figure 5-6. Normalized mean particle velocity vs normalized flux reduction for (a) PVDF and (b) PTFE membranes. Percentages in parentheses in legends indicate surfactant concentrations. Dark blue symbols represent “reduced-sticking” conditions, orange and green symbols represent “sticking” conditions. Error bars for normalized mean velocity indicate standard errors, error bars for normalized flux reduction were estimated using Poisson statistics.

In contrast, under “sticking” conditions, no correlation was observed between flux reduction and particle velocity, and, in fact, the velocity of mobile particles remained nearly constant with time, i.e. the reduction in flux was entirely due to the reduction in the number of particles, not their velocity. This suggested that the local resistance for available pathways remained unchanged, and that the decrease of flux was dominated by the complete blocking of certain pathways.^{15, 32, 33} Motivated by the observations of particle aggregates shown in **Figure 5-3a**, we hypothesize that the “sticky” particles aggregated within constrictions, forming catastrophic blockages. A more detailed discussion is given below in Section 5.3.5.

5.4.4 Progression of Membrane Functional Tortuosity

In order to study the evolutions of the effective membrane structure during fouling, we calculated tortuosity distributions (for tracer particle trajectories passing through available pathways) as a function of effective flux, as shown in **Figure 5-7**. We observed that under “reduced-sticking” conditions, in both PVDF (**Figure 5-7a**) and PTFE membranes (**Figure 5-7c**), the apparent tortuosity of available pathways increased systematically with increasing fouling, indicated by a rightward shift of the tortuosity distributions. This transition was more dramatic for trajectories in the PVDF membrane (**Figure 5-7a**), but still apparent (especially the shift in the peaks of the distributions) in the PTFE membrane (**Figure 5-7c**). In previous work on membrane tortuosity, we observed that the apparent tortuosity of pathways was sensitive to both particle velocity and to the particle size/pore size ratio. Specifically, a decrease in particle velocity and an increase in the particle size/pore size ratio resulted in larger apparent tortuosity values.¹⁹ Therefore, for the “reduced-sticking” scenarios presented here, the decrease of the

particle velocity as fouling progressed could partially explain the observed increase in apparent tortuosity. In particular, at lower velocity (i.e. lower Péclet number), particles flowed less deterministically in the flow direction and were more likely to diffusively explore alternative pathways in the lateral directions, therefore exhibiting greater tortuosity. Moreover, as discussed above, the decrease of particle velocity also suggested the narrowing of available pathways. Consequently, the increase of the particle size/pore size ratio during fouling under “reduced-sticking” conditions would also result in increased apparent tortuosity, since this could result in the formation of obstructions that force particles to deviate into alternative pathways. In summary, more direct (i.e. less tortuous) pathways were presumably narrowed or closed earlier in the fouling process (presumably because they were more accessible to particles), and the remaining pathways exhibited higher tortuosity. This was also consistent with the fact that effective flux decreased faster than the particle velocity, which could be explained by the closure of a small fraction of pathways.

In contrast, under “sticking” conditions (**Figures 5-7b** and **5-7d**), the tortuosity of the available pathways in both membranes remained unchanged during the fouling process, which was consistent with the fact that the mean particle velocity also remained constant. Evidently, the pathways that remained open were still representative of the original pathways, and the closing of pathways, which was believed to be the dominant factor causing membrane fouling in this case, was stochastic.

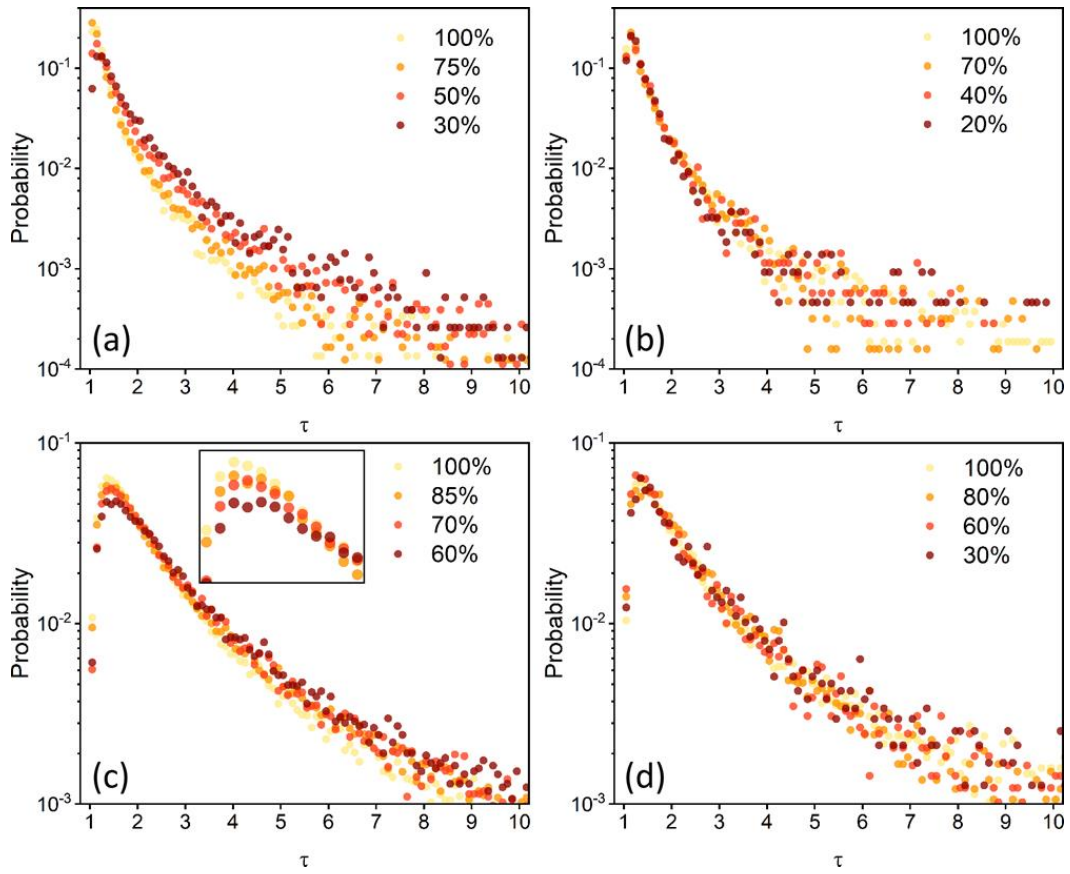


Figure 5-7. Probability distributions of local tortuosity for 200 nm tracer particles in PVDF membranes (a) with high surfactant concentration ("reduced-sticking") and (b) with reduced surfactant ("sticking"), and for 40 nm tracer particles in PTFE membranes (c) with 1% surfactant ("reduced-sticking") and (d) with 0.2% surfactant ("sticking") at different stages of fouling. Percentages in legends indicate normalized flux.

5.4.5 Hypothetical Fouling Mechanisms

The empirical observation of qualitatively different fouling behaviors under “reduced-sticking” conditions and “sticking” conditions (in both PVDF and PTFE membranes) suggests that the “stickiness” of tracer particles is a determining factor in fouling processes. We previously found that the existence of anomalous highly confining regions in filtration membranes was instrumental in causing more meandering trajectories and longer retention times.¹⁹ Here we hypothesize that these confining regions also influence the observed fouling behaviors (illustrated in **Figure 5-8**). Being generally more retentive, these constrictions tend to retain tracer particles.^{19, 20, 34} However, under “reduced-sticking” conditions, even with particles already stuck in the constrictions, incoming particles could potentially pass through the narrowed constriction, since particle-surface interactions and particle-particle interactions were significantly reduced. Nevertheless, the particles immobilized in the constrictions would increase the resistance of pathways gradually, resulting in a systematic decrease of the mean particle

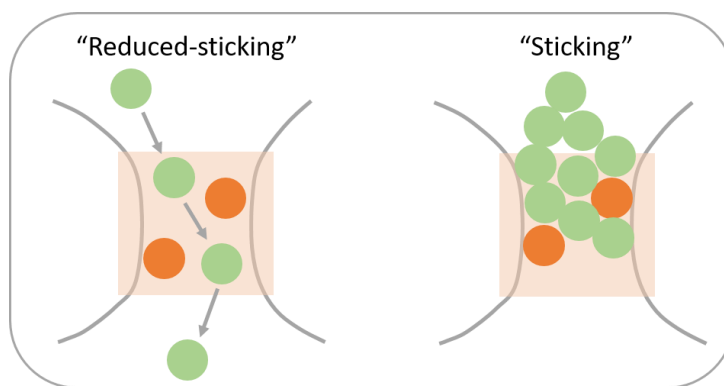


Figure 5-8. Schematic diagrams of different fouling mechanisms in membrane constrictions (denoted by light coral squares) under “reduced-sticking” and “sticking” conditions. Orange circles represent particles that were stuck in the constrictions and green circles represent incoming particles.

velocity. Moreover, as discussed earlier in this article, the “narrowing” of pathways in this case eventually results in the formation of obstacles and forces particles into detours. This “exclusion” effect, together with the decrease of particle velocity, was likely to bring about an increase in pathway tortuosity. However, under “sticking” conditions, with substantial particle-surface interactions and particle-particle interactions, the retention of one or more particle(s) in a constriction is likely to lead to further aggregation of incoming particles, leading to rapid pore blocking. This hypothesis was supported by the observation of particle clusters at later fouling stages (as shown in **Figure 5-3f**) under “sticking” conditions. Since the sticking of particles in constrictions could easily become catastrophic and lead to the rapid closure of pathways, it is reasonable to assume that particles able to flow through the membranes without being held up at any of the constrictions used only “clean” pathways which remained the same resistance and tortuosity. As a consequence, under “sticking” conditions, the apparent velocity of particles and pathway tortuosity exhibited minimal changes as the membranes were increasingly fouled.

5.5 CONCLUSIONS

A single-particle tracking approach was employed to study the effects of particle “stickiness” on membrane fouling. With direct observations of particle trajectories in membrane under different conditions, we found that the sticking of particles had substantial impacts on fouling mechanisms. When particle sticking was reduced, fouling occurred more slowly, and we observed a systematic decrease of particle velocity and an increase in the apparent tortuosity (of available pathways) as a function of flux reduction. In contrast, under “sticking” conditions,

despite the fact that fouling occurred more quickly, both particle velocity and apparent tortuosity remained constant as fouling progressed. We proposed that the presence of highly confining regions in membrane was crucial to the presence of these distinct fouling mechanisms. Specifically, such constrictions were presumably “narrowed” gradually under “reduced-sticking” conditions, explaining the decrease of particle velocity and the increase of pathway tortuosity; and were blocked rapidly under the “sticking” conditions where both particle-surface interactions and particle-particle interactions were much more significant. These interpretations were further supported by direct observations of retained particle aggregates under “sticking” conditions, but not under “reduced-sticking” conditions.

Importantly, the particle-tracking technique employed here enabled the visualization of fouling processes in filtration membranes and provided direct evidence of fouling mechanisms under specific operating scenarios. This valuable information could benefit the design and optimization of filtration processes with reduced fouling effects. The comprehensive information provided by the direct observation of particle trajectories, including the analysis of particle velocity and pathway tortuosity, has significant potential to advance the understanding of the complex and heterogeneous mass transport during filtration processes.

5.6 REFERENCES

1. van Reis, R.; Zydney, A., Bioprocess membrane technology. *J. Membr. Sci.* **2007**, 297 (1), 16-50.
2. Watson, D. S.; Kerchner, K. R.; Gant, S. S.; Pedersen, J. W.; Hamburger, J. B.; Ortigosa, A. D.; Potgieter, T. I., At-line process analytical technology (PAT) for more efficient scale up of biopharmaceutical microfiltration unit operations. *Biotechnol. Prog.* **2016**, 32 (1), 108-115.

3. Castilho, P. H.; Correia, T. R.; Pessoa de Amorim, M. T.; Escobar, I. C.; Queiroz, J. A.; Correia, I. J.; Morão, A. M., Modification of microfiltration membranes by hydrogel impregnation for pDNA purification. *J. Appl. Polym. Sci.* **2015**, *132* (21).
4. Ding, Q.; Yamamura, H.; Murata, N.; Aoki, N.; Yonekawa, H.; Hafuka, A.; Watanabe, Y., Characteristics of meso-particles formed in coagulation process causing irreversible membrane fouling in the coagulation-microfiltration water treatment. *Water Res.* **2016**, *101*, 127-136.
5. Lindquist, E. D.; Norman, W. R.; Soerens, T., A review of: Fouling in hollow fiber membrane microfilters used for household water treatment. *J. Water, Sanit. Hyg. Dev.* **2015**, *5* (2), 229-231.
6. Qin, W.; Zhang, J.; Xie, Z.; Ng, D.; Ye, Y.; Gray, S. R.; Xie, M., Synergistic effect of combined colloidal and organic fouling in membrane distillation: Measurements and mechanisms. *Environ. Sci.: Water Res. Technol.* **2017**, *3* (1), 119-127.
7. Alfano, A.; Donnarumma, G.; Cimini, D.; Fusco, A.; Marzaioli, I.; De Rosa, M.; Schiraldi, C., Lactobacillus plantarum: Microfiltration experiments for the production of probiotic biomass to be used in food and nutraceutical preparations. *Biotechnol. Prog.* **2015**, *31* (2), 325-333.
8. de Cazes, M. d.; Belleville, M.-P.; Mougél, M.; Kellner, H.; Sanchez-Marcano, J., Characterization of laccase-grafted ceramic membranes for pharmaceuticals degradation. *J. Membr. Sci.* **2015**, *476*, 384-393.
9. Ganiyu, S. O.; van Hullebusch, E. D.; Cretin, M.; Esposito, G.; Oturan, M. A., Coupling of membrane filtration and advanced oxidation processes for removal of pharmaceutical residues: a critical review. *Sep. Purif. Technol.* **2015**, *156*, 891-914.
10. Wang, Y.; Zhu, J.; Huang, H.; Cho, H.-H., Carbon nanotube composite membranes for microfiltration of pharmaceuticals and personal care products: Capabilities and potential mechanisms. *J. Membr. Sci.* **2015**, *479*, 165-174.
11. Guo, W.; Ngo, H.-H.; Li, J., A mini-review on membrane fouling. *Bioresour. technol.* **2012**, *122*, 27-34.
12. Henry, C.; Minier, J.-P.; Lefèvre, G., Towards a description of particulate fouling: From single particle deposition to clogging. *Adv. colloid interface sci.* **2012**, *185*, 34-76.

13. Miller, D. J.; Kasemset, S.; Paul, D. R.; Freeman, B. D., Comparison of membrane fouling at constant flux and constant transmembrane pressure conditions. *J. Membr. Sci.* **2014**, *454*, 505-515.
14. Bolton, G.; LaCasse, D.; Kuriyel, R., Combined models of membrane fouling: development and application to microfiltration and ultrafiltration of biological fluids. *J. Membr. Sci.* **2006**, *277* (1), 75-84.
15. Wang, F.; Tarabara, V. V., Pore blocking mechanisms during early stages of membrane fouling by colloids. *J. Colloid Interface Sci.* **2008**, *328* (2), 464-9.
16. Bowen, W.; Calvo, J.; Hernandez, A., Steps of membrane blocking in flux decline during protein microfiltration. *J. Membr. Sci.* **1995**, *101* (1-2), 153-165.
17. Ho, C.-C.; Zydney, A. L., A combined pore blockage and cake filtration model for protein fouling during microfiltration. *J. Colloid Interface Sci.* **2000**, *232* (2), 389-399.
18. Corbatón-Báguena, M.-J.; Álvarez-Blanco, S.; Vincent-Vela, M.-C., Fouling mechanisms of ultrafiltration membranes fouled with whey model solutions. *Desalination* **2015**, *360*, 87-96.
19. Cai, Y.; Schwartz, D. K., Mapping the Functional Tortuosity and Spatiotemporal Heterogeneity of Porous Polymer Membranes with Super-Resolution Nanoparticle Tracking. *ACS Appl. Mater. Interfaces* **2017**, *9* (49), 43258-43266.
20. Skaug, M. J.; Wang, L.; Ding, Y.; Schwartz, D. K., Hindered nanoparticle diffusion and void accessibility in a three-dimensional porous medium. *ACS Nano* **2015**, *9* (2), 2148-2156.
21. Cai, Y.; Schwartz, D. K., Influence of protein surface coverage on anomalously strong adsorption sites. *ACS Appl. Mater. Interfaces* **2015**, *8* (1), 511-520.
22. Cai, Y.; Shashikanth, N.; Leckband, D. E.; Schwartz, D. K., Cadherin diffusion in supported lipid bilayers exhibits calcium-dependent dynamic heterogeneity. *Biophys. J.* **2016**, *111* (12), 2658-2665.
23. Honciuc, A.; Harant, A. W.; Schwartz, D. K., Single-molecule observations of surfactant diffusion at the solution– solid interface. *Langmuir* **2008**, *24* (13), 6562-6566.
24. Janna, W. S., *Introduction to fluid mechanics*. CRC press: 2009.

25. Hiemenz, P. C.; Hiemenz, P. C., *Principles of colloid and surface chemistry*. M. Dekker New York: 1986; Vol. 9.
26. Roach, L. S.; Song, H.; Ismagilov, R. F., Controlling nonspecific protein adsorption in a plug-based microfluidic system by controlling interfacial chemistry using fluorosurfactants. *Analytical chemistry* **2005**, 77 (3), 785-796.
27. Zhang, X.; Niu, L.; Yu, S.; Li, F.; Zhao, X.; Hu, H., Influence of low-level anionic surfactant on PES ultrafiltration performance: membrane fouling and rejection of nuclides. *Water, Air, & Soil Pollution* **2016**, 227 (8), 274.
28. Wong, T.-S.; Kang, S. H.; Tang, S. K.; Smythe, E. J.; Hatton, B. D.; Grinthal, A.; Aizenberg, J., Bioinspired self-repairing slippery surfaces with pressure-stable omniphobicity. *Nature* **2011**, 477 (7365), 443-447.
29. Iritani, E.; Katagiri, N.; Yamashita, Y., Effect of membrane morphology on rising properties of filtration resistance in microfiltration of dilute colloids. *AIChE Journal* **2017**.
30. Shannon, M. A.; Bohn, P. W.; Elimelech, M.; Georgiadis, J. G.; Mariñas, B. J.; Mayes, A. M., Science and technology for water purification in the coming decades. *Nature* **2008**, 452 (7185), 301-310.
31. Mulder, J., *Basic principles of membrane technology*. Springer Science & Business Media: 2012.
32. Lee, J.-K.; Liu, B. Y., An experimental study of particulate retention by microporous membranes in liquid filtration. *KSME J.* **1994**, 8 (1), 69-77.
33. Chen, S.-C.; Segets, D.; Ling, T.-Y.; Peukert, W.; Pui, D. Y., An experimental study of ultrafiltration for sub-10 nm quantum dots and sub-150 nm nanoparticles through PTFE membrane and Nuclepore filters. *J. Membr. Sci.* **2016**, 497, 153-161.
34. Skaug, M. J.; Schwartz, D. K., Tracking nanoparticle diffusion in porous filtration media. *Ind. Eng. Chem. Res.* **2015**, 54 (16), 4414-4419.

Bibliography

Aissaoui, N.; Bergaoui, L.; Landoulsi, J.; Lambert, J. F.; Boujday, S., Silane layers on silicon surfaces: mechanism of interaction, stability, and influence on protein adsorption. *Langmuir* 2012, 28 (1), 656-65.

Alfano, A.; Donnarumma, G.; Cimini, D.; Fusco, A.; Marzaioli, I.; De Rosa, M.; Schiraldi, C., *Lactobacillus plantarum*: Microfiltration experiments for the production of probiotic biomass to be used in food and nutraceutical preparations. *Biotechnol. Prog.* 2015, 31 (2), 325-333.

Allen, L. T.; Tosetto, M.; Miller, I. S.; O'Connor, D. P.; Penney, S. C.; Lynch, I.; Keenan, A. K.; Pennington, S. R.; Dawson, K. A.; Gallagher, W. M., Surface-induced changes in protein adsorption and implications for cellular phenotypic responses to surface interaction. *Biomaterials* 2006, 27 (16), 3096-108.

Andreasen, P., Free and total calcium concentrations in the blood of rainbow trout, *Salmo gairdneri*, during 'stress' conditions. *J. Exp. Biol.* 1985, 118, 111-120.

Arai, T.; Norde, W., The behavior of some model proteins at solid-liquid interfaces 1. Adsorption from single protein solutions. *Colloids Surf.* 1990, 51, 1-15.

Asanov, A. N.; Delucas, L. J.; Oldham, P. B.; Wilson, W. W., Heteroenergetics of bovine serum albumin adsorption from good solvents related to crystallization conditions. *J. Colloid Interface Sci.* 1997, 191 (1), 222-235.

Asenath Smith, E.; Chen, W., How to prevent the loss of surface functionality derived from aminosilanes. *Langmuir* 2008, 24 (21), 12405-12409.

Banerjee, I.; Pangule, R. C.; Kane, R. S., Antifouling coatings: recent developments in the design of surfaces that prevent fouling by proteins, bacteria, and marine organisms. *Adv. Mater.* 2011, 23 (6), 690-718.

Baumgartner, W.; Golenhofen, N.; Grundhöfer, N.; Wiegand, J.; Drenckhahn, D., Ca^{2+} dependency of N-cadherin function probed by laser tweezer and atomic force microscopy. *The Journal of neuroscience* 2003, 23 (35), 11008-11014.

Bavari, S.; Bosio, C. M.; Wiegand, E.; Ruthel, G.; Will, A. B.; Geisbert, T. W.; Hevey, M.; Schmaljohn, C.; Schmaljohn, A.; Aman, M. J., Lipid Raft Microdomains A Gateway for Compartmentalized Trafficking of Ebola and Marburg Viruses. *J. Exp. Med.* 2002, 195 (5), 593-602.

Belanger, M.-C.; Marois, Y., Hemocompatibility, Biocompatibility, Inflammatory and in Vivo Studies of Primary Reference Materials Low-Density Polyethylene and Polydimethylsiloxane: A Review. *J. Biomed. Mater. Res.* 2001, 58 (5), 467-477.

Benninger, C.; Kadis, J.; Prince, D., Extracellular calcium and potassium changes in hippocampal slices. *Brain Res.* 1980, 187 (1), 165-182.

Berg, C. F.; Held, R., Fundamental transport property relations in porous media incorporating detailed pore structure description. *Transport Porous Med.* 2016, 112 (2), 467-487.

Bhambure, R.; Sharma, I.; Pattanayek, S. K.; Rathore, A. S., Qualitative and quantitative examination of non-specific protein adsorption on filter membrane disks of a commercially available high throughput chromatography device. *J. Membr. Sci.* 2014, 451, 312-318.

Bhatia, S., Directional autocorrelation and the diffusional tortuosity of capillary porous media. *J. Catal.* 1985, 93 (1), 192-196.

Biswas, K. H.; Hartman, K. L.; Yu, C.-h.; Harrison, O. J.; Song, H.; Smith, A. W.; Huang, W. Y.; Lin, W.-C.; Guo, Z.; Padmanabhan, A., E-cadherin junction formation involves an active kinetic nucleation process. *Proc. Natl. Acad. Sci. U. S. A.* 2015, 112 (35), 10932-10937.

Bloomfield, V., The Structure of Bovine Serum Albumin at Low pH*. *Biochemistry* 1966, 5 (2), 684-689.

Boggon, T. J.; Murray, J.; Chappuis-Flament, S.; Wong, E.; Gumbiner, B. M.; Shapiro, L., C-cadherin ectodomain structure and implications for cell adhesion mechanisms. *Science* 2002, 296 (5571), 1308-1313.

Bolis, V.; Cavenago, A.; Fubini, B., Surface heterogeneity on hydrophilic and hydrophobic silicas: water and alcohols as probes for H-bonding and dispersion forces. *Langmuir* 1997, 13 (5), 895-902.

Bolton, G.; LaCasse, D.; Kuriyel, R., Combined models of membrane fouling: development and application to microfiltration and ultrafiltration of biological fluids. *J. Membr. Sci.* 2006, 277 (1), 75-84.

Bowen, W.; Calvo, J.; Hernandez, A., Steps of membrane blocking in flux decline during protein microfiltration. *J. Membr. Sci.* 1995, 101 (1-2), 153-165.

Boyce, S. T.; Ham, R. G., Calcium-regulated differentiation of normal human epidermal keratinocytes in chemically defined clonal culture and serum-free serial culture. *J. Invest. Dermatol.* 1983, 81, 33-40.

Brown, E. M.; Vassilev, P. M.; Hebert, S. C., Calcium ions as extracellular messengers. *Cell* 1995, 83 (5), 679-682.

Cai, Y.; Schwartz, D. K., Influence of protein surface coverage on anomalously strong adsorption sites. *ACS Appl. Mater. Interfaces* 2015, 8 (1), 511-520.

Cai, Y.; Schwartz, D. K., Influence of protein surface coverage on anomalously strong adsorption sites. *ACS Appl. Mater. Interfaces* 2015.

Cai, Y.; Schwartz, D. K., Mapping the Functional Tortuosity and Spatiotemporal Heterogeneity of Porous Polymer Membranes with Super-Resolution Nanoparticle Tracking. *ACS Appl. Mater. Interfaces* 2017, 9 (49), 43258-43266.

Cai, Y.; Schwartz, D. K., Single-nanoparticle tracking reveals mechanisms of membrane fouling. *J. Membr. Sci.* 2018.

Cai, Y.; Shashikanth, N.; Leckband, D. E.; Schwartz, D. K., Cadherin diffusion in supported lipid bilayers exhibits calcium-dependent dynamic heterogeneity. *Biophys. J.* 2016, 111 (12), 2658-2665.

Carter, D. C.; Ho, J. X., Structure of serum albumin. *Adv. Protein Chem.* 1994, 45 (45), 153-203.

Castilho, P. H.; Correia, T. R.; Pessoa de Amorim, M. T.; Escobar, I. C.; Queiroz, J. A.; Correia, I. J.; Morão, A. M., Modification of microfiltration membranes by hydrogel impregnation for pDNA purification. *J. Appl. Polym. Sci.* 2015, 132 (21).

Chang, H.; Reitstetter, R.; Gruener, R., Lipid-ion channel interactions: increasing phospholipid headgroup size but not ordering acyl chains alters reconstituted channel behavior. *J. Membr. Biol.* 1995, 145 (1), 13-19.

Chang, I.-S.; Le Clech, P.; Jefferson, B.; Judd, S., Membrane fouling in membrane bioreactors for wastewater treatment. *J. Environ. Eng.* 2002, 128 (11), 1018-1029.

Chaparro Sosa, A. F.; Kienle, D. F.; Falatach, R. M.; Flanagan, J.; Kaar, J. L.; Schwartz, D. K., Stabilization of Immobilized Enzymes via the Chaperone-like Activity of Mixed Lipid Bilayers. ACS Appl. Mater. Interfaces 2018.

Charmas, B.; Leboda, R., Effect of surface heterogeneity on adsorption on solid surfaces: application of inverse gas chromatography in the studies of energetic heterogeneity of adsorbents. J. Chromatogr. A 2000, 886 (1), 133-152.

Chatelier, R. C.; Minton, A. P., Adsorption of globular proteins on locally planar surfaces: models for the effect of excluded surface area and aggregation of adsorbed protein on adsorption equilibria. Biophys. J. 1996, 71 (5), 2367.

Chen, S.-C.; Segets, D.; Ling, T.-Y.; Peukert, W.; Pui, D. Y., An experimental study of ultrafiltration for sub-10 nm quantum dots and sub-150 nm nanoparticles through PTFE membrane and Nuclepore filters. J. Membr. Sci. 2016, 497, 153-161.

Cho, J.; Amy, G.; Pellegrino, J., Membrane filtration of natural organic matter: factors and mechanisms affecting rejection and flux decline with charged ultrafiltration (UF) membrane. J. Membr. Sci. 2000, 164 (1), 89-110.

Chothia, C.; Jones, E. Y., The molecular structure of cell adhesion molecules. Annu. Rev. Biochem. 1997, 66 (1), 823-862.

Corbatón-Báguena, M.-J.; Álvarez-Blanco, S.; Vincent-Vela, M.-C., Fouling mechanisms of ultrafiltration membranes fouled with whey model solutions. Desalination 2015, 360, 87-96.

Courjean, O.; Chevreux, G.; Perret, E.; Morel, A.; Sanglier, S.; Potier, N.; Engel, J.; Van Dorsselaer, A.; Feracci, H., Modulation of E-cadherin monomer folding by cooperative binding of calcium ions. Biochemistry 2008, 47 (8), 2339-2349.

Cremer, P. S.; Boxer, S. G., Formation and spreading of lipid bilayers on planar glass supports. J. Phys. Chem. B 1999, 103 (13), 2554-2559.

Datta, S. S.; Chiang, H.; Ramakrishnan, T.; Weitz, D. A., Spatial fluctuations of fluid velocities in flow through a three-dimensional porous medium. Phys. Rev. Lett. 2013, 111 (6), 064501.

David, C., Geometry of flow paths for fluid transport in rocks. J. Geophys. Res.: Solid Earth 1993, 98 (B7), 12267-12278.

de Cazes, M. d.; Belleville, M.-P.; Mougél, M.; Kellner, H.; Sanchez-Marcano, J., Characterization of laccase-grafted ceramic membranes for pharmaceuticals degradation. *J. Membr. Sci.* 2015, 476, 384-393.

Deis, L. N.; Wu, Q.; Wang, Y.; Qi, Y.; Daniels, K. G.; Zhou, P.; Oas, T. G., suppression of conformational heterogeneity at a protein-protein interface. *Proc. Natl. Acad. Sci. U. S. A.* 2015, 112 (29), 9028-9033.

Dentz, M.; Cortis, A.; Scher, H.; Berkowitz, B., Time behavior of solute transport in heterogeneous media: transition from anomalous to normal transport. *Adv. Water Resour.* 2004, 27 (2), 155-173.

Ding, Q.; Yamamura, H.; Murata, N.; Aoki, N.; Yonekawa, H.; Hafuka, A.; Watanabe, Y., Characteristics of meso-particles formed in coagulation process causing irreversible membrane fouling in the coagulation-microfiltration water treatment. *Water Res.* 2016, 101, 127-136.

DuBeshter, T.; Sinha, P. K.; Sakars, A.; Fly, G. W.; Jorne, J., Measurement of tortuosity and porosity of porous battery electrodes. *J. Electrochem. Soc.* 2014, 161 (4), A599-A605.

Dykhuizen, R. C.; Casey, W. H., An analysis of solute diffusion in rocks. *Geochim. Cosmochim. Acta* 1989, 53 (11), 2797-2805.

Eckstein, E. C.; Bailey, D. G.; Shapiro, A. H., Self-diffusion of particles in shear flow of a suspension. *J. Fluid Mech.* 1977, 79 (1), 191-208.

Ederly, Y.; Guadagnini, A.; Scher, H.; Berkowitz, B., Origins of anomalous transport in heterogeneous media: Structural and dynamic controls. *Water Resour. Res.* 2014, 50 (2), 1490-1505.

Edward, J. T., Molecular volumes and the Stokes-Einstein equation. *J. Chem. Educ.* 1970, 47 (4), 261.

Elzouki, A. Y.; Stapleton, F.; Harfi, H.; Oh, W.; Whitley, R.; Nazer, H., Textbook of clinical pediatrics. Springer Science & Business Media: 2011.

Ganiyu, S. O.; van Hullebusch, E. D.; Cretin, M.; Esposito, G.; Oturan, M. A., Coupling of membrane filtration and advanced oxidation processes for removal of pharmaceutical residues: a critical review. *Sep. Purif. Technol.* 2015, 156, 891-914.

Gao, W.; Liang, H.; Ma, J.; Han, M.; Chen, Z.-l.; Han, Z.-s.; Li, G.-b., Membrane fouling control in ultrafiltration technology for drinking water production: a review. *Desalination* 2011, 272 (1), 1-8.

Ghanbarian, B.; Hunt, A. G.; Ewing, R. P.; Sahimi, M., Tortuosity in Porous Media: A Critical Review. *Soil Sci. Soc. Am. J.* 2013, 77 (5), 1461-1477.

Ghanbarian, B.; Hunt, A. G.; Sahimi, M.; Ewing, R. P.; Skinner, T. E., Percolation theory generates a physically based description of tortuosity in saturated and unsaturated porous media. *Soil Sci. Soc. Am. J.* 2013, 77 (6), 1920-1929.

Graf, K.; Kappl, M., Physics and chemistry of interfaces. John Wiley & Sons: 2006.

Gritti, F.; Guiochon, G., Heterogeneity of the adsorption mechanism of low molecular weight compounds in reversed-phase liquid chromatography. *Anal. Chem.* 2006, 78 (16), 5823-34.

Grunwald, G. B., The structural and functional analysis of cadherin calcium-dependent cell adhesion molecules. *Curr. Opin. Cell Biol.* 1993, 5 (5), 797-805.

Guo, W.; Ngo, H.-H.; Li, J., A mini-review on membrane fouling. *Bioresour. technol.* 2012, 122, 27-34.

Hartvig, R. A.; van de Weert, M.; Ostergaard, J.; Jorgensen, L.; Jensen, H., Protein adsorption at charged surfaces: the role of electrostatic interactions and interfacial charge regulation. *Langmuir* 2011, 27 (6), 2634-43.

He, K.; Babaye Khorasani, F.; Retterer, S. T.; Thomas, D. K.; Conrad, J. C.; Krishnamoorti, R., Diffusive dynamics of nanoparticles in arrays of nanoposts. *ACS Nano* 2013, 7 (6), 5122-5130.

He, K.; Retterer, S. T.; Srijanto, B. R.; Conrad, J. C.; Krishnamoorti, R., Transport and dispersion of nanoparticles in periodic nanopost arrays. *ACS Nano* 2014, 8 (5), 4221-4227.

Hennings, H.; Michael, D.; Cheng, C.; Steinert, P.; Holbrook, K.; Yuspa, S. H., Calcium regulation of growth and differentiation of mouse epidermal cells in culture. *Cell* 1980, 19 (1), 245-254.

Henry, C.; Minier, J.-P.; Lefèvre, G., Towards a description of particulate fouling: From single particle deposition to clogging. *Adv. colloid interface sci.* 2012, 185, 34-76.

Herold, C.; Schwille, P.; Petrov, E. P., DNA condensation at freestanding cationic lipid bilayers. *Phys. Rev. Lett.* 2010, 104 (14), 148102.

Herrera, E.; Giacomelli, C. E., Surface coverage dictates the surface bio-activity of D-amino acid oxidase. *Colloids Surf., B* 2014, 117, 296-302.

Hideshima, S.; Sato, R.; Inoue, S.; Kuroiwa, S.; Osaka, T., Detection of tumor marker in blood serum using antibody-modified field effect transistor with optimized BSA blocking. *Sens. Actuators, B* 2012, 161 (1), 146-150.

Hiemenz, P. C.; Hiemenz, P. C., Principles of colloid and surface chemistry. M. Dekker New York: 1986; Vol. 9.

Ho, C.-C.; Zydney, A. L., A combined pore blockage and cake filtration model for protein fouling during microfiltration. *J. Colloid Interface Sci.* 2000, 232 (2), 389-399.

Honciuc, A.; Harant, A. W.; Schwartz, D. K., Single-molecule observations of surfactant diffusion at the solution-solid interface. *Langmuir* 2008, 24, 6562-6566.

Honciuc, A.; Harant, A. W.; Schwartz, D. K., Single-molecule observations of surfactant diffusion at the solution– solid interface. *Langmuir* 2008, 24 (13), 6562-6566.

Hou, S. H.; Zhao, J.; Ellman, C. F.; Hu, J.; Griffin, Z.; Spiegel, D. M.; Bourdeau, J. E., Calcium and phosphorus fluxes during hemodialysis with low calcium dialysate. *Am. J. Kidney Dis.* 1991, 18 (2), 217-224.

Hsieh, H. Y.; Wang, P. C.; Wu, C. L.; Huang, C. W.; Chieng, C. C.; Tseng, F. G., Effective enhancement of fluorescence detection efficiency in protein microarray assays: application of a highly fluorinated organosilane as the blocking agent on the background surface by a facile vapor-phase deposition process. *Anal. Chem.* 2009, 81 (19), 7908-16.

Iritani, E.; Katagiri, N.; Yamashita, Y., Effect of membrane morphology on rising properties of filtration resistance in microfiltration of dilute colloids. *AIChE Journal* 2017.

Isaienko, O.; Borguet, E., Hydrophobicity of Hydroxylated Amorphous Fused Silica Surfaces. *Langmuir* 2013, 29 (25), 7885-7895.

Jacob, J. D. C.; He, K.; Retterer, S. T.; Krishnamoorti, R.; Conrad, J. C., Diffusive dynamics of nanoparticles in ultra-confined media. *Soft Matter* 2015, 11 (38), 7515-7524.

Jager, M.; Nir, E.; Weiss, S., Site-specific labeling of proteins for single-molecule FRET by combining chemical and enzymatic modification. *Protein Sci.* 2006, 15 (3), 640-6.

Janna, W. S., Introduction to fluid mechanics. CRC press: 2009.

Jiang, L.; Granick, S., Real-space, in situ maps of hydrogel pores. *ACS Nano* 2016, 11 (1), 204-212.

Johnson, N. L.; Kotz, S.; Balakrishnan, N., Continuous univariate distributions. John Wiley & Sons: New York, 1994.

Kang, S. H.; Yeung, E. S., Dynamics of Single-Protein Molecules at a Liquid/Solid Interface: Implications in Capillary Electrophoresis and Chromatography. *Anal. Chem.* 2002, 74 (24), 6334-6339.

Kastantin, M.; Schwartz, D. K., Connecting Rare DNA Conformations and Surface Dynamics Using Single-Molecule Resonance Energy Transfer. *ACS Nano* 2011, 5 (12), 9861-9869.

Kastantin, M.; Schwartz, D. K., Identifying multiple populations from single-molecule lifetime distributions. *Chemphyschem* 2013, 14 (2), 374-80.

Kidoaki, S.; Matsuda, T., Adhesion forces of the blood plasma proteins on self-assembled monolayer surfaces of alkanethiolates with different functional groups measured by an atomic force microscope. *Langmuir* 1999, 15 (22), 7639-7646.

Kim, J.; Somorjai, G. A., Molecular packing of lysozyme, fibrinogen, and bovine serum albumin on hydrophilic and hydrophobic surfaces studied by infrared-visible sum frequency generation and fluorescence microscopy. *J. Am. Chem. Soc.* 2003, 125 (10), 3150-3158.

Kim, S. A.; Tai, C.-Y.; Mok, L.-P.; Mosser, E. A.; Schuman, E. M., Calcium-dependent dynamics of cadherin interactions at cell–cell junctions. *Proceedings of the National Academy of Sciences* 2011, 108 (24), 9857-9862.

Kim, S. A.; Tai, C.-Y.; Mok, L.-P.; Mosser, E. A.; Schuman, E. M., Calcium-dependent dynamics of cadherin interactions at cell–cell junctions. *Proc. Natl. Acad. Sci. U. S. A.* 2011, 108 (24), 9857-9862.

Kiselev, M. A.; Gryzunov, I. A.; Dobretsov, G. E.; Komarova, M. N., Size of Human Serum Albumin in Solution. *Biofizika* 2000, 46, 423-427.

Kisley, L.; Chen, J.; Mansur, A. P.; Dominguez-Medina, S.; Kulla, E.; Kang, M. K.; Shuang, B.; Kourentzi, K.; Poongavanam, M. V.; Dhamane, S.; Willson, R. C.; Landes, C. F., High ionic strength narrows the population of sites participating in protein ion-exchange adsorption: a single-molecule study. *J. Chromatogr. A* 2014, 1343, 135-42.

Kisley, L.; Chen, J.; Mansur, A. P.; Shuang, B.; Kourentzi, K.; Poongavanam, M. V.; Chen, W. H.; Dhamane, S.; Willson, R. C.; Landes, C. F., Unified superresolution experiments and stochastic theory provide mechanistic insight into protein ion-exchange adsorptive separations. *Proc. Natl. Acad. Sci. U. S. A.* 2014, 111 (6), 2075-80.

Knight, J. D.; Lerner, M. G.; Marcano-Velázquez, J. G.; Pastor, R. W.; Falke, J. J., Single molecule diffusion of membrane-bound proteins: window into lipid contacts and bilayer dynamics. *Biophys. J.* 2010, 99 (9), 2879-2887.

Knight, J. D.; Lerner, M. G.; Marcano-Velázquez, J. G.; Pastor, R. W.; Falke, J. J., Single molecule diffusion of membrane-bound proteins: window into lipid contacts and bilayer dynamics. *Biophysical journal* 2010, 99 (9), 2879-2887.

Koch, A. W.; Pokutta, S.; Lustig, A.; Engel, J., Calcium binding and homoassociation of E-cadherin domains. *Biochemistry* 1997, 36 (25), 7697-7705.

Koltover, I.; Salditt, T.; Safinya, C., Phase diagram, stability, and overcharging of lamellar cationic lipid–DNA self-assembled complexes. *Biophys. J.* 1999, 77 (2), 915-924.

Kong, C. S.; Kim, D.-Y.; Lee, H.-K.; Shul, Y.-G.; Lee, T.-H., Influence of pore-size distribution of diffusion layer on mass-transport problems of proton exchange membrane fuel cells. *J. Power Sources* 2002, 108 (1-2), 185-191.

Koponen, A.; Kataja, M.; Timonen, J., Tortuous flow in porous media. *Phys. Rev. E* 1996, 54 (1), 406-410.

Krisdhasima, V.; McGuire, J.; Sproull, R., Surface hydrophobic influences on β -lactoglobulin adsorption kinetics. *J. Colloid Interface Sci.* 1992, 154 (2), 337-350.

Kurrat, R.; Prenosil, J.; Ramsden, J., Kinetics of human and bovine serum albumin adsorption at silica–titania surfaces. *J. Colloid Interface Sci.* 1997, 185 (1), 1-8.

Kusumi, A.; Sako, Y.; Yamamoto, M., Confined lateral diffusion of membrane receptors as studied by single particle tracking (nanovid microscopy). Effects of calcium-induced differentiation in cultured epithelial cells. *Biophys. J.* 1993, 65 (5), 2021-2040.

Lambert, O.; Taveau, J.-C.; Him, J. L. K.; Al Kurdi, R.; Gulino-Debrac, D.; Brisson, A., The basic framework of VE-cadherin junctions revealed by cryo-EM. *J. Mol. Biol.* 2005, 346 (5), 1193-1196.

Landesfeind, J.; Hattendorff, J.; Ehrl, A.; Wall, W. A.; Gasteiger, H. A., Tortuosity determination of battery electrodes and separators by impedance spectroscopy. *J. Electrochem. Soc.* 2016, 163 (7), A1373-A1387.

Langdon, B. B.; Kastantin, M.; Schwartz, D. K., Surface Chemistry Influences Interfacial Fibrinogen Self-Association. *Biomacromolecules* 2015, 16, 3201-3208.

Langdon, B. B.; Kastantin, M.; Walder, R.; Schwartz, D. K., Interfacial protein-protein associations. *Biomacromolecules* 2014, 15 (1), 66-74.

Langdon, B. B.; Mirhossaini, R. B.; Mabry, J. N.; Sriram, I.; Lajmi, A.; Zhang, Y.; Rojas, O. J.; Schwartz, D. K., Single-molecule resolution of protein dynamics on polymeric membrane surfaces: the roles of spatial and population heterogeneity. *ACS Appl. Mater. Interfaces* 2015, 7 (6), 3607-17.

Leckband, D.; de Rooij, J., Cadherin adhesion and mechanotransduction. *Annual review of cell and developmental biology* 2014, 30, 291-315.

Leckband, D.; de Rooij, J., Cadherin adhesion and mechanotransduction. *Annu. Rev. Cell Dev. Biol.* 2014, 30, 291-315.

Leckband, D.; Prakasam, A., Mechanism and dynamics of cadherin adhesion. *Annu. Rev. Biomed. Eng.* 2006, 8, 259-287.

Lee, J.-K.; Liu, B. Y., An experimental study of particulate retention by microporous membranes in liquid filtration. *KSME J.* 1994, 8 (1), 69-77.

Lee, S.; Park, G.; Amy, G.; Hong, S.-K.; Moon, S.-H.; Lee, D.-H.; Cho, J., Determination of membrane pore size distribution using the fractional rejection of nonionic and charged macromolecules. *J. Membr. Sci.* 2002, 201 (1-2), 191-201.

Lee, Y.; Andrade Jr, J. S.; Buldyrev, S. V.; Dokholyan, N. V.; Havlin, S.; King, P. R.; Paul, G.; Stanley, H. E., Traveling time and traveling length in critical percolation clusters. *Phys. Rev. E* 1999, 60 (3), 3425.

- Levitz, P., Off-lattice reconstruction of porous media: critical evaluation, geometrical confinement and molecular transport. *Adv. Colloid Interface Sci.* 1998, 76, 71-106.
- Lhoest, J. B.; Detrait, E.; Van Den Bosch De Aguilar, P.; Bertrand, P., Fibronectin adsorption, conformation, and orientation on polystyrene substrates studied by radiolabeling, XPS, and ToF SIMS. *J. Biomed. Mater. Res.* 1998, 41 (1), 95-103.
- Li, L.; Qian, Y.; Jiang, C.; Lv, Y.; Liu, W.; Zhong, L.; Cai, K.; Li, S.; Yang, L., The use of hyaluronan to regulate protein adsorption and cell infiltration in nanofibrous scaffolds. *Biomaterials* 2012, 33 (12), 3428-45.
- Lindquist, E. D.; Norman, W. R.; Soerens, T., A review of: Fouling in hollow fiber membrane microfilters used for household water treatment. *J. Water, Sanit. Hyg. Dev.* 2015, 5 (2), 229-231.
- Liu, Y.; Hu, E.; Khan, E. A.; Lai, Z., Synthesis and characterization of ZIF-69 membranes and separation for CO₂/CO mixture. *J. Membr. Sci.* 2010, 353 (1), 36-40.
- Ljunglof, A.; Hjorth, R., Confocal microscopy as a tool for studying protein adsorption to chromatographic matrices. *J. Chromatogr. A* 1996, 743, 75-83.
- Lohaus, J.; Perez, Y.; Wessling, M., What are the microscopic events of colloidal membrane fouling? *J. Membr. Sci.* 2018.
- Lu, M.; Chai, J.; Fu, D., Structural basis for autoregulation of the zinc transporter YiiP. *Nat. Struct. Mol. Biol.* 2009, 16 (10), 1063-7.
- Luey, J.-K.; McGuire, J.; Sproull, R. D., The effect of pH and NaCl concentration on adsorption of β -lactoglobulin at hydrophilic and hydrophobic silicon surfaces. *J. Colloid Interface Sci.* 1991, 143 (2), 489-500.
- Luik, A.; Naboka, Y. N.; Mogilevich, S.; Hushcha, T.; Mischenko, N., Study of human serum albumin structure by dynamic light scattering: two types of reactions under different pH and interaction with physiologically active compounds. *Spectrochim. Acta Mol. Biomol. Spectrosc.* 1998, 54 (10), 1503-1507.
- Ma, H.; Hyun, J.; Stiller, P.; Chilkoti, A., "Non-Fouling" Oligo (ethylene glycol)-Functionalized Polymer Brushes Synthesized by Surface-Initiated Atom Transfer Radical Polymerization. *Adv. Mater.* 2004, 16 (4), 338-341.

Mabry, J. N.; Skaug, M. J.; Schwartz, D. K., Single-molecule insights into retention at a reversed-phase chromatographic interface. *Anal. Chem.* 2014, 86 (19), 9451-8.

Majumdar, D. S.; Smirnova, I.; Kasho, V.; Nir, E.; Kong, X.; Weiss, S.; Kaback, H. R., Single-molecule FRET reveals sugar-induced conformational dynamics in LacY. *Proc. Natl. Acad. Sci. U. S. A.* 2007, 104 (31), 12640-5.

Marchesi, V.; Tillack, T.; Jackson, R.; Segrest, J.; Scott, R., Chemical characterization and surface orientation of the major glycoprotein of the human erythrocyte membrane. *Proc. Natl. Acad. Sci. U. S. A.* 1972, 69 (6), 1445-1449.

Marsh, D., Intrinsic curvature in normal and inverted lipid structures and in membranes. *Biophys. J.* 1996, 70 (5), 2248.

Maruyama, T.; Katoh, S.; Nakajima, M.; Nabetani, H., Mechanism of bovine serum albumin aggregation during ultrafiltration. *Biotechnology and bioengineering* 2001, 75 (2), 233-238.

Maurer, P.; Hohenester, E.; Engel, J., Extracellular calcium-binding proteins. *Current opinion in cell biology* 1996, 8 (5), 609-617.

Maurer, P.; Hohenester, E.; Engel, J., Extracellular calcium-binding proteins. *Curr. Opin. Cell Biol.* 1996, 8 (5), 609-617.

McClellan, S. J.; Franses, E. I., Effect of concentration and denaturation on adsorption and surface tension of bovine serum albumin. *Colloids Surf., B* 2003, 28 (1), 63-75.

McDowell-Boyer, L. M.; Hunt, J. R.; Sitar, N., Particle transport through porous media. *Water Resour. Res.* 1986, 22 (13), 1901-1921.

McUmbler, A. C.; Randolph, T. W.; Schwartz, D. K., Electrostatic Interactions Influence Protein Adsorption (but Not Desorption) at the Silica-Aqueous Interface. *J. Phys. Chem. Lett.* 2015, 6 (13), 2583-7.

Meng, F.; Chae, S.-R.; Drews, A.; Kraume, M.; Shin, H.-S.; Yang, F., Recent advances in membrane bioreactors (MBRs): membrane fouling and membrane material. *Water Res.* 2009, 43 (6), 1489-1512.

Meyer, D. W.; Bijeljic, B., Pore-scale dispersion: Bridging the gap between microscopic pore structure and the emerging macroscopic transport behavior. *Phys. Rev. E* 2016, 94 (1), 013107.

Miller-Jaster, K. N.; Petrie Aronin, C. E.; Guilford, W. H., A Quantitative Comparison of Blocking Agents in the In Vitro Motility Assay. *Cell. Mol. Bioeng.* 2011, 5 (1), 44-51.

Miller, D. J.; Kasemset, S.; Paul, D. R.; Freeman, B. D., Comparison of membrane fouling at constant flux and constant transmembrane pressure conditions. *J. Membr. Sci.* 2014, 454, 505-515.

Milling, A.; Mulvaney, P.; Larson, I., Direct measurement of repulsive van der Waals interactions using an atomic force microscope. *J. Colloid Interface Sci.* 1996, 180 (2), 460-465.

Minchinton, A. I.; Tannock, I. F., Drug penetration in solid tumours. *Nat. rev., Cancer* 2006, 6 (8), 583-592.

Minton, A. P., Effects of excluded surface area and adsorbate clustering on surface adsorption of proteins: I. Equilibrium models. *Biophys. Chem.* 2000, 86 (2), 239-247.

Modi, S.; M, G. S.; Goswami, D.; Gupta, G. D.; Mayor, S.; Krishnan, Y., A DNA nanomachine that maps spatial and temporal pH changes inside living cells. *Nat. Nanotechnol.* 2009, 4 (5), 325-30.

Möller, C.; Allen, M.; Elings, V.; Engel, A.; Müller, D. J., Tapping-mode atomic force microscopy produces faithful high-resolution images of protein surfaces. *Biophys. J.* 1999, 77 (2), 1150-1158.

Monserud, J. H.; Schwartz, D. K., Effects of molecular size and surface hydrophobicity on oligonucleotide interfacial dynamics. *Biomacromolecules* 2012, 13 (12), 4002-4011.

Moore, E. W., Ionized calcium in normal serum, ultrafiltrates, and whole blood determined by ion-exchange electrodes. *J. Clin. Invest.* 1970, 49 (2), 318.

Morrissey, B. W.; Stromberg, R. R., The conformation of adsorbed blood proteins by infrared bound fraction measurements. *J. Colloid Interface Sci.* 1974, 46 (1), 152-164.

Mulder, J., Basic principles of membrane technology. Springer Science & Business Media: 2012.

Nagar, B.; Overduin, M.; Ikura, M.; Rini, J. M., Structural basis of calcium-induced E-cadherin rigidification and dimerization. *Nature* 1996.

Nakanishi, K.; Sakiyama, T.; Imamura, K., On the adsorption of proteins on solid surfaces, a common but very complicated phenomenon. *J. Biosci. Bioeng.* 2001, 91 (3), 233-244.

Nakao, S.-i., Determination of pore size and pore size distribution: 3. Filtration membranes. *J. Membr. Sci.* 1994, 96 (1-2), 131-165.

Nicholson, C.; Ten Bruggencate, G.; Stockle, H.; Steinberg, R., Calcium and potassium changes in extracellular microenvironment of cat cerebellar cortex. *J. Neurophysiol.* 1978, 41 (4), 1026-1039.

Nicolay, K.; Braun, K. P.; Graaf, R. A. d.; Dijkhuizen, R. M.; Kruiskamp, M. J., Diffusion NMR spectroscopy. *NMR Biomed.* 2001, 14 (2), 94-111.

Nikiforov, T. T.; Beechem, J. M., Development of homogeneous binding assays based on fluorescence resonance energy transfer between quantum dots and Alexa Fluor fluorophores. *Anal. Biochem.* 2006, 357 (1), 68-76.

Nygren, H.; Alaeddin, S.; Lundström, I.; Magnusson, K.-E., Effect of surface wettability on protein adsorption and lateral diffusion. Analysis of data and a statistical model. *Biophys. Chem.* 1994, 49 (3), 263-272.

O'Melia, C. R., Particles, pretreatment, and performance in water filtration. *J. Environ. Eng.* 1985, 111 (6), 874-890.

Oliva, F. Y.; Avalle, L. B.; Cámara, O. R.; De Pauli, C. P., Adsorption of human serum albumin (HSA) onto colloidal TiO₂ particles, Part I. *J. Colloid Interface Sci.* 2003, 261 (2), 299-311.

Parlett, C. M.; Wilson, K.; Lee, A. F., Hierarchical porous materials: catalytic applications. *Chem. Soc. Rev.* 2013, 42 (9), 3876-3893.

Pavani, S. R. P.; Thompson, M. A.; Biteen, J. S.; Lord, S. J.; Liu, N.; Twieg, R. J.; Piestun, R.; Moerner, W., Three-dimensional, single-molecule fluorescence imaging beyond the diffraction limit by using a double-helix point spread function. *Proc. Natl. Acad. Sci.* 2009, 106 (9), 2995-2999.

Pertz, O.; Bozic, D.; Koch, A. W.; Fauser, C.; Brancaccio, A.; Engel, J., A new crystal structure, Ca²⁺ dependence and mutational analysis reveal molecular details of E-cadherin homoassociation. *EMBO J.* 1999, 18 (7), 1738-1747.

Pertz, O.; Bozic, D.; Koch, A. W.; Fauser, C.; Brancaccio, A.; Engel, J., A new crystal structure, Ca²⁺ dependence and mutational analysis reveal molecular details of E-cadherin homoassociation. *The EMBO journal* 1999, 18 (7), 1738-1747.

Podhipleux, N.; Krisdhasima, V.; McGuire, J., Molecular charge effects on protein behavior at hydrophobic and hydrophilic solid surfaces. *Food hydrocolloids* 1996, 10 (3), 285-293.

Pokutta, S.; Herrenknecht, K.; Kemler, R.; ENGEL, J., Conformational changes of the recombinant extracellular domain of E-cadherin upon calcium binding. *Eur. J. Biochem.* 1994, 223 (3), 1019-1026.

Pokutta, S.; Herrenknecht, K.; Kemler, R.; ENGEL, J., Conformational changes of the recombinant extracellular domain of E-cadherin upon calcium binding. *European journal of biochemistry* 1994, 223 (3), 1019-1026.

Prakasam, A.; Maruthamuthu, V.; Leckband, D., Similarities between heterophilic and homophilic cadherin adhesion. *Proc. Natl. Acad. Sci. USA* 2006, 103 (42), 15434-15439.

Prasad, R.; Sirkar, K., Dispersion-free solvent extraction with microporous hollow-fiber modules. *AIChE J.* 1988, 34 (2), 177-188.

Puddu, V.; Perry, C. C., Peptide Adsorption on Silica Nanoparticles: Evidence of Hydrophobic Interactions. *ACS Nano* 2012, 6 (7), 6356-6363.

Qian, H.; Sheetz, M. P.; Elson, E. L., Single particle tracking. Analysis of diffusion and flow in two-dimensional systems. *Biophys. J.* 1991, 60 (4), 910-921.

Qin, W.; Zhang, J.; Xie, Z.; Ng, D.; Ye, Y.; Gray, S. R.; Xie, M., Synergistic effect of combined colloidal and organic fouling in membrane distillation: Measurements and mechanisms. *Environ. Sci.: Water Res. Technol.* 2017, 3 (1), 119-127.

Rabe, M.; Verdes, D.; Seeger, S., Understanding cooperative protein adsorption events at the microscopic scale: a comparison between experimental data and Monte Carlo simulations. *J. Phys. Chem. B* 2010, 114 (17), 5862-5869.

Rabe, M.; Verdes, D.; Seeger, S., Understanding protein adsorption phenomena at solid surfaces. *Adv. Colloid Interface Sci.* 2011, 162 (1-2), 87-106.

Rabe, M.; Verdes, D.; Zimmermann, J.; Seeger, S., Surface organization and cooperativity during nonspecific protein adsorption events. *J. Phys. Chem. B* 2008, 112 (44), 13971-13980.

Richter, R. P.; Bérat, R.; Brisson, A. R., Formation of solid-supported lipid bilayers: an integrated view. *Langmuir* 2006, 22 (8), 3497-3505.

Rimola, A.; Costa, D.; Sodupe, M.; Lambert, J. F.; Ugliengo, P., Silica surface features and their role in the adsorption of biomolecules: computational modeling and experiments. *Chem. Rev.* 2013, 113 (6), 4216-313.

Roach, L. S.; Song, H.; Ismagilov, R. F., Controlling nonspecific protein adsorption in a plug-based microfluidic system by controlling interfacial chemistry using fluorosurfactants. *Analytical chemistry* 2005, 77 (3), 785-796.

Roach, P.; Farrar, D.; Perry, C. C., Interpretation of protein adsorption: surface-induced conformational changes. *J. Am. Chem. Soc.* 2005, 127 (22), 8168-73.

San Paulo, A.; García, R., Tip-surface forces, amplitude, and energy dissipation in amplitude-modulation (tapping mode) force microscopy. *Phys. Rev. B* 2001, 64 (19), 193411.

Saxena, A.; Tripathi, B. P.; Kumar, M.; Shahi, V. K., Membrane-based techniques for the separation and purification of proteins: an overview. *Adv. Colloid Interface Sci.* 2009, 145 (1-2), 1-22.

Saxton, M. J., Single-particle tracking: the distribution of diffusion coefficients. *Biophys. J.* 1997, 72 (4), 1744.

Sengupta, P.; Jovanovic-Talisman, T.; Skoko, D.; Renz, M.; Veatch, S. L.; Lippincott-Schwartz, J., Probing protein heterogeneity in the plasma membrane using PALM and pair correlation analysis. *Nat. Methods* 2011, 8 (11), 969-75.

Sethuraman, A.; Belfort, G., Protein structural perturbation and aggregation on homogeneous surfaces. *Biophys. J.* 2005, 88 (2), 1322-33.

Shannon, M. A.; Bohn, P. W.; Elimelech, M.; Georgiadis, J. G.; Mariñas, B. J.; Mayes, A. M., Science and technology for water purification in the coming decades. *Nature* 2008, 452 (7185), 301-310.

Shen, L.; Chen, Z., Critical review of the impact of tortuosity on diffusion. *Chem. Eng. Sci.* 2007, 62 (14), 3748-3755.

Shiddiky, M. J.; Kithva, P. H.; Kozak, D.; Trau, M., An electrochemical immunosensor to minimize the nonspecific adsorption and to improve sensitivity of protein assays in human serum. *Biosens. Bioelectron.* 2012, 38 (1), 132-7.

- Sindorf, D. W.; Maciel, G. E., Solid-state NMR studies of the reactions of silica surfaces with polyfunctional chloromethylsilanes and ethoxymethylsilanes. *J. Am. Chem. Soc.* 1983, 105 (12), 3767-3776.
- Sivasankar, S.; Briehar, W.; Lavrik, N.; Gumbiner, B.; Leckband, D., Direct molecular force measurements of multiple adhesive interactions between cadherin ectodomains. *Proc. Natl. Acad. Sci. USA* 1999, 96 (21), 11820-11824.
- Skaug, M. J.; Schwartz, D. K., Tracking nanoparticle diffusion in porous filtration media. *Ind. Eng. Chem. Res.* 2015, 54 (16), 4414-4419.
- Skaug, M. J.; Wang, L.; Ding, Y.; Schwartz, D. K., Hindered nanoparticle diffusion and void accessibility in a three-dimensional porous medium. *ACS Nano* 2015, 9 (2), 2148-2156.
- Sotomayor, M.; Schulten, K., The allosteric role of the Ca²⁺ switch in adhesion and elasticity of C-cadherin. *Biophys. J.* 2008, 94 (12), 4621-4633.
- Stevenson, D., Flow and filtration through granular media—The effect of grain and particle size dispersion. *Water Res.* 1997, 31 (2), 310-322.
- Stradner, A.; Sedgwick, H.; Cardinaux, F.; Poon, W. C. K.; Egelhaaf, S. U.; Schurtenberger, P., Equilibrium cluster formation in concentrated protein solutions and colloids. *Nature* 2004, 432, 492-495.
- Suman, R.; Ruth, D., Formation factor and tortuosity of homogeneous porous media. *Transport Porous Med.* 1993, 12 (2), 185-206.
- Sun, S.; Yue, Y.; Huang, X.; Meng, D., Protein adsorption on blood-contact membranes. *J. Membr. Sci.* 2003, 222 (1-2), 3-18.
- Takeichi, M., Cadherin cell adhesion receptors as a morphogenetic regulator. *Science* 1991, 251 (5000), 1451-1455.
- Talasaz, A. H.; Nemat-Gorgani, M.; Liu, Y.; Ståhl, P.; Dutton, R. W.; Ronaghi, M.; Davis, R. W., Prediction of protein orientation upon immobilization on biological and nonbiological surfaces. *Proc. Natl. Acad. Sci. U. S. A.* 2006, 103 (40), 14773-14778.
- Tauzin, L. J.; Shuang, B.; Kisley, L.; Mansur, A. P.; Chen, J.; de Leon, A.; Advincula, R. C.; Landes, C. F., Charge-dependent transport switching of single molecular ions in a weak polyelectrolyte multilayer. *Langmuir* 2014, 30 (28), 8391-9.

Thakur, G.; Jiang, K.; Lee, D.; Prashanthi, K.; Kim, S.; Thundat, T., Investigation of pH-induced protein conformation changes by nanomechanical deflection. *Langmuir* 2014, 30 (8), 2109-16.

Thompson, M. A.; Lew, M. D.; Badieirostami, M.; Moerner, W., Localizing and tracking single nanoscale emitters in three dimensions with high spatiotemporal resolution using a double-helix point spread function. *Nano Lett.* 2009, 10 (1), 211-218.

Tie, Y.; Calonder, C.; Van Tassel, P. R., Protein adsorption: kinetics and history dependence. *J. Colloid Interface Sci.* 2003, 268 (1), 1-11.

Tsukruk, V. V.; Bliznyuk, V. N., Adhesive and friction forces between chemically modified silicon and silicon nitride surfaces. *Langmuir* 1998, 14 (2), 446-455.

Tufenkji, N.; Elimelech, M., Correlation equation for predicting single-collector efficiency in physicochemical filtration in saturated porous media. *Environ. Sci. Technol.* 2004, 38 (2), 529-536.

Vallabh, R.; Banks-Lee, P.; Seyam, A.-F., New approach for determining tortuosity in fibrous porous media. *J. Eng. Fiber Fabr.* 2010, 5 (3), 7-19.

Van Deemter, J. J.; Zuiderweg, F.; Klinkenberg, A. v., Longitudinal diffusion and resistance to mass transfer as causes of nonideality in chromatography. *Chem. Eng. Sci.* 1956, 5 (6), 271-289.

van Reis, R.; Zydney, A., Bioprocess membrane technology. *J. Membr. Sci.* 2007, 297 (1), 16-50.

Vasina, E. N.; Déjardin, P.; Rezaei, H.; Grosclaude, J.; Quiquampoix, H., Fate of prions in soil: Adsorption kinetics of recombinant unglycosylated ovine prion protein onto mica in laminar flow conditions and subsequent desorption. *Biomacromolecules* 2005, 6 (6), 3425-3432.

Vervoort, R.; Cattle, S., Linking hydraulic conductivity and tortuosity parameters to pore space geometry and pore-size distribution. *J. Hydrol.* 2003, 272 (1), 36-49.

Viegas, R.; Rodriguez, M.; Luque, S.; Alvarez, J.; Coelho, I.; Crespo, J., Mass transfer correlations in membrane extraction: analysis of Wilson-plot methodology. *J. Membr. Sci.* 1998, 145 (1), 129-142.

Vunnam, N.; Pedigo, S., Sequential binding of calcium leads to dimerization in neural cadherin. *Biochemistry* 2011, 50 (14), 2973-2982.

Walder, R.; Nelson, N.; Schwartz, D. K., Super-resolution surface mapping using the trajectories of molecular probes. *Nat. Commun.* 2011, 2, 515.

Wang, D.; He, C.; Stoykovich, M. P.; Schwartz, D. K., Nanoscale Topography Influences Polymer Surface Diffusion. *ACS Nano* 2015, 9 (2), 1656-1664.

Wang, D.; Hu, R.; Mabry, J. N.; Miao, B.; Wu, D. T.; Koynov, K.; Schwartz, D. K., Scaling of Polymer Dynamics at an Oil-Water Interface in Regimes Dominated by Viscous Drag and Desorption-Mediated Flights. *J. Am. Chem. Soc.* 2015, 137, 12312-12320.

Wang, D.; Hu, R.; Mabry, J. N.; Miao, B.; Wu, D. T.; Koynov, K.; Schwartz, D. K., Scaling of Polymer Dynamics at an Oil–Water Interface in Regimes Dominated by Viscous Drag and Desorption-Mediated Flights. *J. Am. Chem. Soc.* 2015, 137 (38), 12312-12320.

Wang, F.; Tarabara, V. V., Pore blocking mechanisms during early stages of membrane fouling by colloids. *J. Colloid Interface Sci.* 2008, 328 (2), 464-9.

Wang, G.; Coppens, M.-O., Rational design of hierarchically structured porous catalysts for autothermal reforming of methane. *Chem. Eng. Sci.* 2010, 65 (7), 2344-2351.

Wang, J. S.; Brown, G. J.; Hung, W. C.; Wai, C. M., Supercritical fluid deposition of uniform PbS nanoparticle films for energy-transfer studies. *Chemphyschem* 2012, 13 (8), 2068-73.

Wang, L.; Cai, Y.; Jing, Y.; Zhu, B.; Zhu, L.; Xu, Y., Route to hemocompatible polyethersulfone membranes via surface aminolysis and heparinization. *J. Colloid Interface Sci.* 2014, 422, 38-44.

Wang, M. S.; Palmer, L. B.; Schwartz, J. D.; Razatos, A., Evaluating protein attraction and adhesion to biomaterials with the atomic force microscope. *Langmuir* 2004, 20 (18), 7753-7759.

Wang, S.; Yong, W.; Liu, J.; Zhang, L.; Chen, Q.; Dong, Y., Development of an indirect competitive assay-based aptasensor for highly sensitive detection of tetracycline residue in honey. *Biosens. Bioelectron.* 2014, 57, 192-8.

Wang, Y.; Zhu, J.; Huang, H.; Cho, H.-H., Carbon nanotube composite membranes for microfiltration of pharmaceuticals and personal care products: Capabilities and potential mechanisms. *J. Membr. Sci.* 2015, 479, 165-174.

Watson, D. S.; Kerchner, K. R.; Gant, S. S.; Pedersen, J. W.; Hamburger, J. B.; Ortigosa, A. D.; Potgieter, T. I., At-line process analytical technology (PAT) for more efficient scale up of biopharmaceutical microfiltration unit operations. *Biotechnol. Prog.* 2016, 32 (1), 108-115.

White, F. M.; Corfield, I., Viscous fluid flow. McGraw-Hill Higher Education Boston: 2006; Vol. 3.

Wiederseiner, S.; Andreini, N.; Epely-Chauvin, G.; Ancey, C., Refractive-index and density matching in concentrated particle suspensions: a review. *Exp. Fluids* 2011, 50 (5), 1183-1206.

Wiest, M. C.; Eagleman, D. M.; King, R. D.; Montague, P. R., Dendritic spikes and their influence on extracellular calcium signaling. *Journal of neurophysiology* 2000, 83 (3), 1329-1337.

Wong, S. Y.; Han, L.; Timachova, K.; Veselinovic, J.; Hyder, M. N.; Ortiz, C.; Klibanov, A. M.; Hammond, P. T., Drastically lowered protein adsorption on microbicidal hydrophobic/hydrophilic polyelectrolyte multilayers. *Biomacromolecules* 2012, 13 (3), 719-26.

Wong, T.-S.; Kang, S. H.; Tang, S. K.; Smythe, E. J.; Hatton, B. D.; Grinthal, A.; Aizenberg, J., Bioinspired self-repairing slippery surfaces with pressure-stable omniphobicity. *Nature* 2011, 477 (7365), 443-447.

Wu, Y.; Jin, X.; Harrison, O.; Shapiro, L.; Honig, B. H.; Ben-Shaul, A., Cooperativity between trans and cis interactions in cadherin-mediated junction formation. *Proc. Natl. Acad. Sci. USA* 2010, 107 (41), 17592-17597.

Wu, Y.; Jin, X.; Harrison, O.; Shapiro, L.; Honig, B. H.; Ben-Shaul, A., Cooperativity between trans and cis interactions in cadherin-mediated junction formation. *Proceedings of the National Academy of Sciences* 2010, 107 (41), 17592-17597.

Xiao, Y.; Isaacs, S. N., Enzyme-linked immunosorbent assay (ELISA) and blocking with bovine serum albumin (BSA)--not all BSAs are alike. *J. Immunol. Methods* 2012, 384 (1-2), 148-51.

Xie, Z.; Srividya, N.; Sosnick, T. R.; Pan, T.; Scherer, N. F., Single-molecule studies highlight conformational heterogeneity in the early folding steps of a large ribozyme. *Proc. Natl. Acad. Sci. U. S. A.* 2004, 101 (2), 534-9.

Yang, D.; Lu, X.; Hong, Y.; Xi, T.; Zhang, D., The molecular mechanism of mediation of adsorbed serum proteins to endothelial cells adhesion and growth on biomaterials. *Biomaterials* 2013, 34 (23), 5747-58.

Yuspa, S. H.; Koehler, B.; Kulesz-Martin, M.; Hennings, H., Clonal growth of mouse epidermal cells in medium with reduced calcium concentration. *J. Invest. Dermatol.* 1981, 76 (2), 144-146.

Zhang, B.; Wang, X.; Liu, F.; Cheng, Y.; Shi, D., Effective reduction of nonspecific binding by surface engineering of quantum dots with bovine serum albumin for cell-targeted imaging. *Langmuir* 2012, 28 (48), 16605-13.

Zhang, X.; Niu, L.; Yu, S.; Li, F.; Zhao, X.; Hu, H., Influence of low-level anionic surfactant on PES ultrafiltration performance: membrane fouling and rejection of nuclides. *Water, Air, & Soil Pollution* 2016, 227 (8), 274.

Zhao, J.; Granick, S., How polymer surface diffusion depends on surface coverage. *Macromolecules* 2007, 40, 1243-1247.

Zhao, J.; Granick, S., Polymer Lateral Diffusion at the Solid-Liquid Interface. *J. Am. Chem. Soc.* 2004, 126, 6242-6243.

Zheng, J.; Li, L.; Chen, S.; Jiang, S., Molecular simulation study of water interactions with oligo (ethylene glycol)-terminated alkanethiol self-assembled monolayers. *Langmuir* 2004, 20 (20), 8931-8938.

Zhuravlev, L., The surface chemistry of amorphous silica. Zhuravlev model. *Colloids Surf., A* 2000, 173 (1), 1-38.

Ziemba, B. P.; Knight, J. D.; Falke, J. J., Assembly of membrane-bound protein complexes: detection and analysis by single molecule diffusion. *Biochemistry* 2012, 51 (8), 1638-1647.

Ziemba, B. P.; Li, J.; Landgraf, K. E.; Knight, J. D.; Voth, G. A.; Falke, J. J., Single-molecule studies reveal a hidden key step in the activation mechanism of membrane-bound protein kinase C- α . *Biochemistry* 2014, 53 (10), 1697-1713.

Appendix A: Supporting Information for Chapter 2

A.1 SUPPLEMENTARY TABLE

Table A-2. The fitting parameters of f (site fractions) and λ (characteristic number of adsorption events) from a Poisson mixture model of HSA adsorption on TMS, FS, OEG and NH₂ surfaces at different area fractions. Numbers in parentheses represent the experimental uncertainties in the last digit.

Surface	F_{HSA}	Strong Sites		Weak Sites	
		f	λ	f	λ
TMS	$\sim 10^{-6}$	0.19 (2)	9.2 (9)	0.80 (3)	0.19 (4)
TMS	~ 1	0.017 (8)	3.3 (3)	0.980 (1)	0.20 (2)
FS	$\sim 10^{-6}$	0.18 (1)	12.1 (8)	0.810 (9)	0.097 (9)
FS	~ 1	0.079 (6)	6.2 (3)	0.920 (6)	0.076 (7)
OEG	$\sim 10^{-6}$	0.084(3)	6.1(2)	0.915(4)	0.13(1)
OEG	~ 1	0.018(2)	4.4(3)	0.982(2)	0.24(1)
NH ₂	$\sim 10^{-6}$	0.14 (1)	14.6 (6)	0.850 (4)	0.12 (1)
NH ₂	$\sim 10^{-5}$	0.060(4)	13.7(9)	0.94 (4)	0.19 (3)
NH ₂	$\sim 10^{-4}$	0.003 (1)	4.2 (3)	0.990 (3)	0.28 (6)
NH ₂	$\sim 10^{-3}$	0.19 (3)	12.4 (4)	0.81 (3)	0.33 (5)
NH ₂	~ 1	0.17 (2)	13.8 (9)	0.82 (1)	0.37 (2)

A.2 SUPPLEMENTARY FIGURES

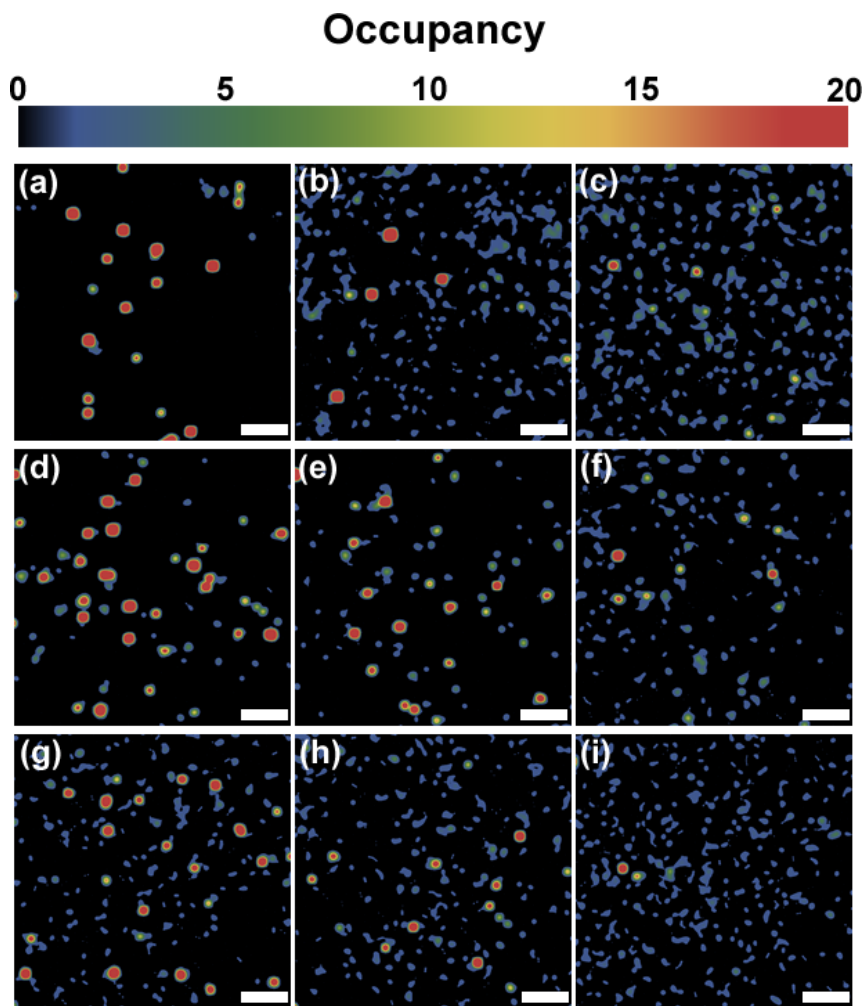


Figure A-1. Representative super-resolution occupancy maps of HSA on (a-c) TMS, (d-f) FS and (g-i) OEG surfaces at very low HSA area fraction ($\sim 10^{-6}$, panels a, d and g), intermediate area fraction ($\sim 10^{-3}$, panels b, e and h) and high area fraction (~ 1 , panels c, f and i). Sites were Gaussian blurred. Scale bar = 2 μm . The strong retention sites on the occupancy maps were largely the same as the strong adsorption sites on the adsorption maps in the main text in Chapter 2.

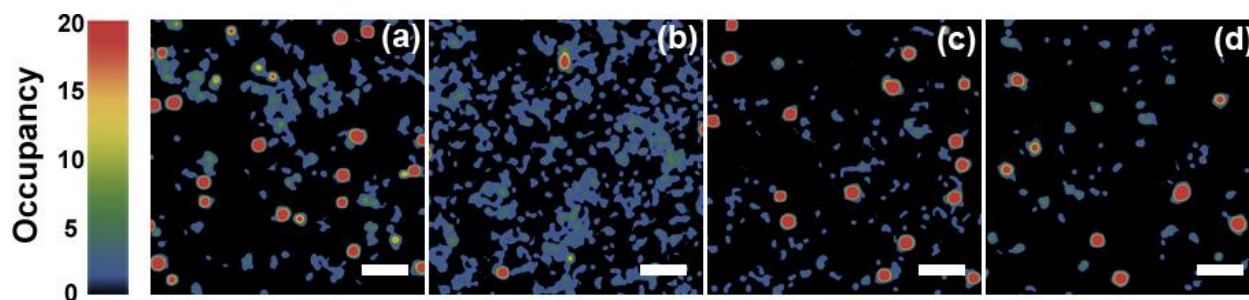


Figure A-2. Representative super-resolution occupancy maps of HSA on an NH_2 surface at area fractions of (a) $\sim 10^{-6}$, (b) $\sim 10^{-4}$, (c) $\sim 10^{-3}$ and (d) ~ 1 . Scale bar = 2 μm .

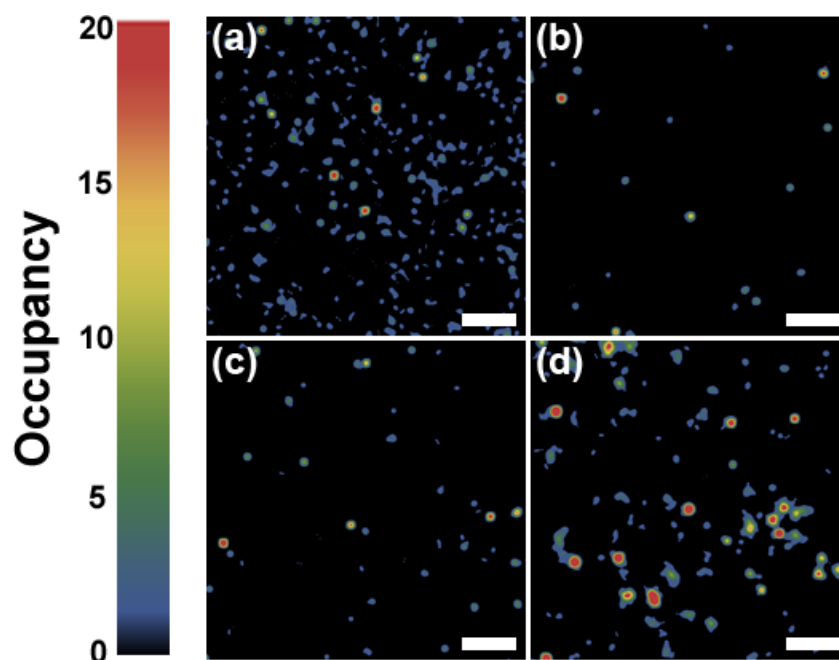


Figure A-3. Super-resolution occupancy maps of donor-labeled HSA molecules on (a) bare NH_2 surface sites, or (b) sites pre-occupied by acceptor-labeled molecules at an HSA area fraction of 10^{-4} ; similarly, donor-labeled HSA molecules on (c) bare NH_2 surface sites or (d) sites pre-occupied by acceptor-labeled molecules at an HSA area fraction of 10^{-3} . Scale bar = 2 μm .

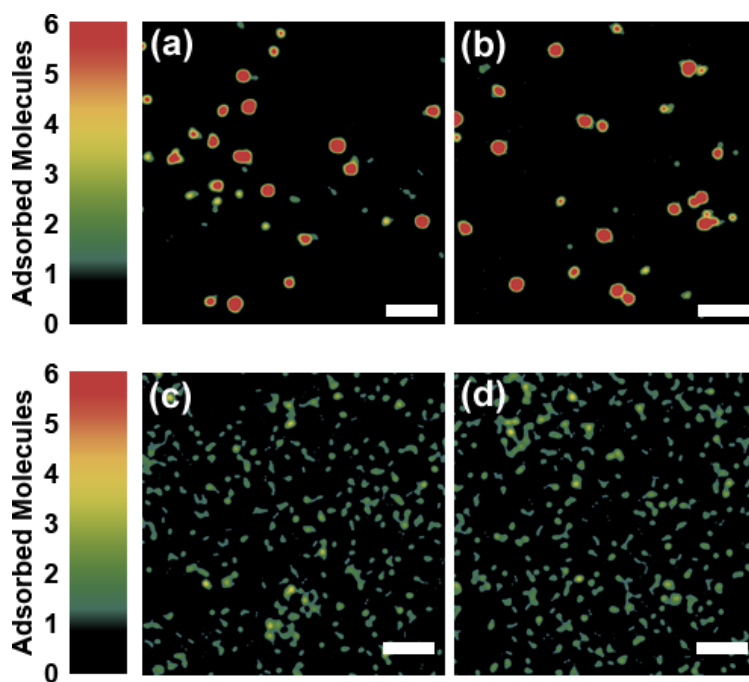


Figure A-4. Representative super-resolution adsorption maps on FS surfaces at an HSA area fraction of $\sim 10^{-6}$ using (a) 10^{-5} mg/mL tracer HSA, and (b) 10^{-7} mg/mL tracer HSA mixed with 10^{-5} mg/ml non-labeled HSA. Similarly, representative super-resolution adsorption maps on NH_2 surfaces at an HSA area fraction of $\sim 10^{-4}$ using (a) 10^{-7} mg/mL tracer HSA mixed with 10^{-6} mg/ml non-labeled HSA, and (b) 10^{-6} mg/mL tracer. On both negatively and positively charged surfaces, the fraction of labeled HSA did not appear to influence the mapping results, specifically the apparent surface density of strong sites.

Appendix B: Supporting Information for Chapter 3

B.1 SUPPLEMENTARY TABLES

Table B-1. The best-fit parameters of f_i and λ_i from a Rayleigh mixture model for the histograms of step sizes. The corresponding diffusion coefficient for each population D_i was calculated by $\lambda_i^2 = 2D_i\Delta t$. The average diffusion coefficients D_{avg} were calculated by $D_{\text{avg}} = \sum_{i=1}^M f_i D_i$. Numbers in the parentheses represent the uncertainties in the last digit.

$[\text{Ca}^{2+}]$ (mM)	f_1	λ_1	D_1 ($\mu\text{m}^2/\text{s}$)	f_2	λ_2	D_2 ($\mu\text{m}^2/\text{s}$)	D_{avg} ($\mu\text{m}^2/\text{s}$)
0	0.54(3)	0.085(4)	0.072(7)	0.46(5)	0.55(5)	3.1(6)	1.5(3)
0.1	0.18(1)	0.090(5)	0.081(9)	0.82(2)	0.56(1)	3.2(1)	2.6(1)
0.2	0.13(1)	0.10(1)	0.11(2)	0.87(1)	0.57(1)	3.2(1)	2.8(1)
0.8	0.055(2)	0.118(3)	0.139(7)	0.945(7)	0.55(1)	3.1(1)	2.93(9)
2	0.021(1)	0.11(1)	0.12(2)	0.98(1)	0.562(4)	3.16(4)	3.14(5)

Table B-2. The ensemble diffusion coefficients calculated by fitting the MSD vs lag time plots for the diffusion of cadherin at different Ca^{2+} concentrations and for the diffusion of fluorescently labeled lipids. Numbers in the parentheses represent the uncertainties in the last digit.

Sample	D_E ($\mu\text{m}^2/\text{s}$)
$[\text{Ca}^{2+}] = 0 \text{ mM}$	1.354(3)
$[\text{Ca}^{2+}] = 0.1 \text{ mM}$	2.225(2)
$[\text{Ca}^{2+}] = 0.2 \text{ mM}$	2.677(5)
$[\text{Ca}^{2+}] = 0.8 \text{ mM}$	3.05(1)
$[\text{Ca}^{2+}] = 2 \text{ mM}$	3.173(3)
DOPC/DOPE-LR (0 mM Ca^{2+})	3.346(5)
DOPC/DOPE-LR (2 mM Ca^{2+})	3.124(5)

Table B-3. The best-fit parameters of μ and σ associated with fits of the histograms of individual trajectory diffusion coefficients to a reciprocal normal distribution. μ and σ are the mean and standard deviation, respectively, of the (Gaussian-distributed) inverse-diffusion coefficient ($1/D$) distribution. Numbers in the parentheses represent the uncertainties in the last digit.

$[\text{Ca}^{2+}]$ (mM)	μ (s/ μm^2)	σ (s/ μm^2)
0	0.30(3)	1.52(3)
0.1	0.15(1)	0.387(8)
0.2	0.12(1)	0.370(5)
0.8	0.105(9)	0.373(8)
2	0.098(9)	0.358(8)

B.2 SUPPLEMENTARY FIGURES

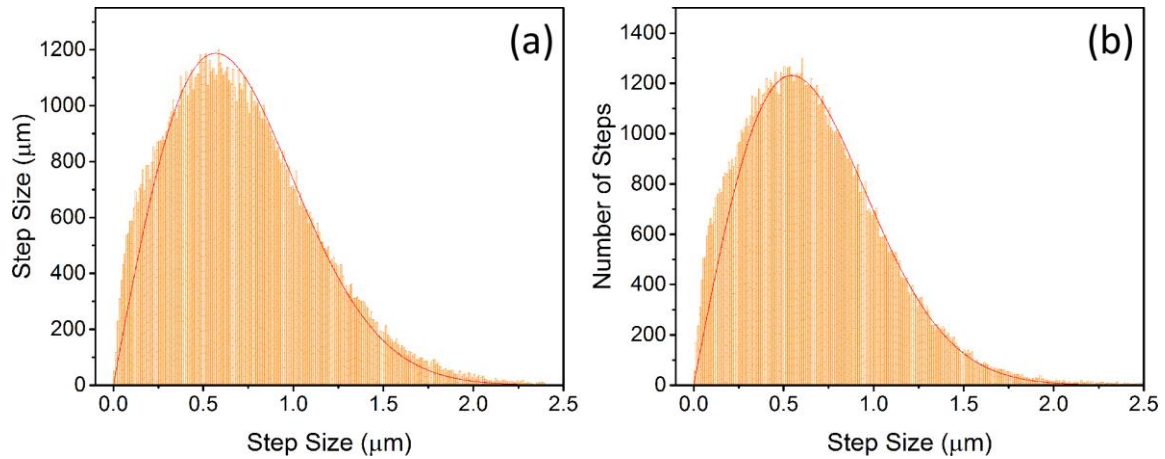


Figure B-1. Step size distributions for fluorescently labeled DOPE-LR lipids in DOPC lipid bilayers at (a) $[Ca^{2+}] = 0$ mM and (b) $[Ca^{2+}] = 2$ mM. Both of the distributions can be nicely described by a Rayleigh distribution (represented by the red lines):

$$N_s(r) = Q \frac{r}{\lambda^2} \exp\left(\frac{-r^2}{2\lambda^2}\right)$$

where N_s is the number of steps with a displacement of r . There was only one population of step sizes (in spite of the negligible shoulders in small step size regions) in both distributions and the values of scaling parameter λ were 0.568(7) and 0.545(5), respectively, associating with fast diffusion.

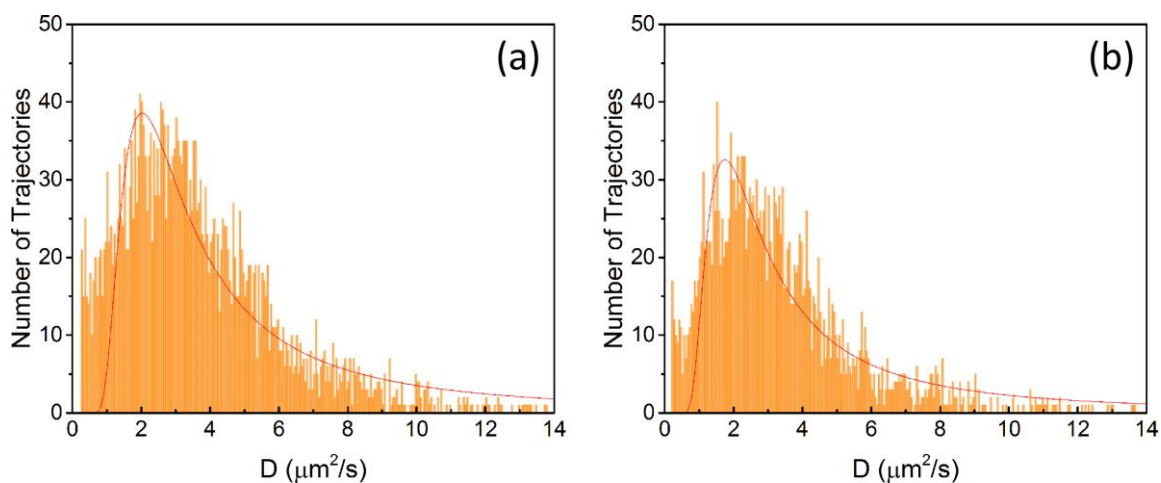


Figure B-2. Histograms of diffusion coefficients for fluorescently labeled DOPE-LR lipids in DOPC lipid bilayers at (a) $[\text{Ca}^{2+}] = 0 \text{ mM}$ and (b) $[\text{Ca}^{2+}] = 2 \text{ mM}$. Red lines represent reciprocal normal fits. The values of fitting parameter μ were 0.098(5) and 0.100(6), which were highly close to the value for fast-diffusing cadherin molecules (see **Table B-3**).

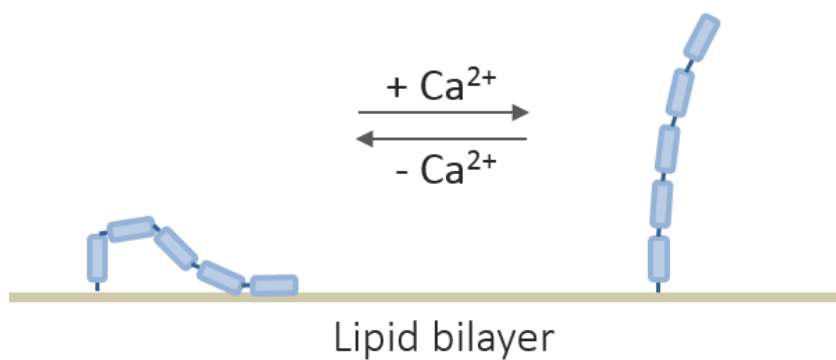


Figure B-3. Schematic sketch for the proposed dynamic shifting mechanism.

Appendix C: Supporting Information for Chapter 4

C.1 SUPPLEMENTARY TABLES

Table C-1. Fitting parameters and calculated diffusion coefficients for mean squared displacement (MSD) versus time plots in **Figure 4-2** in Chapter 4.

	Slope	Standard Error	Diffusion Coefficient
40 nm - Bulk	3.37	0.02	0.84(1)
40 nm - PVDF	0.703	0.001	0.18(0)
200 nm - Bulk	0.76	0.01	0.19(0)
200 nm - PVDF	0.161	0.002	0.04(0)

Table C-2. Calculated standard deviation (SD) values for histograms of normalized residence time distributions at different experimental conditions for three replicate experiments. Standard deviation values, indicating temporal heterogeneity of trajectories in membrane, decreased with Pe and increased with tracer particle size. The observed trends were consistent for replicate experiments. Numbers in parentheses represent uncertainty in the least-significant digit.

	Pe	SD_1	SD_2	SD_3
40 nm	3.3(3)	0.90	0.86	0.92
	5.3(1)	0.75	0.78	0.73
	6.7(2)	0.65	0.67	0.64
200 nm	3.2(2)	0.93	0.92	0.97
	4.9(2)	0.83	0.81	0.87
	6.3(2)	0.77	0.71	0.73

Table C-3. Ratios of mean residence times for more tortuous trajectories (RT_1) and less tortuous trajectories (RT_2) for different experimental conditions. For each experimental condition, trajectories were divided into two groups by the median tortuosity value, and mean residence times were calculated for both groups. Higher RT_1/RT_2 values indicated stronger correlations between tortuosity and retention. For both sizes of tracer particles, RT_1/RT_2 values were significantly smaller for diffusion in bulk, which was consistent with the much weaker correlations observed in the heat maps shown in **Figure C-5**.

40 nm	RT_1/RT_2	200 nm	RT_1/RT_2
$Pe = 3.3(3)$	1.82	$Pe = 3.3(3)$	1.89
$Pe = 5.3(1)$	1.57	$Pe = 5.3(1)$	1.77
$Pe = 6.7(2)$	1.47	$Pe = 6.7(2)$	1.67
Bulk	1.14	Bulk	1.18

C.2 SUPPLEMENTARY FIGURES

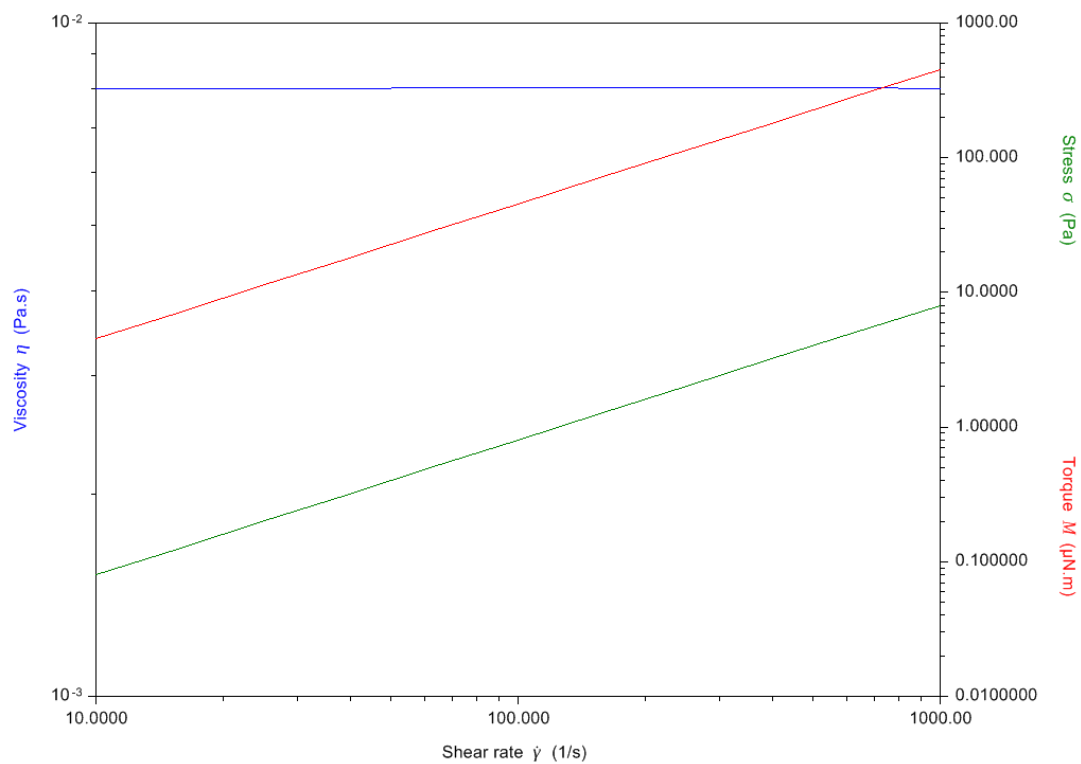


Figure C-1. Flow curves of the index-matching solvent (isopropyl alcohol/Triton X-100). The dynamic viscosity of the solvent was determined to be 0.008 Pa·s and was independent of shear rate. Torque and shear stress were both linear in the shear rate range, and the solvent exhibited Newtonian behavior.

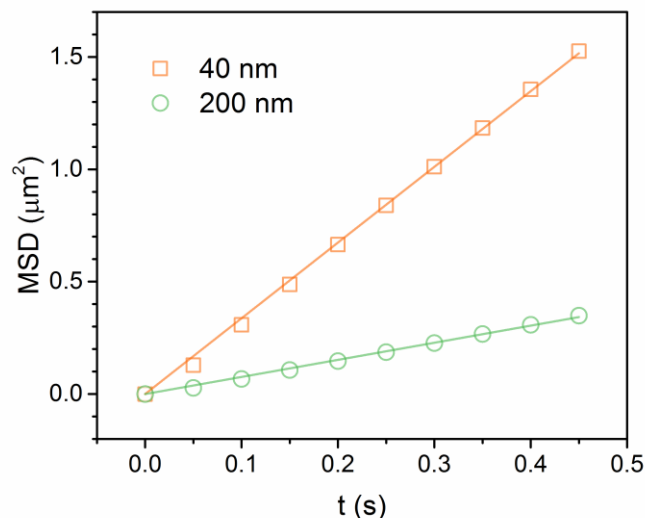


Figure C-2. Mean squared displacements (MSD) versus time plots for 40 nm and 200 nm tracer particles in bulk index-matching solvent. Solid lines represent linear fits to the equation $\text{MSD} = 4Dt$. Calculated ensemble diffusion coefficients were $0.84 \pm 0.01 \text{ } \mu\text{m}^2/\text{s}$ (for 40 nm particles) and $0.19 \pm 0.01 \text{ } \mu\text{m}^2/\text{s}$ (for 200 nm particles). Hydrodynamic radii of tracer particles were calculated using the Stokes-Einstein relation:

$$D = \frac{k_B T}{6\pi\eta r}$$

where k_B is the Boltzmann constant, $T = 293 \text{ K}$, and η is the dynamic viscosity of solvent, which was measured to be $0.008 \text{ Pa}\cdot\text{s}$. The corresponding hydrodynamic diameters estimated for the two tracers were 64 nm and 268 nm, which were systematically larger than the nominal sizes provided by the manufacturer.

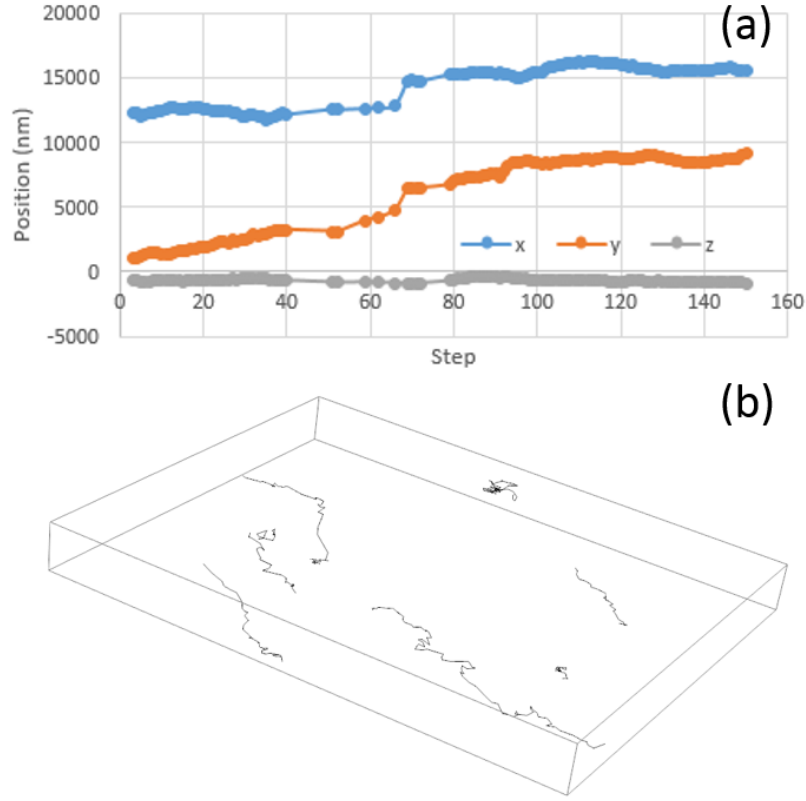


Figure C-3. Results from DH-PSF 3D-tracking experiments with 40 nm tracer particles at $Pe = 1.8$. (a) x, y and z positions versus step plots for a representative trajectory. Fluctuations in the z direction were negligible. (b) Representative trajectories plotted in 3D. Tortuosity values calculated in 2D and 3D were nearly identical ($\tau = 2.5$).

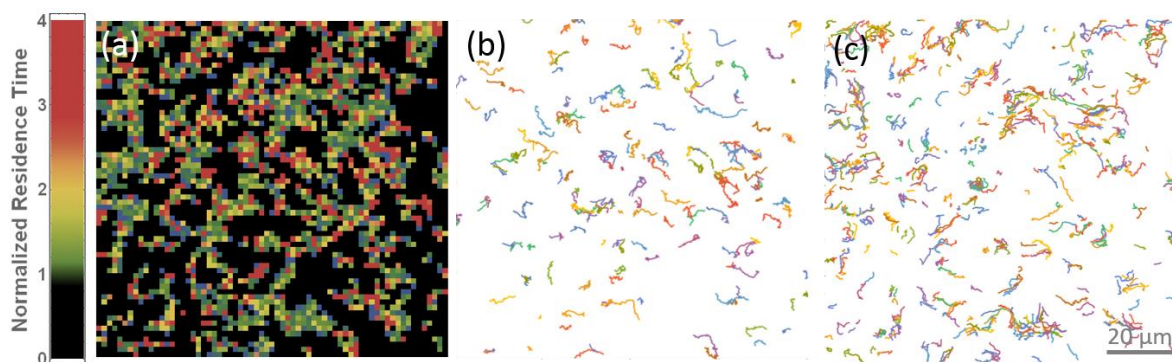


Figure C-4. (a) Heat map of normalized residence times in a representative field of view. Hotter colors indicate longer retention times. Bins with $t/t_0 > 2$ were defined as long-retaining regions (shown as red in the map). Trajectories were further divided into two groups based on the heat map as shown in panels (b) and (c). (b) Trajectories that passed through long-retaining regions. (c) Trajectories that did not pass through any of the long-retaining regions. Tortuosity for trajectories in the two groups were calculated separately for each experimental condition. Scale bar = 20 μm .

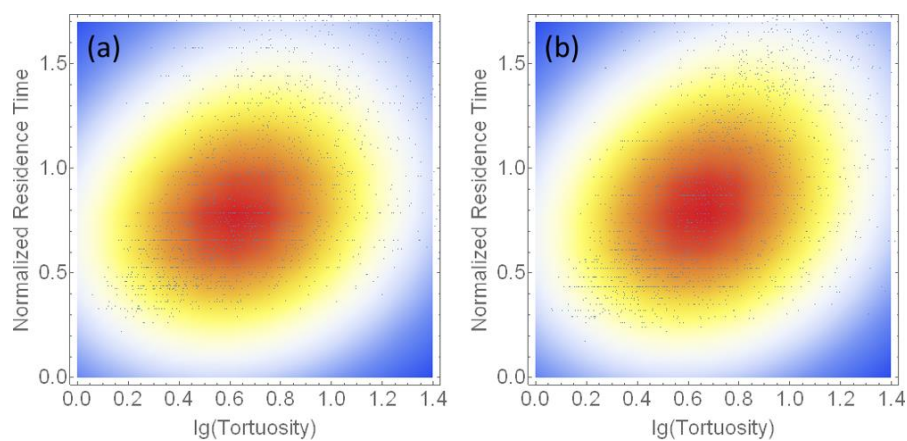


Figure C-5. Heat maps showing correlations of normalized mean residence time per length vs. the logarithm of tortuosity for each trajectory for particles in bulk solvent. (a) 40 nm tracer particles and (b) 200 nm tracer particles diffusion in bulk solvent. Much weaker correlations of tortuosity and retention (as shown in **Figure 4-9** in Chapter 4 for flow conditions in membrane) were observed in these heat maps (see **Table C-3** for more results and discussion), indicating more homogeneous motion of tracer particles in bulk solvent.

Appendix D: Supporting Information for Chapter 5

D.1 SUPPLEMENTARY FIGURES

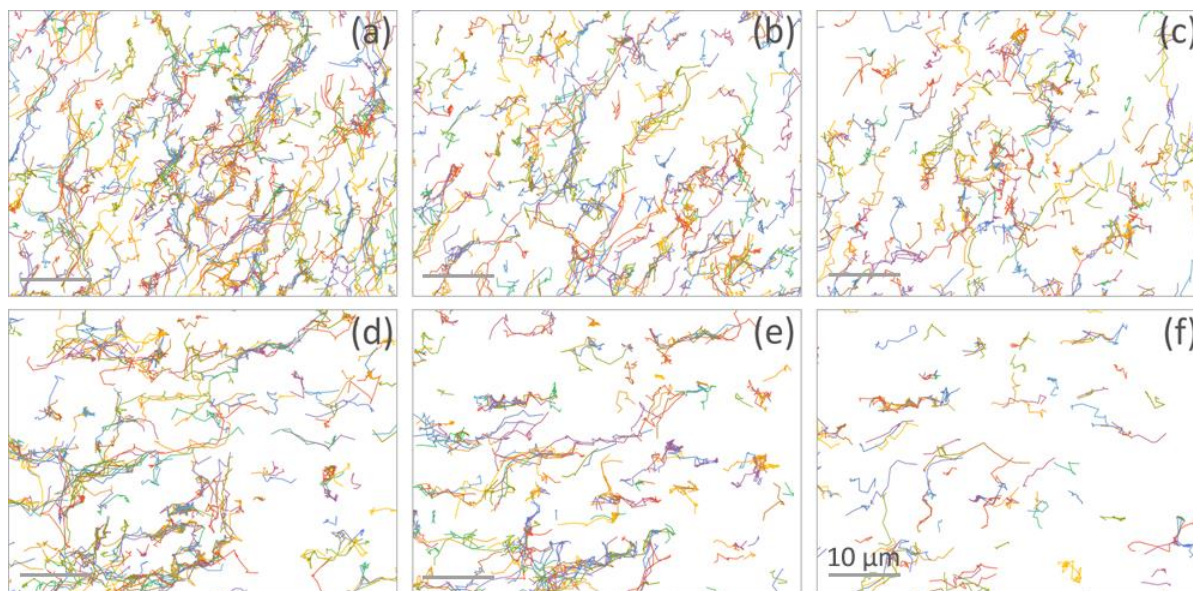


Figure D-1. (a–c) Representative trajectory maps of 40 nm tracer particles in a PTFE membrane under “reduced-sticking” conditions. Trajectories collected in (a) 0–7.5 min, (b) 75–82.5 min and (c) 120–127.5 min were overlaid in each panel. (d–f) Representative trajectory maps of 40 nm tracer particles in a PTFE membrane under “sticking” conditions. Trajectories collected in (d) 0–7.5 min, (e) 47–54.5 min and (f) 105–112.5 min were overlaid in each panel.



Figure D-2. Representative trajectory maps of 40 nm tracer particles in a PVDF membrane under “sticking” conditions. Trajectories collected in (a) 0–7.5 min, (b) 40–47.5 min and (c) 60–67.5 min were overlaid in each panel.

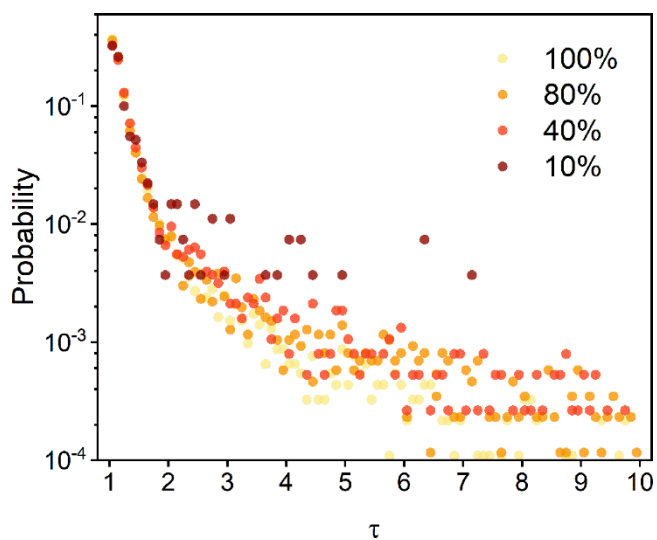


Figure D-3. Probability distributions of 40 nm tracer particles in a PVDF membrane (under “sticking” condition) at different stages of fouling. Percentages in legends indicate normalized flux.